

INCREASING LIFETIMES OF SUPERCONDUCTING QUBITS

ALEXANDER PATRICK MCCORMICK PLACE

A DISSERTATION
PRESENTED TO THE FACULTY
OF PRINCETON UNIVERSITY
IN CANDIDACY FOR THE DEGREE
OF DOCTOR OF PHILOSOPHY

RECOMMENDED FOR ACCEPTANCE BY
THE DEPARTMENT OF
ELECTRICAL AND COMPUTER ENGINEERING

ADVISER: PROFESSOR ANDREW A. HOUCK

SEPTEMBER 2022

© Copyright by Alexander Patrick McCormick Place, 2022.

All rights reserved.

Abstract

Superconducting quantum circuits are a promising platform for quantum computation. The building block for most quantum processors is a qubit (quantum bit) which can store information in a superposition of two states. Superconducting qubits are lithographically defined from metals, often niobium or aluminum. However, these devices have limited use because the information they store decays before most useful computations can take place. In this thesis we explore the cause of these losses. Specifically, we employ tantalum as the capacitor pad of a two-dimensional transmon qubit and find lifetimes and coherence times with dynamical decoupling over $300 \mu\text{s}$. We then switch to a resonator geometry to probe tantalum materials properties. We develop a power and temperature dependent measurement to quantify sources of decay. We find our resonators are primarily limited by two-level system loss at materials interfaces. Finally we employ this resonator characterization method to determine the effects of processing treatments and new packages on resonator decay, showing a buffered-oxide etch before measurement reduces two-level system loss.

Acknowledgements

First, I'd like to thank my advisor Prof. Andrew Houck. I am grateful for the many lessons that Andrew taught me in both science and life. His creativity and care have fostered an extremely welcoming lab. I am continually impressed with his ability to both manage impactful science and lead institutional changes which are critical to ensuring equality for all. Sometimes what he said was tough to hear, but as time goes by I realize the importance of what he did for me. I am also grateful to Prof. Nathalie de Leon, who served as a de-facto advisor. She taught me how to approach science rigorously. She opened my eyes to the world of materials science and I learned a lot from our discussions.

I'd also like to thank Prof. Jeff Thompson for sitting on my generals committee, Prof. Claire Gmachl for reading my thesis, and Prof. Robert Cava for many collaborations. I'd especially like to thank Prof. Steve Lyon, who beyond being on many committees of mine has always had an open door and a fun story to tell. He's always up for a good discussion about interesting physics or life, and he's made the tools in his lab frequently available to us.

I am extremely grateful for my lab mates. They have provided boundless friendship and support. You all are the ones who got me through graduate school, and I can't thank you enough. In chronological order, I'd like to thank Gengyan Zhang—I pestered you with many questions and you were extremely patient and kind. Alicia Kollar, thank you for also putting up with our questions. Tom Hazard, in my mind you are the quintessential get-it-done experimentalist and your smile often lifted the mood. Andrei Vrajitoarea, despite that you want people to think you are prickly your huge heart is extremely obvious. May your life be as fun as a British comedy. Zhaoqi Leng, you are brilliant and I highly valued our friendship. Your contributions to the lab were often unseen and underappreciated, but extremely important. Berthold Jaeck, you often brightened my day. I highly valued your viewpoint both scientifically and politically. Pranav Mundada, you are a measurement whiz and taught me many things. I value the many fun times we had. Mattias Fitzpatrick—I owe you a lot. You taught me to be both a rigorous scientist but more importantly a caring person. You were there for me through tough times, and

through our conversations I learned a lot about the world.

Andras Gyenis, you took me on as your mentee despite not being on your project. You taught me how to design experiments, fab, and measure. More importantly I am grateful to have glimpsed how you think. Beyond lab I highly value our friendship—you literally put a roof over my head. I respect your opinion immensely.

My fellow conspirators in “the three amigos”, I couldn’t have made it through this without you. You both have made major shifts in who I am as a person. Anjali Premkumar, you have given me an entire education, both while buttoning up fridges and by just watching how you touch the lives of the people around you. You also have very impressive intuition. Basil Smitham, I consider you a brother. You are extremely caring, creative, and skilled, and I really mean that. You are the backbone of the lab. I think your inconspicuous kindness has been a major part of what our lab culture has become. You both are my role models.

Sara Sussman, words can’t express the importance of our friendship. You have taught me a tremendous amount about who I want to be. You are the most courageous person I know, and I really mean that. You have helped me through more situations than I could ever count. You’re also an electronics magician.

Kevin Crowley, Aveek Dutta, and Lila Rodgers, you’ve been there for me through thick and thin on T1Team. Kevin, our friendship has taught me a ton. I’m honored to have spent the last year working with you. Aveek, you have an extraordinary ability to take a step back and put perspective on a situation. You’re both creative and skilled at getting the job done. You often brightened my day with a fun story. Lila, I am forever grateful for the support you’ve given me through some tough times. Your friendship pulled me through. Russell McLellan, even though you’ve only been here for half a year I already feel like we’re old friends. Archimedes and Newton don’t have a chance against your intelligence or your beatboxing. Nana Shumiya, we haven’t had much time together but you’ve already cracked me up a ton. I wish us and Yuki could work together longer.

Jake Bryon, you are currently making fun of me as I write this. You’re an awesome person, you brighten my day, and I’m honored to call you a friend. Xanthe Croot, Tesla

should study you to figure out how to make longer lasting batteries. Your desire to and skill at making the world a better place is remarkable—whether that's writing letters to the editors of the Bachelor or trying to direct money for more effective disease research.

Christie Chiu, you inspire me with your theory skills and your ability to help so many people in a day. You are a model leader and mentor. Jeronimo Martinez, you brighten my mornings and are becoming a fab monster. You and Parth Jatakia have very impressive careers ahead. Parth, I don't know of anybody who makes me laugh more often than you. You're humble and you go out of your way to help the people around you, even if they don't see it. Charlie Guinn, you've been a delight this last year, I hope your life is filled with frequent trips to Applebees. Jeremiah Coleman and Shashwat Kumar, you have both become valuable parts of our lab and I'm excited to follow your bright futures.

I've had the honor of working with several undergraduates who are amazing people. Harsh Babla was the first to join. Our conversations have broadened my mind. I am grateful for your optimistic and fun attitude, and your skills will take you far. I look forward to many more deep thoughts with you in the future. Youqi and Hoang, it's only been a month since you left and I already miss you. You are both extremely skilled and will go far, but that's not what makes me respect you. Youqi, you are courageous and passionate, but also extremely kind. Hoang, you have a curiosity that can't be quenched and sharing it lights up the people around you. Trisha Madhavan, reflecting on our time together just makes me grin. You had my back in some tough times and I'm forever grateful. You are incredibly kind and know how to get the job done. Nishaad Khedkar, thank you for brightening my day every time I saw you. You always had a smile while doing some really good work. I am excited to continue hearing about your many adventures. Cosmin Andrei, we've had a lot of good times. Your curiosity is inspiring. Cady Feng, you were a pleasure to work with and a sapphire processing pro. Esha Umbarkar, you just started but you're already killing it. You all will go far and I'm excited to keep in touch with each of you.

There are a ton of unsung heroes of the Princeton Engineering departments who are critical to our research. The PRISM Cleanroom staff has been nothing short of

tremendous. Everyone likes to complain about the cleanroom, but it needs to be said that you do a stellar job. Joe Palmer and Paul Cole, you are nothing short of a blessing. Our conversations have shaped how I view the world. I don't think you realize how much getting to talk to you all made my day, every time. Bert Harrop, you "da" man. Zuzanna Lewicka, you've always been there for me and I've really enjoyed our time together. Roman Akhmechet, I was scared of you to start but that sly smile of yours quickly revealed itself—you are an asset to the cleanroom. Brien Ely, you are the most sane person in the cleanroom and you are a tool genius. Magda Moczala-Dusanowska, you have gone above and beyond what was asked of you and always make me smile. Eon Mckenzie, I really value our conversations and your positivity, you may be the wisest man in Princeton. Eric Mills, Ian Harvey, and David Barth, though you beat me to leave you were all instrumental in my PhD and wonderful friends.

Prof. Nan Yao's Imaging and Analysis Center is top notch and the team he's organized is remarkable. John Schrieber and Denis Potapenko, you are both highly skilled and just a lot of fun to be around. I just chuckle thinking about a lot of the good times we've had. Guangming Cheng, you are a magician with the TEM and often brightened my day.

The department staff have been a joy to work with. Barbara Fruhling, you've been a constant source of support, thank you. Cecilia York, thank you for putting up with me, we've had a lot of fun. Eric Litostansky and Bill Gervasi, you've pulled through in big ways, I owe you a lot of beers. Dave and Kevin, you all have the best attitude I've ever seen. Jean Bausmith, Kate Brosowsky, Colleen Conrad, and Roelie Abdi, you all have run a mean lean graduate office machine. David Radcliff, thanks for all of the help over the years. Phil Curry, Enrique Guerrero, and Anthony Schulz, thanks for all of the help and good conversations.

There are also several notable people who have served as both mentors and dear friends before and throughout graduate school. Peter Hung, Charles Steinhardt, and Prashanth Venkataram, I am immensely grateful to the three of you.

I had the pleasure of growing in faith with a brilliant and extremely generous group of people at the Episcopal Church at Princeton. Father Allen and Mother Kara, you both

provided unceasing guidance and care throughout my PhD. Your leadership has grown an extremely special community. There are too many parishioners who have made a huge impact on me to name—thank you all for the many wonderful conversations and true support.

Thank you to all the people who made my time outside of lab enjoyable around Princeton. Kevin Nuckolls and Theano Stavrinos have provided constant support and friendship. I am extremely grateful to Valentin Skoutnev, Michael Soskind, Brady Gunnarsson, Jordan Dull, Kyle Castoria, Eric Blow, Jason Liu, and many others for many sports and adventures.

There are also several continuing friendships from childhood and undergrad that have and continue to define who I am. I would be lost without these guiding stars.

Finally I want to thank my family. Uncle Billy, you taught me the importance of curiosity. Dr. Boswell, you have always been my role model, both academically and more broadly. I am blessed to have a second family on and around Florida Street—you all mean the world to me, thank you. I am grateful to my brother Kevin for his tough love and my sister-in-law Jenna for her not-tough love. Sarah, you are my foundation. You are always there for me. You give me the confidence to face the many challenges in lab, but you also erase my worries on our many adventures. Your passion, dedication, and courage continually inspire me. The two people who I owe everything to are my mom and dad. I truly believe there are no better parents out there. No words can describe the boundless love you gave Kevin and me or the joy of spending an evening with you. I have always hoped to be just like you both one day.

To my family.

Contents

Abstract	3
Acknowledgements	4
List of Figures	15
List of Tables	18
1 Introduction	19
1.1 Background: Quantum Computing	19
1.2 Principles of Operation	20
1.2.1 The Lumped Element Resonator	20
1.2.2 Anharmonic Oscillator: The Transmon	23
1.3 Qubit Loss Measurements	26
1.3.1 Detour: The Bloch Sphere	27
1.3.2 Depolarization: T_1	27
1.3.3 Depolarization: Q	29
1.3.4 Decoherence: T_2	29
1.4 Coherence Times and the Bigger Picture	31
1.4.1 History of T_1	33
1.5 Thesis Overview	33
2 Sources of Loss	34
2.1 Introduction	34
2.2 Classical Dielectric Loss	34
2.3 Two-Level Systems (TLS)	38

2.3.1	Evidence for Strongly Coupled Individual TLS	39
2.3.2	TLS Saturation	40
2.3.3	Empirical Saturation Models	41
2.3.4	Quantum Corrections: Photon Number (and Extra Temperature) Dependencies	42
2.3.5	Temperature Dependence of TLS T_1 and T_2	47
2.3.6	Driving Voltage Correction	50
2.3.7	TLS Loss Summary	50
2.3.8	Interface Participation Ratios: Microscopic Origins	51
2.4	Quasiparticles	52
2.4.1	Junction Quasiparticle Losses	53
2.4.2	Resonator QP Losses	53
2.4.3	Sources of Quasiparticles	54
2.4.4	Photon-Assisted Parity Switching (PAPS)	55
2.5	Decay Into Environment: Purcell and Packaging	55
2.5.1	Purcell Limit	55
2.5.2	Packaging Decay	57
2.6	Other Sources of Loss	58
2.6.1	Vortex Loss	58
2.6.2	Quasiparticles Forming TLS	58
2.7	Comparing Loss Source Contributions	59
3	Qubit Materials: Overview	60
3.1	Introduction	60
3.2	Desired Materials Properties: Superconductors	60
3.2.1	T_c	60
3.2.2	Oxide	61
3.2.3	Crystallinity and Grain Boundaries	62
3.2.4	Patterning	63
3.3	Desired Materials Properties: Substrate	63

3.3.1	Classical Loss	63
3.3.2	Substrate-Air Interface	63
3.3.3	Substrate-Metal Interface	64
3.3.4	Substrate Defects	64
3.3.5	Dielectric Constant	64
3.3.6	Quasiparticle Coupling	64
3.4	Probing Materials	65
3.4.1	X-ray Diffraction (XRD)	65
3.4.2	XPS	66
3.4.3	AFM	67
3.4.4	PPMS	67
3.4.5	SEM and TEM	68
4	Tantalum Transmons	69
4.1	Introduction	69
4.2	Fabrication	70
4.2.1	Sapphire Preparation	70
4.2.2	Deposition and Lithography	74
4.2.3	Device Packaging	76
4.2.4	Design and Fabrication Notes	78
4.3	Measurement	80
4.3.1	CPMG	82
4.3.2	Fitting Procedure	84
4.4	Device iterations	84
4.4.1	Transmon on a Silicon Substrate	87
4.5	Characterization of tantalum films.	87
4.5.1	Overview	87
4.5.2	X-ray Diffraction	91
4.5.3	Grain Boundaries	91
4.5.4	Tantalum Oxide	93

4.5.5	Sapphire-Tantalum Interface	94
4.5.6	XPS, AFM, XRD Characterization Details	94
4.5.7	Electron Microscopy Characterization Details	96
4.6	Discussion	96
5	Quantifying Sources of Loss	98
5.1	Introduction	98
5.2	Resonator Overview	99
5.2.1	Coplanar Waveguide (CPW) Resonators	100
5.2.2	Measurement Overview	100
5.3	Temperature Fits	102
5.4	Varying Participation Ratios	104
5.5	Quantifying Effects of Fabrication Procedures: BOE	106
5.6	Q_{other} Comparison	108
5.7	Comparison to Qubits	111
6	Conclusion and Outlook	112
A	Detailed Fabrication Procedures	114
A.1	Detailed Transmon Fabrication Procedure	114
A.1.1	Substrate and Substrate Preparation	114
A.1.2	Photolithography	114
A.1.3	Etch	116
A.1.4	Clean	116
A.1.5	Electron Beam Lithography	116
A.1.6	Junction Deposition	117
A.2	Detailed Resonator Fabrication Procedure	118
B	Tantalum Deposition	120
B.1	Optimized Recipe	120
C	Tantalum Etches	122

D Josephson Junction Fabrication	125
D.1 Manhattan Junction Overview	125
D.2 Exposure Problems	126
D.2.1 Flagging	126
D.2.2 Residual Carbon	126
E How to Design a Transmon	131
E.1 Transmon Design	131
E.1.1 Transmon Hamiltonian Parameters	131
E.1.2 Transmon Layout	133
E.1.3 Example Transmon Parameters	139
F Participation Ratio Simulations	140
F.1 Participation Ratio Simulations: Qubits	140
F.1.1 Results	142
F.2 Participation Ratio Simulations: Resonators	144
G Sample Resonator Temperature and Power Dependent Fits	145

List of Figures

1.1	Lumped Element Resonator	20
1.2	Energy Spectra	22
1.3	The Josephson Junction	24
1.4	The Bloch Sphere	28
1.5	Dephasing on the Bloch Sphere	30
1.6	History of T_1 and T_2	32
2.1	Possible Sources of Two-Level System (TLS) Loss	35
2.2	Photon Number Dependence of Loss	36
2.3	TLS Overview	36
2.4	Example Two-Level System	37
2.5	Summary of TLS-Photon Interactions	40
2.6	Classical Temperature Dependence of TLS Loss	43
2.7	TLS-Limited Quality Factor	51
2.8	Interface Participation Ratios	52
2.9	Proposed Quasiparticle Generation Channel	54
2.10	Basics of Purcell Filters	56
3.1	Oxide Interfaces	61
3.2	Measured Niobium Oxide Composition as a Function of Depth	62
3.3	XRD Overview	65
3.4	XRD Measurement of Tantalum and Sapphire	66
4.1	Characterization of Sapphire Surface	72

4.2	Sapphire Processing Pitfalls	73
4.3	Qubit Fabrication Process	75
4.4	Device Geometry Overview	77
4.5	Tantalum-Based Transmon Superconducting Qubit	79
4.6	Schematic of the Measurement Electronics and Device Shielding	81
4.7	Lifetime and Decoherence Measurements	83
4.8	Spectral Decomposition of Device 11c	84
4.9	CPMG Traces	85
4.10	Microscopy and Spectroscopy of Tantalum Films	88
4.11	X-ray Diffraction Spectrum of a Sputtered Tantalum Film on Sapphire .	89
4.12	Oxide Characterization	90
4.13	Grain Boundary Characterization	92
4.14	Tantalum-Sapphire Interface Characterization	95
5.1	Coplanar Waveguid Resonator Overview	99
5.2	Multiplexed Resonator Measurements	101
5.3	Resonator Temperature and Power Fit	103
5.4	Comparison of Resonator Interface Participation Ratio Pitch Dependence	104
5.5	Q_{TLS0} Dependence on Pitch	105
5.6	BOE Oxide Thickness Measurement	107
5.7	Effect of BOE on Q_{TLS0}	107
5.8	Comparison of CPW and Lumped Element Q_{other}	109
5.9	Qubit Quality Factor Dependence on Participation Ratio	110
A.1	Lithography Overview	115
B.1	XRD of Working Tantalum Deposition	121
B.2	PPMS Measurement of Working Tantalum Deposition	121
C.1	Scanning Electron Microscopy Images of Tantalum Etch Development .	123
C.2	Chlorine Plasma Etch	124

D.1	Josephson Junction Fabrication Overview	126
D.2	Undercuts and Flagging	127
D.3	Dose Regions for Electron Beam Exposure	128
D.4	Undercut Problems	128
D.5	Unclean Exposure	129
E.1	Definition of Capacitances	133
E.2	Purcell Filter Overview	135
E.3	Microwave Office Simulation Overview	136
E.4	Importance of Deposition Direction on Capacitor-Junction Contact . . .	138
F.1	Overview of Simulation Components	141
F.2	Simulated Designs	143
G.1	Sample Low Quality Fit	146
G.2	Sample Low Quality Fit	147
G.3	Sample Low T_c Fit	148

List of Tables

4.1	Summary of Devices	71
5.1	Fit Parameters of Resonator Temperature and Power Fit	102
E.1	Example Transmon Parameters	139
F.1	Capacitor Pad Participation Ratios	142
F.2	Aluminum Participation Ratio	143
F.3	Coplanar Waveguide Participation Ratios	144

Chapter 1

Introduction

1.1 Background: Quantum Computing

Computing the time dynamics of a quantum system has been a topic of great interest over the past two decades. To physicists, simulating interacting atoms can reveal new phenomenon and insights about the rules governing the mesoscopic world [1]. Materials scientists and chemical engineers are interested in simulating classically intractable questions at the nanoscale, for example to build better batteries [2] or medications [3]. Surprisingly a much wider set of problems in linear algebra and cryptography can also be mapped to algorithms involving interacting quantum objects [4, 5].

To compute the time dynamics of a quantum system, most quantum processor proposals evolve a register of two-state quantum bits, or “qubits”, under the influence of engineered interactions with other qubits. Several qubit architectures have been proposed, including trapped ions [6], color centers [7], and cold atoms [8]. This thesis focuses on superconducting qubits—superconducting films that are lithographically defined with nanometer to micron feature sizes. Techniques similar to those found in classical foundries are used to make capacitive and inductive circuit elements for single microwave photons. Combined in the correct way, the energy levels of the resulting qubit are similar to a bound electron. In this way we can engineer “artificial atoms”.

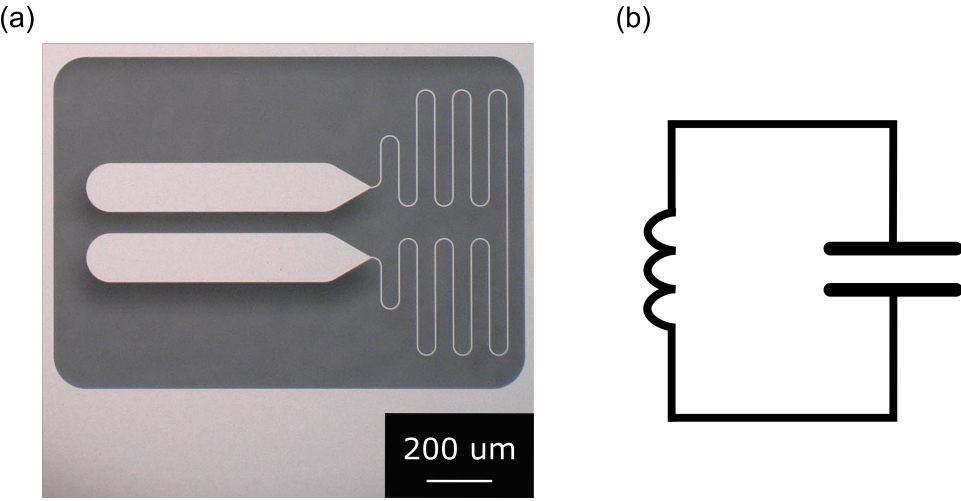


Figure 1.1: **Lumped Element Resonator.** (a) Optical image of a lumped element resonator with equivalent circuit shown in (b).

1.2 Principles of Operation

1.2.1 The Lumped Element Resonator

Background

The simplest resonant circuit is an LC oscillator. Though the energy spectrum of this circuit doesn't contain a subspace that is usable as logical qubit states (proven below), an LC oscillator experiences many of the energy decay channels present in more complex qubits. Its simple spectrum and ease of fabrication make it ideal as a starting circuit to analyze as well as a useful tool to measure qubit loss channels. Furthermore, the transmon qubit, the design primarily used in superconducting qubit industry, is a simple perturbation of the LC oscillator.

Hamiltonian

A wire patterned from a thin superconducting film has a self-inductance which shorts two adjacent electrodes that provide a capacitance, as shown in figure 1.1. Following [9], to find the energy levels of the LC oscillator we first write the Lagrangian. Noting q as the charge on the capacitor, L the inductance, and C the capacitance

$$\mathcal{L} = \frac{1}{2}L\dot{q}^2 - \frac{1}{2C}q^2. \quad (1.1)$$

Defining the momentum conjugate to the charge as

$$\Phi = \frac{d\mathcal{L}}{d\dot{q}} = L\dot{q} \quad (1.2)$$

we can write the Hamiltonian

$$H = \Phi\dot{q} - \mathcal{L} = \frac{\Phi^2}{2L} + \frac{q^2}{2C}. \quad (1.3)$$

If we make the typical assumption that we can promote Φ and q to quantum operators, and then change variables for convenience we can write

$$\begin{aligned} \hat{a} &= i\frac{1}{\sqrt{2L\hbar\Omega}}\hat{\Phi} + \frac{1}{\sqrt{2C\hbar\Omega}}\hat{q} \\ \hat{a}^\dagger &= -i\frac{1}{\sqrt{2L\hbar\Omega}}\hat{\Phi} + \frac{1}{\sqrt{2C\hbar\Omega}}\hat{q} \end{aligned} \quad (1.4)$$

$$H = \hbar\Omega(\hat{a}^\dagger\hat{a} + \frac{1}{2}) \quad (1.5)$$

with the resonant frequency the same as a classical operator, $\Omega = \frac{1}{\sqrt{LC}}$. This gives an infinite number of eigenstates equally spaced by resonant frequency Ω (see figure 1.2 (a)).

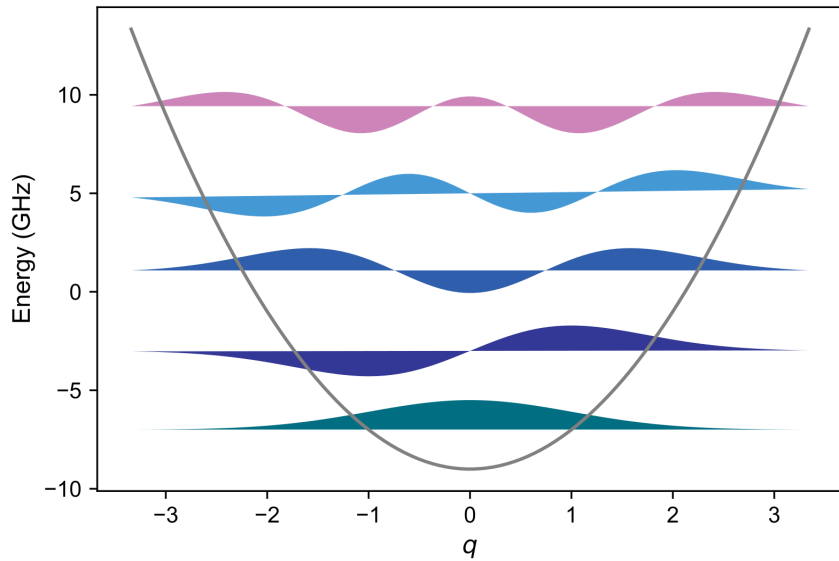
Driving the LC Oscillator

How can we excite the LC oscillator? Suppose we apply an oscillating electric field across the capacitor, inducing a maximum voltage difference V at frequency Ω_d . This adds a term to the Hamiltonian

$$\begin{aligned} H_{drive} &= V \cos(\omega_d t)\hat{q} \\ &= V \cos(\omega_d t)\sqrt{2C\hbar\Omega}(\hat{a} + \hat{a}^\dagger) \end{aligned} \quad (1.6)$$

In order to find the frequency ω_d that will create the fastest gates, move the time

(a)



(b)

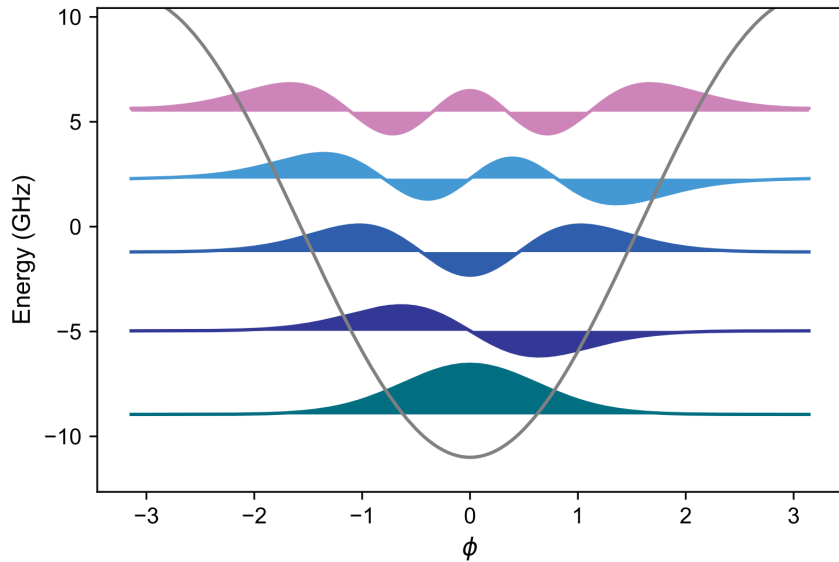


Figure 1.2: **Energy Spectra** Wavefunctions, shifted by their energies, plotted on top of the potential of a (a) LC oscillator and (b) transmon (with help from the package scQubits in Python).

dependence of equation 1.6 to the operators by changing to the Heisenberg picture

$$\begin{aligned} H_{drive} &= V \cos(\omega_d t) \sqrt{2C\hbar\Omega} (e^{-i\Omega t} \hat{a} + e^{i\Omega t} \hat{a}^\dagger) \\ &= \frac{V}{\sqrt{2}} \sqrt{C\hbar\Omega} (e^{-it(\omega_d - \Omega)} \hat{a} + e^{it(\Omega - \omega_d)} \hat{a}^\dagger) \end{aligned} \quad (1.7)$$

where we have ignored the terms that have frequencies far from DC, noting that since they are rapidly oscillating they will on average cause very little change to the qubit state (the rotating wave approximation). By the same logic, if there is an off resonant drive, i.e. Ω is far from ω_d , the terms that were kept can be ignored—the drive doesn't change the state of the qubit! However, if $\omega_d = \Omega$, the time dependence cancels and the drive is able to move the qubit up or down to adjacent energy levels.

Why the LC Oscillator Is Not a Qubit

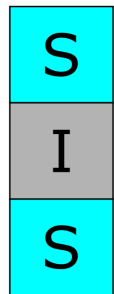
In the case of the LC oscillator, the energy level splitting between the n and $n + 1$ eigenstates, $\omega_{n,n+1}$, is the same for every n . Suppose we set the lowest two levels of the harmonic oscillator as our qubit states. Applying a drive at frequency $\omega_{0,1}$ can move us in between these two levels. However, it can also move us from level 1 to level 2. We no longer have a qubit but instead a 3-level system, though if we keep applying this drive we will approach an infinite-level system!

To ensure population is always in a two state manifold, a workable qubit should have $\omega_{0,1} \neq \omega_{1,2}$. This way, a drive applied at frequency $\omega_{0,1}$ can no longer move the qubit from the 1 to 2 state. The level detuning is a sufficiently important concept that it has a name—the anharmonicity: $\alpha \equiv \omega_{1,2} - \omega_{0,1}$.

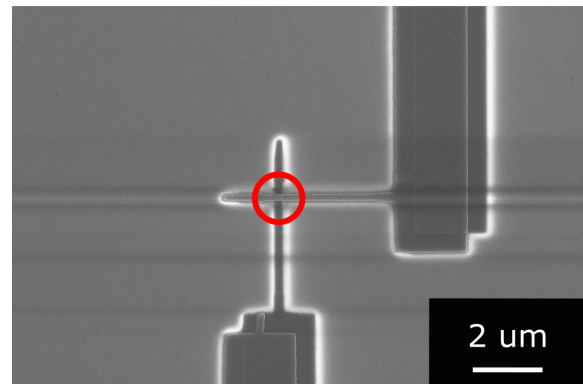
1.2.2 Anharmonic Oscillator: The Transmon

Finding a device with non-zero anharmonicity should allow us to isolate two levels that can be used as a qubit subspace, as we saw in the last section. We can create this anharmonicity by deforming the potential shown in figure 1.2 (a), which will in turn shift the qubit energy levels anisotropically. To achieve this we'll first examine a new circuit element: the Josephson junction.

(a)



(b)



(c)

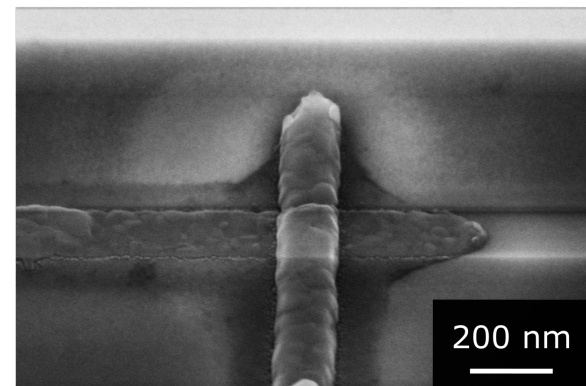


Figure 1.3: **The Josephson Junction.** (a) Schematic image of a Josephson junction, composed of an insulator sandwiched between two superconducting leads. (b) Image of an aluminum Josephson junction on sapphire. The junction is circled, the rest of the aluminum is used to connect to the capacitor pads. (c) Enlarged image of another Josephson junction.

A Josephson junction is an insulating barrier between two superconductors (figure 1.3). The barrier is sufficiently small that cooper pairs can tunnel over it. Expressing this tunnelling in terms of the number of cooper pairs that have crossed the junction, n [9]:

$$H_{JJ} = -\frac{E_J}{2} \sum_n (|n\rangle \langle n+1| + |n\rangle \langle n-1|). \quad (1.8)$$

To simplify this equation, consider the fourier space to the charge¹:

$$|n\rangle = A \int e^{-in\phi} |\phi\rangle d\phi \quad (1.9)$$

for some normalization constant A. Note that

$$\begin{aligned} \cos(\phi) |n\rangle &= \frac{1}{2}(e^{i\phi} + e^{-i\phi}) |n\rangle \\ &= \frac{1}{2} \int (e^{i\phi} + e^{-i\phi}) e^{-in\phi} |\phi\rangle d\phi \\ &= \frac{1}{2} \int e^{-i(n-1)\phi} |\phi\rangle d\phi + \int e^{-i(n+1)\phi} |\phi\rangle d\phi \\ &= \frac{1}{2} (|n-1\rangle + |n+1\rangle). \end{aligned} \quad (1.10)$$

If ϕ and n were quantum operators (which will be the case below), then:

$$\cos(\phi) = \frac{1}{2} \sum_n (|n-1\rangle \langle n| + |n+1\rangle \langle n|) \quad (1.11)$$

Employing equation 1.11 to simplify the Josephson junction Hamiltonian (equation 1.8) gives

$$H_{JJ} = -E_J \cos(\phi). \quad (1.12)$$

Close to zero, a cosine potential is very similar to a harmonic oscillator potential. However, higher energy levels sample the potential further from the origin where the cosine differs from a parabola. Accordingly, the higher energy levels are shifted, creating

¹Note that this can be more rigorously justified through a tight binding model [9] or if we first prove ϕ and n are conjugate quantum operators [10].

anharmonicity. This is the key difference between the LC oscillator and the transmon—the inductor is switched to a Josephson junction, making a non-harmonic potential (figure 1.2 (b)).

To quantify this intuition, we can write the Hamiltonian of the transmon by switching the potential in equation 1.3 for that given in equation 1.12 ²:

$$\begin{aligned}
 H_{transmon} &= 4E_c\hat{n}^2 - E_J\cos(\hat{\phi}) \\
 &\approx 4E_c\hat{n}^2 - E_J\left(\frac{-\hat{\phi}^2}{2!} + \frac{\hat{\phi}^4}{4!}\right) \\
 &= \underbrace{4E_c\hat{n}^2}_{H_{LC}} + \underbrace{\frac{E_J}{2}\hat{\phi}^2 - E_J\frac{\hat{\phi}^4}{4!}}_{H_1}
 \end{aligned} \tag{1.13}$$

where $E_c \equiv \frac{e^2}{2C}$. This explicitly shows $H_{transmon}$ is a combination of the LC oscillator Hamiltonian and an additional perturbation. The perturbation lowers the qubit frequency by a photon number-dependent amount—creating anharmonicity: $\omega_{01} - \omega_{21} \approx E_c$ [11]. Accordingly, we can use the lowest two levels as the isolated logical qubit states.

1.3 Qubit Loss Measurements

Now that we've established how to isolate and drive a logical qubit subspace, we'll consider how losses change the state of the qubit. If we had an ideal device, once it was initialized it would stay in the same state forever, or at least until we apply a gate to it. Unfortunately, in reality there are two main types of noise: (1) the qubit will naturally decay to the lowest energy state (depolarization) and (2) the phase of the qubit will spuriously change (decoherence). Before we formalize these definitions, first we'll introduce a convenient formalism to visualize the state of a qubit.

²Note that we are switching the charge operator from the continuous q to the discrete n , and correspondingly we redefine the phase variable, the proof of which we will not show here. Equation 1.13 is rigorously derived in [9].

1.3.1 Detour: The Bloch Sphere

To aid in the conceptualization of a qubit state, we'll first look at the Bloch sphere representation. A qubit's logical subspace has two degrees of freedom and can be written without loss of generality as:

$$|\Psi\rangle = \cos(\theta)|0\rangle + e^{i\phi}\sin(\theta)|1\rangle \quad (1.14)$$

We can map these two degrees of freedom to a unit sphere as shown in figure 1.4. Note that since the qubit has a finite energy splitting, even in the absence of any drives ϕ has a time dependence:

$$\begin{aligned} i\hbar\frac{d}{dt}|\Psi(t)\rangle &= \hat{H}|\Psi(t)\rangle \\ &= \hbar\omega_{0,1}e^{i\phi}\sin(\theta)|1\rangle \end{aligned} \quad (1.15)$$

Noting the ground state doesn't change with time, the solution gives

$$\phi(t) = -\omega_{0,1}t. \quad (1.16)$$

Accordingly, if the state vector is initialized anywhere on the equator of the bloch sphere it will precess around the z-axis.

We can now conceptualize the two types of loss. Depolarization takes the qubit from $|1\rangle$ to $|0\rangle$ —i.e. it forces the qubit to decay along the $-\hat{z}$ direction of the Bloch sphere. Decoherence changes the natural precession rate of the qubit around the equator.

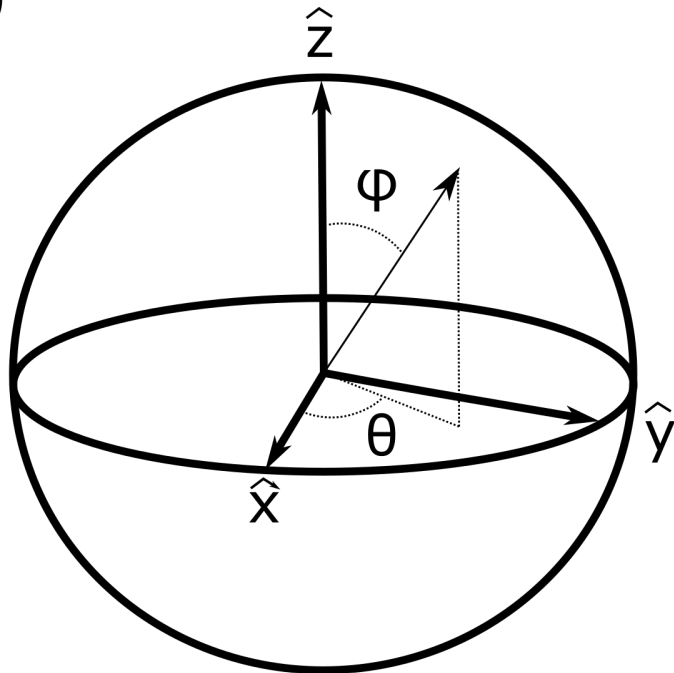
1.3.2 Depolarization: T_1

First, let's consider the qubit's natural tendency to decay to the lower energy state—down the $-\hat{z}$ direction of the Bloch sphere.

Suppose there exists a noise source, with operator \hat{N} , that couples to the qubit via some operator \hat{Q} [12]. Fermi's golden rule gives:

$$\Gamma = \frac{1}{\hbar^2} |\langle 0 | \hat{Q} | 1 \rangle|^2 S_N(\omega_{0,1}) \quad (1.17)$$

(a)



(b)

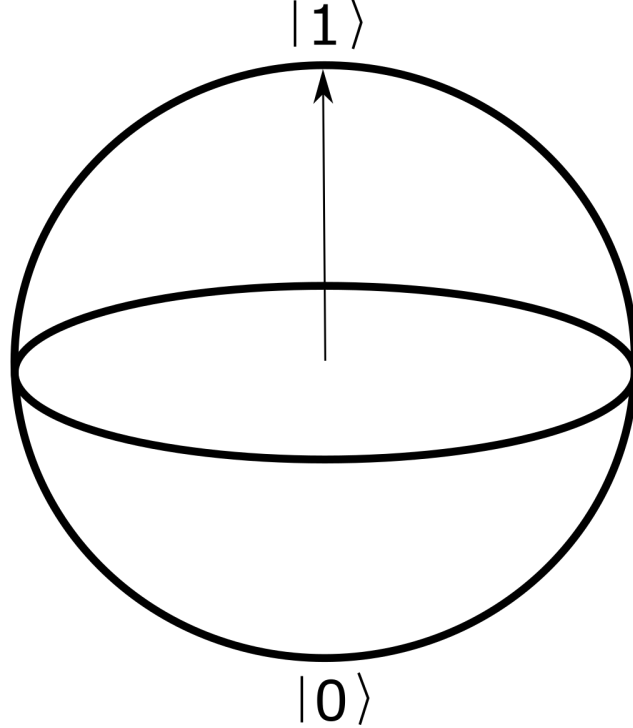


Figure 1.4: **The Bloch Sphere.** (a) Conversion between equation 1.14 and the Bloch sphere. (b) The $|0\rangle$ and $|1\rangle$ states are the poles of the Bloch sphere. A vector not at the poles is a superposition of the two states.

where Γ is the rate of deexcitation of the qubit. Noting that Γ is independent of the probability of the qubit being in the $|1\rangle$ state, p_1 , we can write:

$$\frac{d}{dt}p_1 = -\Gamma p_1. \quad (1.18)$$

The time dependent solution is

$$p_1 = e^{-\Gamma t} = e^{-\frac{t}{T_1}} \quad (1.19)$$

Hence our qubit decays to the ground state with characteristic time $T_1 = \frac{1}{\Gamma}$.

1.3.3 Depolarization: Q

Quoting losses in terms of T_1 comes with drawbacks. To demonstrate this, consider a lossy spring which dissipates energy η every time it oscillates. Our goal is to attach a mass to this spring, forming an oscillator, and reduce the losses in the friction-filled system. At first glance, a clever student motivated to increase T_1 might think to quadruple the weight on the spring, doubling its period and likewise its T_1 . However, the characteristic timescale of the spring has also increased—for example if there are more than one coupled oscillators in the picture, their timescale of interaction (i.e. gate speed) has increased.

A way to eliminate this ambiguity in the T_1 loss metric is to compare the loss timescale to the oscillation timescale, defining the quality factor, Q :

$$Q \equiv \frac{T_1}{T_{oscillation}/2\pi} = T_1 \omega_{0,1} \quad (1.20)$$

Accordingly, Q is a measure of the loss per oscillation.

1.3.4 Decoherence: T_2

Next consider noise in $\phi(t)$. The time dependence of the phase is driven by the energy level splitting of the qubit (see equation 1.16). Any spurious perturbations to $\omega_{0,1}$ will change the phase from the desired value. Intuitively, decoherence adds a range of uncertainty in

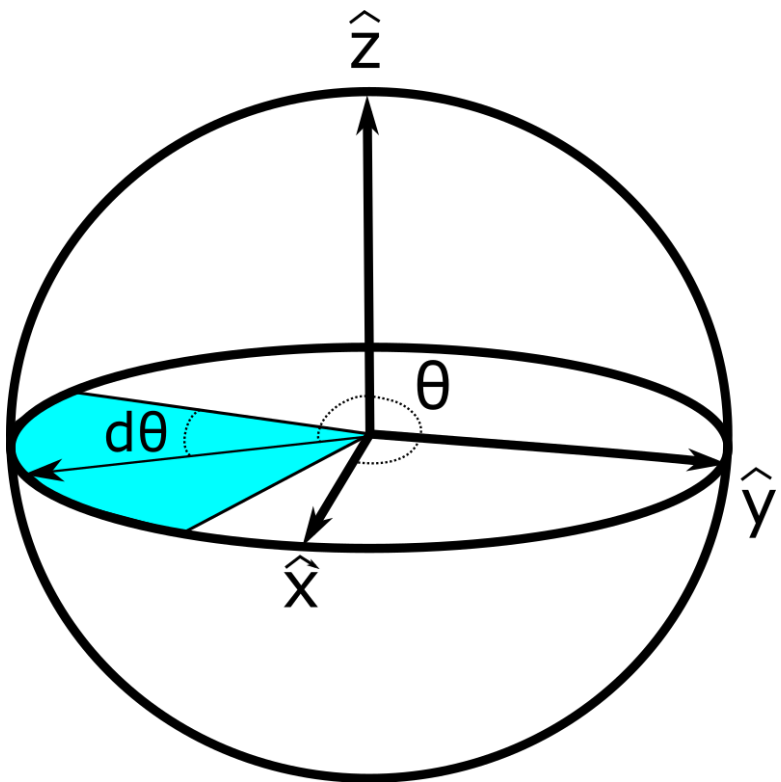


Figure 1.5: **Dephasing on the Bloch Sphere.** Dephasing takes a single vector at angle θ on the equator and adds uncertainty $d\theta$. The blue region represents the spread of possible states the qubit could be in after dephasing.

any value of θ (figure 1.5).

To quantify this uncertainty in θ , suppose we initialize a qubit on the equator then apply a \hat{z} -rotation, $R_z(\theta)$ (which simulates a brief change in resonance frequency). The overlap with the initial state is given by:

$$\eta(\theta) \equiv \frac{1}{2}(\langle 0| + \langle 1|)(|0\rangle \langle 0| + e^{i\theta} |1\rangle \langle 1|)(|0\rangle + |1\rangle) = \frac{1}{2}(1 + e^{i\theta}) \quad (1.21)$$

A simplified model of the changing resonant frequency in a real experiment is a series of random $R_z(\theta)$ perturbations with a roughly Gaussian distribution [13]—where the variance v is proportional to the amount of time the qubit is susceptible to the noise, $v = \frac{t}{T_2}$. Therefore if we perform a measurement where we initialize the qubit on the equator, wait for a variable amount of time, and then measure the overlap with the initial state, P_i :

$$\begin{aligned} P_i &= \frac{1}{\sqrt{4\pi\frac{t}{T_2}}} \int_{-\infty}^{\infty} e^{\frac{-\theta^2}{4t/T_2}} \eta(\theta) d\theta \\ &= \frac{1}{2}(1 + e^{\frac{-t}{T_2}}). \end{aligned} \quad (1.22)$$

The likelihood of the qubit being found in the initialized state on the equator decays with characteristic time T_2 —called the decoherence time.

1.4 Coherence Times and the Bigger Picture

How high do T_1 and T_2 need to be for a processor to be able to perform useful quantum computations? There is a lot of ambiguity in this question, starting with the definition of a “useful” computation. As an example, the Google Quantum AI team used a 53 qubit quantum processor to significantly speed up algorithms compared to classical computers [14], however the practical applications of this algorithm are unclear.

Consider what it might look like to run an algorithm. The qubits will be initialized into certain states, a sequence of gates between the qubits will be executed, and then the states of some qubits will be read. If the runtime of this set of steps is longer than the coherence of the qubits, the information might decay in the middle of the algorithm! To

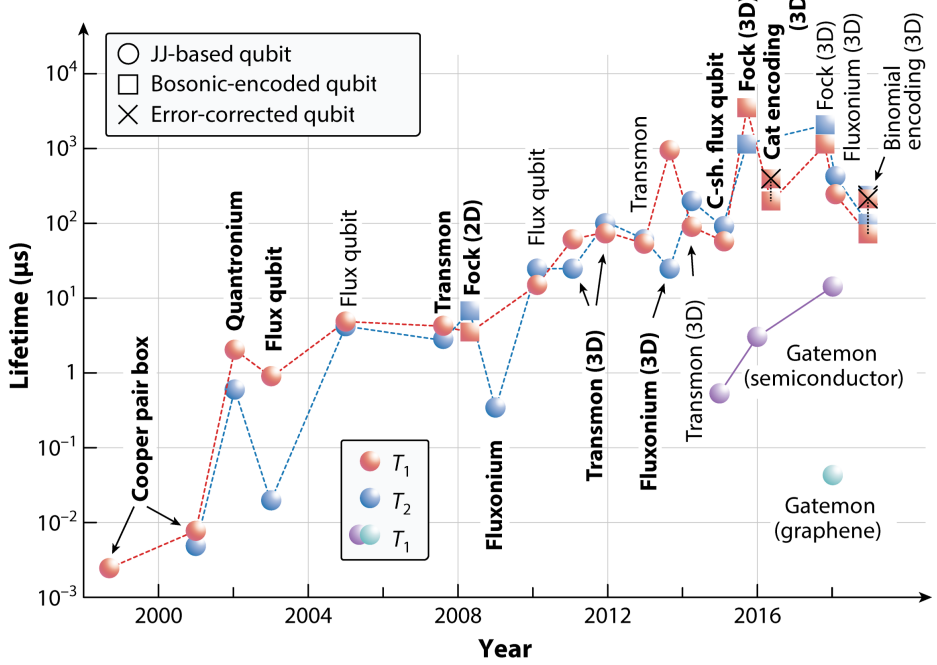


Figure 1.6: **History of T_1 and T_2 .** Reproduced from [17].

mitigate this, quantum error correction schemes have been devised that can correct for bit and phase flips during computations [15]. However, these schemes require significant hardware overhead—in many of them, multiple physical qubits are connected to make a single logical qubit which never decoheres. The higher the likelihood for error, the more qubits are required to make a logical qubit. However we can at least ask: given an error correction scheme and number of qubits, what is the maximum error per physical qubit that can be corrected? This maximal error, called the error correcting threshold, is the sum of all possible errors, but some of the most significant are depolarization and decoherence.

Accordingly there's not a hard target for T_1 and T_2 . Instead, as T_1 and T_2 increase, the complexity and cost of quantum processors is reduced. For reference, logical operations were successfully realized on a 7 transmon processor with T_1 ranging from 27-102 μ s and T_2 ranging from 55-117 μ s [16].

1.4.1 History of T_1

The first coherence measurement of a superconducting qubit was published by Nakamura et al. in 1999 [18]. Measuring the predecessor of the transmon, a Cooper-pair box, they quoted a coherence time of roughly 2 ns, though don't quote T_1 . As shown in figure 1.6, steady progress in increasing T_1 was made throughout the next decade and a half on the transmon and similar qubits. However, before the work in this thesis the published planar transmon T_1 peaked at $114 \mu\text{s}$ [19]. The increases beyond this lifetime in figure 1.6 rely on three dimensional geometries that are significantly larger than planar transmons and have different paths to scalability [20, 21], so won't be considered here.

1.5 Thesis Overview

This thesis explores how to reduce the losses in superconducting devices, primarily through materials. Chapter 2 summarizes many relevant phenomenon that can limit T_1 . Chapter 3 focuses on how qubit materials affect these losses, as well as how to probe these materials properties. We then experimentally demonstrate the dependence of depolarization on materials in chapter 4, where we show that switching from niobium to tantalum transmon capacitor pads significantly increases T_1 . Finally, we explore the loss mechanisms in these transmons by measuring a simpler resonator geometry in chapter 5.

Chapter 2

Sources of Loss

2.1 Introduction

In this chapter we will review the causes and signatures of some of the largest sources of loss in superconducting qubits. We will then give an order-of-magnitude comparison of the T_1 limit expected from these sources.

2.2 Classical Dielectric Loss

As light propagates through a material a portion of the energy is absorbed. Likewise, if any part of a qubit's energy is stored in a dielectric, energy will decay into that material. To quantify this loss, we define the loss tangent: if all of a qubit's electric field was stored in a single dielectric which was the sole source of loss:

$$\frac{1}{Q} \equiv \tan(\delta) \quad (2.1)$$

Superconducting qubits are made of many materials. Therefore we define a weighted sum of the losses:

$$\frac{1}{Q} = \sum_i p_i \tan(\delta_i) \quad (2.2)$$

where the weighting coefficients are called the “participation ratio”, defined as:

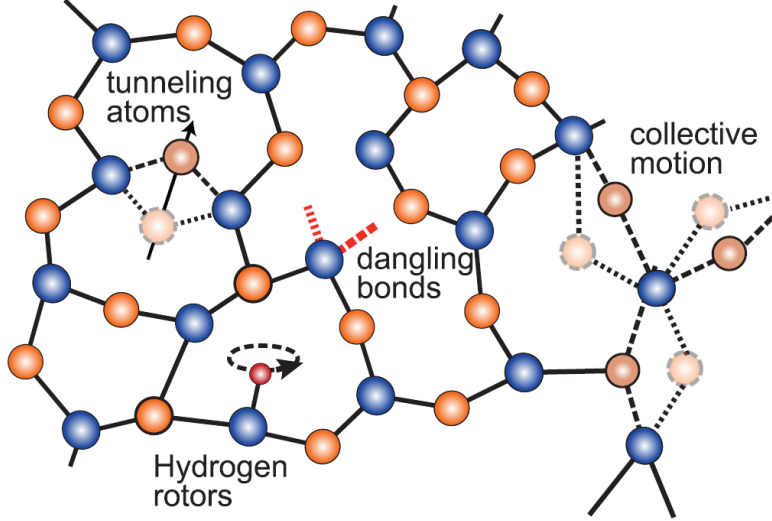


Figure 2.1: Possible Sources of Two-Level System (TLS) Loss. Several proposed microscopic mechanisms that may create quantum objects with two states. Figure reproduced from [24].

$$p_i = \frac{\text{energy stored in } i^{\text{th}} \text{ dielectric}}{\text{net energy}} = \frac{\int \epsilon_i E^2 dV_i}{\sum_j \int \epsilon_j E^2 dV_j} \quad (2.3)$$

In most two-dimensional qubit designs the bulk substrate has the largest participation ratio—on the order of 90% (see appendix F). Accordingly, it’s crucial that the substrate has a low $\tan(\delta)$. For reference, a rough estimate of the loss tangent of sapphire is $2 * 10^{-8}$ [22], leading to a Q limit of roughly $50 * 10^6$. However, the exact loss tangent of the sapphire is a topic of significant research. In comparison, the loss tangent of silicon may be an order of magnitude higher [22], limiting Q to roughly $5 * 10^6$ —which is close to the qubit quality factors currently being measured!

Similarly to the bulk sapphire, we can define participation ratios of the several-nanometer thick amorphous regions at interfaces. However because these interfaces likely host two-level systems we will hold their discussion until section 2.3.8.

Several methods exist to simulate participation ratios, but the most commonly used is explained in [23] (and discussed in appendix F).

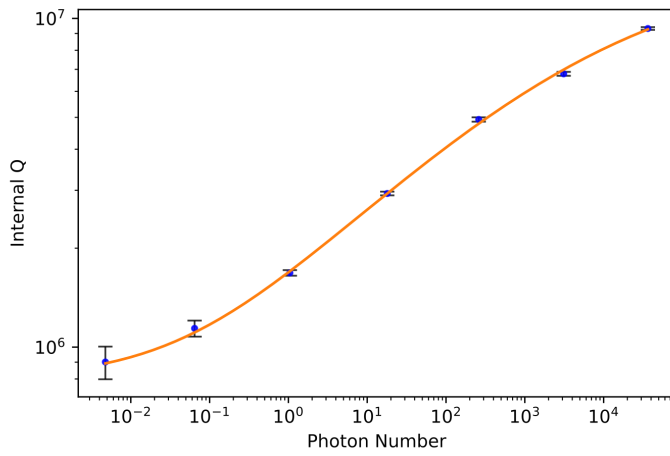


Figure 2.2: **Photon Number Dependence of Loss.** The quality factor (“internal” denotes that any losses due to the measurement lines have been omitted) of a resonator depends on the number of photons injected. This is a signature of saturation. The line of best fit is from equation 2.51.

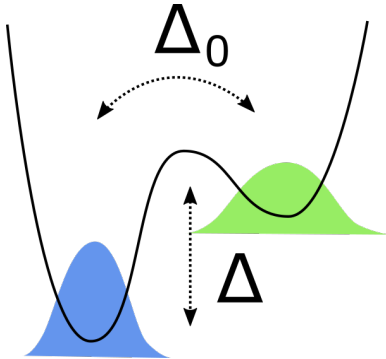


Figure 2.3: **TLS Overview.** Generalized model of a two-level system. There are two energy wells, each of which have a quantum state localized at the bottom (the blue and green wave functions). The energy difference between the states is Δ and the tunneling amplitude is Δ_0 .

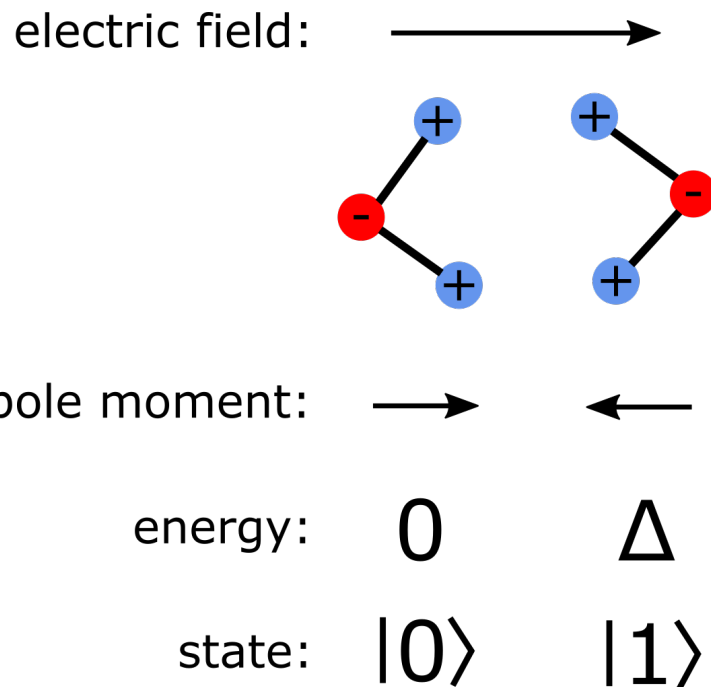


Figure 2.4: **Example Two-Level System.** The left and right columns depict two possible states of a toy model of a two-level system, formed by a negatively charged ion tunneling between two positions relative to two positively charged ions. The externally applied electric field remains constant between both cases, giving the right column a higher energy.

2.3 Two-Level Systems (TLS)

Surprisingly, measurements of the losses in superconducting resonators often highly depend on the number of photons injected into the system (an example is shown in figure 2.2). As the number of photons increases, the loss per photon decreases. Another way to think of this is that the first few photons in a resonator “fill up”—or saturate—the paths photons can decay into.

While the exact microscopic source of this saturable loss remains elusive, the decay observed in many experiments is consistent with spurious fluctuating quantum oscillators with two possible states [24–26]. Several proposals for the source of these “two-level systems” (TLS’s) include tunneling atoms in amorphous materials, unpassivated electrons with extra degrees of freedom, and hydrogen defects (figure 2.1) [24]. A toy model of the states and energies of a TLS is given in figure 2.4.

A generalized two level system has two quantum states with energy splitting Δ , separated by an energy barrier with tunneling matrix element Δ_0 (figure 2.3).

$$H = \frac{1}{2} \begin{bmatrix} -\Delta & \Delta_0 \\ \Delta_0 & \Delta \end{bmatrix} \quad (2.4)$$

Diagonalizing this matrix gives a significantly simpler Hamiltonian:

$$\begin{aligned} H &= \frac{1}{2}\epsilon\sigma_z \\ \epsilon &= \sqrt{\Delta^2 + \Delta_0^2} \end{aligned} \quad (2.5)$$

where σ_z is the Pauli-z matrix. Lastly, we need to consider how to couple to a TLS. Assuming capacitive coupling (but a similar argument could be made for other types of couplings), the electric field of the qubit at the position of the two-level system, \vec{E} , couples via the dipole moment of the TLS, \vec{d} (in the original basis):

$$H_1 = \frac{1}{2} \begin{bmatrix} \vec{E} \cdot \vec{d} & 0 \\ 0 & -\vec{E} \cdot \vec{d} \end{bmatrix} \quad (2.6)$$

Transitioning this to the basis that diagonalizes the TLS:

$$H_1 = \frac{\vec{E} \cdot \vec{d}}{\epsilon} (\sigma_Z \Delta - \sigma_X \Delta_0) \quad (2.7)$$

The full Hamiltonian is then

$$H = \left(\frac{1}{2} \epsilon + \frac{\vec{E} \cdot \vec{d} \Delta}{\epsilon} \right) \sigma_Z - \frac{\vec{E} \cdot \vec{d} \Delta_0}{\epsilon} \sigma_X. \quad (2.8)$$

In order to write the full Hamiltonian of a resonator (or a qubit) coupled to a TLS, note that the electric field in a capacitor is proportional to the stored charge. From equation 1.4 we can write q , and likewise \vec{E} , in terms of ladder operators:

$$\vec{E} = \vec{\beta} (a + a^\dagger) \quad (2.9)$$

The resonator-TLS Hamiltonian is then (using equation 1.5)

$$H_{Resonator-TLS} = \hbar \Omega (\hat{a}^\dagger \hat{a} + \frac{1}{2}) + \frac{\epsilon}{2} \sigma_{Z,TLS} + \frac{\vec{\beta} \cdot \vec{d}}{\epsilon} (a + a^\dagger) (\Delta \sigma_Z - \Delta_0 \sigma_X) \quad (2.10)$$

From this we note that if the resonator and TLS have a similar frequency, they can swap excitations (if the systems are far detuned the last term can be ignored under the rotating wave approximation). The TLS can then continue to Rabi flop with the qubit (discussed in the next section) or decay, coupling the qubit to the mechanism that causes the TLS to lose excitations.

2.3.1 Evidence for Strongly Coupled Individual TLS

Even though we don't know the microscopic mechanism that creates a TLS, there is significant evidence hinting at their existence. Some experiments [27, 28] are able to tune their qubits in and out of resonance with frequency-localized TLS. The avoided crossings witnessed in these devices suggest not only the existence of the TLS, but moreover that they are coherent enough to hybridize with a qubit.

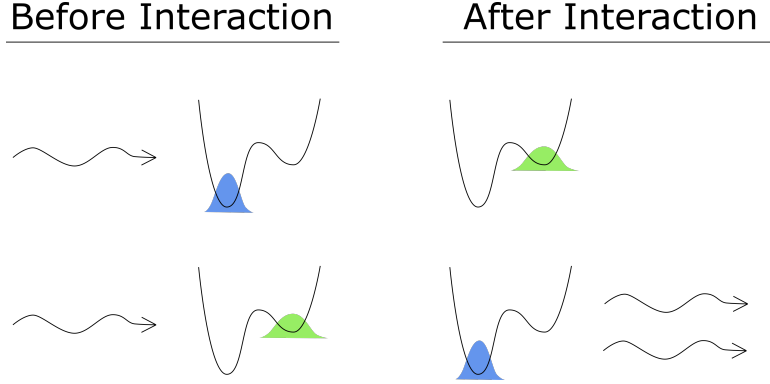


Figure 2.5: **Summary of TLS-Photon Interactions.** When a TLS is in the ground state, it is able to absorb a photon (top row). However, when the TLS is in the excited state, stimulated emission can occur, where the TLS relaxes and emits another photon (bottom row).

2.3.2 TLS Saturation

A key indicator of TLS loss is saturation: losses that change with the number of excited two-level systems. To understand this phenomenon, caused by the last term of equation 2.10, suppose we have a single TLS coupled to a resonator. If the TLS is in its ground state it can absorb a photon from the resonator (top row of figure 2.5). However, if the TLS is in the excited state and interacts with a photon, stimulated emission can occur: the TLS emits a photon, increasing the number of excitations in the resonator (bottom row of 2.5)!

Accordingly, qubit losses should scale with the number of ground-state TLS. Spiecker et al. [29] used a clever pulse scheme that allowed them to excite individual TLS before measuring T_1 . As they excited more TLS, their T_1 increased. However, this pulse scheme is difficult to implement on qubits and not possible to implement on a typical resonator device. Instead, there are two other heavily used methods to excite TLS and subsequently reduce qubit or resonator decay:

Increase Photon Number

Suppose there are t TLS that are coupled to a resonator. If the number of photons in the resonator, \bar{n} , is much greater than t , then at most t of the photons will decay into the TLS (for simplicity ignore TLS lifetimes). However, the other roughly $\bar{n} - t$ photons

won't experience TLS loss ¹. Since the quality factor is the device loss averaged over every photon, in net we see an increase in Q.

Increase Temperature

If the TLS are well thermalized to the phonon temperature, T , the number of thermally excited TLS scales with $e^{-\frac{\epsilon}{k_b T}}$. Heating the device therefore turns potential sources of loss into sites of possible stimulated emission.

2.3.3 Empirical Saturation Models

If a qubit is limited by both TLS loss and another non-power or temperature dependent decay mechanism, we can back out the relative contribution of each loss source by measuring the increase in Q from saturation. To do so we first need analytic models for TLS saturation as a function of photon number and temperature.

To gain intuition, we will first derive a majority of the formula for temperature saturation of TLS with a classical argument. Then we will add corrections to this with a full quantum model. Alternative derivations [26] solely use the Bloch equations.

Classical TLS Coupled to a Resonator: Temperature Saturation

Following [30], consider a resonator of frequency ω_0 coupled to N two-level systems, N_+ of which are in the excited state and N_- of which are in the ground state. Assuming the TLS's are in thermal equilibrium with the environment, we know:

$$\begin{aligned} N &= N_+ + N_- \\ \frac{N_+}{N_-} &= e^{\frac{-\hbar\omega_0}{k_b T}} \end{aligned} \tag{2.11}$$

To determine the resonator losses, suppose we send in a resonant pulse which causes each TLS to have probability per time W of flipping. Noting that transitions from state $|0\rangle$ to $|1\rangle$ absorb energy and $|1\rangle$ to $|0\rangle$ emit energy:

¹Though the $\bar{n} - t$ photons may induce stimulated emission causing a TLS to again extract another photon from the system, the net number of photons stays unchanged.

$$\begin{aligned} power\ absorbed &= WN_- \hbar \omega_0 \\ power\ emitted &= WN_+ \hbar \omega_0 \end{aligned} \quad (2.12)$$

$$net\ loss = W \hbar \omega_0 (N_- - N_+). \quad (2.13)$$

Equation 2.13 highlights how to determine the effects of temperature and photon number on resonator losses—by first calculating the effect on population inversion.

Note that since we're in thermal equilibrium, we can simplify equation 2.13 with equation 2.11:

$$\begin{aligned} N &= N_+ + N_- = N_- (e^{-\frac{\hbar \omega_0}{k_b T}} + 1) \\ \longrightarrow N_- &= \frac{N}{e^{-\frac{\hbar \omega_0}{k_b T}} + 1} \end{aligned} \quad (2.14)$$

$$\begin{aligned} N_- - N_+ &= N_- (1 - e^{-\frac{\hbar \omega_0}{k_b T}}) \\ &= N \frac{1 - e^{-\frac{\hbar \omega_0}{k_b T}}}{e^{-\frac{\hbar \omega_0}{k_b T}} + 1} \\ &= N \tanh\left(\frac{\hbar \omega_0}{2 k_b T}\right) \end{aligned} \quad (2.15)$$

Therefore the net loss is:

$$Net\ Loss = W N \hbar \omega_0 \tanh\left(\frac{\hbar \omega_0}{2 k_b T}\right) \quad (2.16)$$

As we increase the temperature, the losses are reduced (see figure 2.6).

2.3.4 Quantum Corrections: Photon Number (and Extra Temperature) Dependencies

Mainly following [25], consider an individual TLS with state function

$$|\Psi\rangle = a_0 |0\rangle + a_1 e^{-i\omega_0 t} |1\rangle \quad (2.17)$$

The classical analysis in the previous section neglected the effects of saturation on

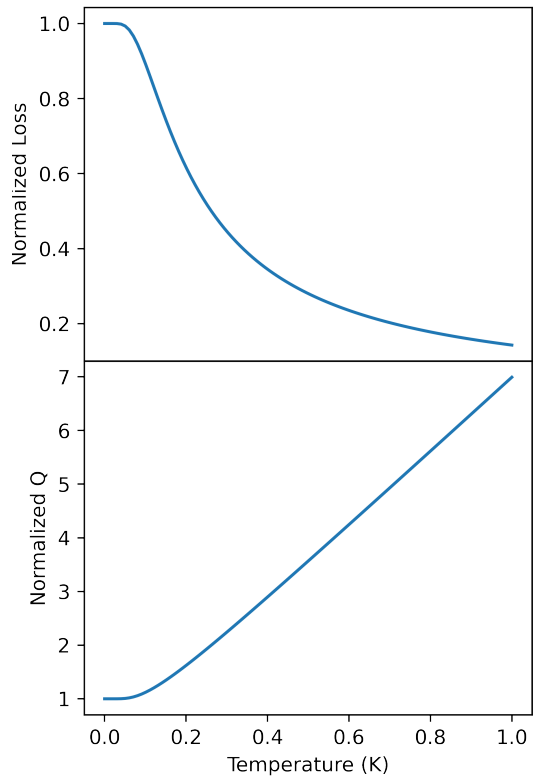


Figure 2.6: **Classical Temperature Dependence of TLS Loss.** Normalized TLS loss and quality factor (inverse loss) as a function of temperature when accounting for classical TLS saturation (equation 2.16).

the T_2 of the TLS. Here we will derive the change in T_2 and how that affects device loss. To do so, we will again start by considering the steady state population difference $w \equiv |a_0|^2 - |a_1|^2$, as previously done in equation 2.13. We will first calculate the time dependencies of a_0 and a_1 .

First, suppose a TLS is capacitively coupled to a resonator, creating a perturbation to the time dependence of the TLS state:

$$(H_0 + H_{int}(t)) |\Psi\rangle = i\hbar \frac{d}{dt} \Psi \quad (2.18)$$

$$\begin{aligned} \dot{a}_0 &= \frac{1}{i\hbar} (\langle 0 | H_{int}(t) | 0 \rangle a_0 + \langle 0 | H_{int}(t) | 1 \rangle a_1 e^{-i\omega_0 t}) \\ \dot{a}_1 &= \frac{1}{i\hbar} (\langle 0 | H_{int}(t) | 1 \rangle a_0 e^{i\omega_0 t} + \langle 1 | H_{int}(t) | 1 \rangle a_1). \end{aligned} \quad (2.19)$$

If the electric field from the resonator at the position of the TLS is $E(t)$ then we define

$$\langle 0 | H_{int}(t) | 1 \rangle = -p_{01} E(t) \quad (2.20)$$

For simplicity we assume Δ in equation 2.10 is 0, giving:

$$\langle 0 | H_{int}(t) | 0 \rangle = \langle 1 | H_{int}(t) | 1 \rangle = 0. \quad (2.21)$$

Combining equations 2.19, 2.20, and 2.21 gives

$$\begin{aligned} \dot{a}_0 &= \frac{-p_{01} E(t)}{i\hbar} a_1 e^{-i\omega_0 t} \\ \dot{a}_1 &= \frac{-p_{01} E(t)}{i\hbar} a_0 e^{i\omega_0 t}. \end{aligned} \quad (2.22)$$

This allows us to write the time dependence of w :

$$\dot{w} = \frac{2p_{01}E(t)}{i\hbar} (a_1 a_0^* e^{-i\omega_0 t} - a_0 a_1^* e^{i\omega_0 t}) \equiv \frac{-2E(t)p_{01}}{\hbar} v \quad (2.23)$$

where

$$v \equiv i(a_0 a_1^* e^{i\omega_0 t} - a_1 a_0^* e^{-i\omega_0 t}). \quad (2.24)$$

It is helpful to define one more quantity related to the dipole moment of the TLS, u , before solving the full time dependence:

$$\begin{aligned} \langle \Psi | \frac{H_{int}}{E(t)} | \Psi \rangle &= \langle 0 | \frac{H_{int}}{E(t)} | 0 \rangle |a_0|^2 + \langle 1 | \frac{H_{int}}{E(t)} | 1 \rangle |a_1|^2 + p_{01}(a_0 a_1^* e^{i\omega_0 t} + a_1 a_0^* e^{-i\omega_0 t}) \\ &= p_{01} \underbrace{(a_0 a_1^* e^{i\omega_0 t} + a_1 a_0^* e^{-i\omega_0 t})}_{\equiv u} \end{aligned} \quad (2.25)$$

Conveniently, the time dependence of u , after a few steps of algebra, is

$$\dot{u} = i\omega_0(a_0 a_1^* e^{i\omega_0 t} - a_1 a_0^* e^{-i\omega_0 t}) = \omega_0 v. \quad (2.26)$$

We will compute the simultaneous time evolution of u , v , and w . To do so we will first compute the time derivative of v :

$$\begin{aligned} \dot{v} &= -\omega_0(a_0 a_1^* e^{i\omega_0 t} + a_1 a_0^* e^{-i\omega_0 t}) + \frac{2p_{01}E(t)}{\hbar}(|a_0|^2 - |a_1|^2) \\ &= -\omega_0 u + \frac{2p_{01}E(t)}{\hbar} w \end{aligned} \quad (2.27)$$

So far we have only considered a lossless TLS. To introduce decay, we add phenomenological decay parameters T_1 and T_2 for terms without and with phase dependence, respectively. We arrive at the Bloch equations:

$$\dot{u} = \frac{-u}{T_2} + \omega_0 v \quad (2.28)$$

$$\dot{v} = \frac{-v}{T_2} - \omega_0 u + \frac{2E(t)p_{01}}{\hbar} w \quad (2.29)$$

$$\dot{w} = -\frac{w - \underline{w}}{T_1} - \frac{2p_{01}E(t)}{\hbar} v \quad (2.30)$$

where \underline{w} is a non-driven steady state population of w (for example from a non-zero temperature).

To solve these equations, define:

$$\begin{aligned}\dot{\rho} &= \dot{u} + i\dot{v} \\ &= -\frac{\rho}{T_2} - i\omega_0\rho + \frac{2iE(t)p_{01}}{\hbar}w\end{aligned}\tag{2.31}$$

Assuming a sinusoidal drive $E(t) = E_0(e^{-i\omega t} + e^{i\omega t})$ and that w has reached its driven steady state solution, \bar{w} , if we write $\rho = \rho_0e^{-i\omega t}$ we find (ignoring fast rotating terms):

$$-i\omega\rho_0e^{-i\omega t} = -\left(\frac{1}{T_2} + i\omega_0\right)\rho_0e^{-i\omega t} + \frac{2iE_0e^{-i\omega t}p_{01}}{\hbar}\bar{w}.\tag{2.32}$$

solving for ρ_0 :

$$\rho_0 = \frac{2iE_0p_{01}\bar{w}}{\hbar} \frac{1}{\frac{1}{T_2}(1 + iT_2(\omega_0 - \omega))}\tag{2.33}$$

Isolating u :

$$\begin{aligned}u_0 &= Re(\rho_0) \\ &= \frac{2E_0p_{01}\bar{w}T_2}{\hbar} \frac{T_2(\omega_0 - \omega)}{1 + T_2^2(\omega - \omega_0)^2}\end{aligned}\tag{2.34}$$

Lastly, to solve for \bar{w} , we find the steady state solution of equation 2.30:

$$\frac{\bar{w} - \underline{w}}{T_1} = \frac{-2p_{01}E(t)}{\hbar}v_0e^{-i\omega t}\tag{2.35}$$

which after some algebra gives

$$\bar{w} = \underline{w} \frac{1}{1 + \frac{4p_{01}^2E_0^2T_2T_1}{\hbar^2} \frac{1}{1 + T_2^2(\omega - \omega_0)^2}}.\tag{2.36}$$

Combining equations 2.34 and 2.36 gives

$$u_0 = \frac{2E_0p_{01}\underline{w}}{\hbar} \frac{\omega_0 - \omega}{\underbrace{\frac{1}{T_2^2} + \frac{4p_{01}^2E_0^2T_1}{\hbar^2T_2}}_{variance/4} + \underbrace{\frac{(\omega - \omega_0)^2}{1 + T_2^2(\omega - \omega_0)^2}}_{detuning\ term}}.\tag{2.37}$$

Note that as E_0 increases from 0, the bracketed variance term transitions from

$$\frac{1}{T_2^2} \longrightarrow \frac{1}{T_2^2} + \frac{4p_{01}^2 E_0^2 T_1}{\hbar^2 T_2}. \quad (2.38)$$

We define:

$$\eta \equiv \frac{T_{2,E_0=0}}{T_{2,E_0 \neq 0}} = \sqrt{1 + \frac{4p_{01}^2 E_0^2 T_1 T_{2,E_0=0}}{\hbar^2}} \quad (2.39)$$

Taking a step back, consider how η affects the net TLS loss:

$$\Gamma_{TLS} \sim \sum_{i=1}^{n_{TLS}} \Gamma_i \quad (2.40)$$

where n_{TLS} is the number of TLS that interact with a resonator and Γ_i is the loss from the i^{th} interacting TLS. We will consider the effects from η on n_{TLS} and Γ_i separately.

n_{TLS} will be proportional to the number of TLS with linewidths overlapping the device frequency. Accordingly, $n_{TLS} \sim \frac{1}{T_2}$ and therefore as E_0 increases, $n_{TLS} \sim \eta$.

On the other hand, the changing TLS T_2 will modify the strength of interaction between each of the n_{TLS} and the resonator. Intuitively, for many of the nearly-resonant TLS the bracketed detuning term in equation 2.37 will be small, causing the strength of the effective dipole moment $p_{01} u_0 \sim T_2^2 \sim \frac{1}{\eta^2}$.

The net effect gives a loss that scales with $\frac{1}{\eta}$. Combining this with the classical analysis, equation 2.16, gives the total TLS loss, Γ_{TLS} :

$$\Gamma_{TLS} = \Gamma_{TLS,0} \frac{\tanh(\frac{\hbar\omega_0}{2k_b T})}{\sqrt{1 + \frac{4p_{01}^2 E_0^2 T_1 T_{2,E_0=0}}{\hbar^2}}} \quad (2.41)$$

2.3.5 Temperature Dependence of TLS T_1 and T_2

To find the full temperature dependence of TLS loss, we need to find how the TLS coherence and depolarization times in equation 2.41 change with temperature.

T_1

If a TLS is thermalized to its environment it will be coupled to thermal phonons. Using a similar argument as section 2.3.3,

$$T_{1,TLS} \sim \tanh\left(\frac{\hbar\omega}{2k_b T}\right). \quad (2.42)$$

The prefactor can be found in [26].

T_2

We don't know the microscopic form of TLS so we can't precisely predict the temperature dependence of $T_{2,TLS}$. However, we can posit a testable hypothesis which we will see in chapter 5 fits the data reasonably well.

T_2 is a measure of the uncertainty in the precession frequency of the TLS, which depends on the uncertainty in the TLS energy splitting (see section 1.3.4). Accordingly we will shift our focus to understanding TLS frequency fluctuations.

Our primary assumption is that a TLS is coupled to at least several other two-level systems which we will call thermal fluctuators (TF's) [31] for reasons that will soon become clear. The TF's are thermally active, and we assume that the state of the TF changes the frequency of the TLS:

$$\Delta f = \sum_i m_i \delta_i \quad (2.43)$$

where Δf is the change from the bare TLS frequency, m_i is the contribution from the i^{th} TF, and δ_i is a random variable that models the state of the i^{th} TF and can take the values -1 or 1 . The variance in frequency is:

$$\begin{aligned} v_{\Delta f} &\equiv \langle (\Delta f)^2 \rangle - \langle \Delta f \rangle^2 \\ &= m^2 \langle \left(\sum_i \delta_i \right)^2 \rangle \\ &= m^2 \langle \sum_{ij} \delta_i \delta_j \rangle \\ &= m^2 \sum_{ij} \langle \delta_i \delta_j \rangle \end{aligned} \quad (2.44)$$

where we have assumed for simplicity that $m_i = m$ for all i . Noting that

$$\langle \delta_i \delta_j \rangle = \begin{cases} 0, & i \neq j \\ 1, & i = j \end{cases} \quad (2.45)$$

we find

$$v_{\Delta f} = m^2 n \quad (2.46)$$

if there are n coupled TF.

Next, we need to find how n depends on temperature. Intuitively, TF fluctuations should follow a Boltzmann probability distribution. We will make the rough approximation that a TF with energy E will become thermally active when $E = \gamma k_b T$ for some constant γ . Following Burnett et al. [32], if we make the further assumption that the density of TF's, ρ , has energy dependence $\rho(E) = rE^\mu$ for some r and μ , then

$$\begin{aligned} n &= \int_0^{\gamma T} \rho(E) \frac{dE(t)}{dt} dt \\ &= r\gamma^\mu k_b^{1+\mu} \int_0^{\gamma T} t^\mu dt \\ &\sim T^{1+\mu}. \end{aligned} \quad (2.47)$$

Putting equations 2.46 and 2.47 together and defining $\beta_1 \equiv 1 + \mu$:

$$v_{\Delta f} \sim m^2 T^{\beta_1} \quad (2.48)$$

Coming back to the T_2 of our TLS, note from section 1.3.4 that T_2 is inversely proportional to the variance in the angle θ of the random \hat{z} rotations a device undergoes. We can treat perturbations in frequency that last time t as rotations: $\theta = t\Delta f$, and likewise $v_\theta \sim v_{\Delta f}$. Therefore we expect:

$$T_{2,TLS} \sim \frac{1}{T^{\beta_1}}. \quad (2.49)$$

2.3.6 Driving Voltage Correction

Equation 2.41 relies on knowing the electric field in the resonator, E_0 . Instead, we normally send a signal through a nearby transmission line that has a capacitance to the device, populating the resonator mode with n photons. This resonator mode does not necessarily have the same electric field everywhere. To account for this, Wang et al. [33] find that E_0^2 can be replaced in equation 2.41 with

$$\alpha n^{\beta_2}. \quad (2.50)$$

where α and β_2 are phenomenological parameters.

2.3.7 TLS Loss Summary

Combining equations 2.41, 2.42, 2.49, and 2.50:

$$\Gamma_{TLS} = \Gamma_{TLS,0} \frac{\tanh(\frac{\hbar\omega_0}{2k_bT})}{\sqrt{1 + \underbrace{\frac{\tanh(\frac{\hbar\omega}{2k_bT}) n^{\beta_2}}{T^{\beta_1}}}_{D}}} \quad (2.51)$$

where we've grouped all of the constants in the denominator in the term D .

The relative size of the two terms in the denominator dramatically changes the shape of the loss as a function of temperature. If the underbraced term is small (i.e. small $T_{1,TLS}$, $T_{2,TLS}$, n) then the only saturation with temperature occurs from classical temperature saturation (section 2.3.3) through the numerator. This gives a gradual increase in Q with temperature (figure 2.7, large D).

However, if the underbraced term is significant, at low temperatures the primary temperature dependence in Q comes from $\frac{1}{T^{\beta_1/2}}$. This causes low-temperature saturation of Q (figure 2.7, small D). In the limit where the underbraced term is sufficiently large, equation 2.51 can be simplified to:

$$\Gamma_{TLS} \approx \Gamma_{TLS,0} \sqrt{T^{\beta_1} \tanh(\frac{\hbar\omega_0}{2k_bT}) \frac{D}{n^{\beta_2}}} \quad (2.52)$$

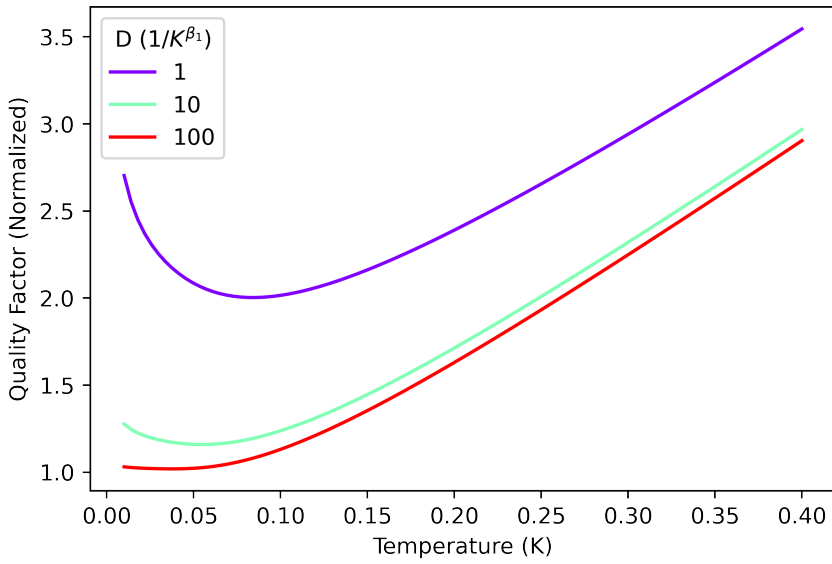


Figure 2.7: **TLS-Limited Quality Factor.** TLS-induced losses as a function of temperature. As D is decreased, the underbraced term of 2.51 becomes significant and adds a low-temperature upturn in quality factor.

2.3.8 Interface Participation Ratios: Microscopic Origins

What is the microscopic mechanism behind classical dielectric loss? A large bath of TLS with a short-lived lifetime (i.e. decay quickly to phonons, etc.) and spanning a large frequency range could absorb photons. To first order the effect of this would be similar to classical microwave loss. However there could be other classical effects at play.

Accordingly a notational shorthand is often used—even though loss at interfaces is likely dominated by two-level systems in some devices [29], an effective loss tangent (see section 2.2) which ignores the frequency inhomogeneity and quantum nature of the decay is employed. To calculate this effective loss tangent of, for example, the metal-air interface, devices can be designed which ideally only vary the participation ratio of the oxide, $p_{\text{metal-air}}$. The change in Q between devices can then be used to calculate the loss tangent [34].

The three main interfaces are shown in figure 2.8 (a). The participation ratio calculation at these interfaces requires integrating over the volume of the interface. Therefore quantifying the thickness of the interface is crucial. One way to do this is through high-

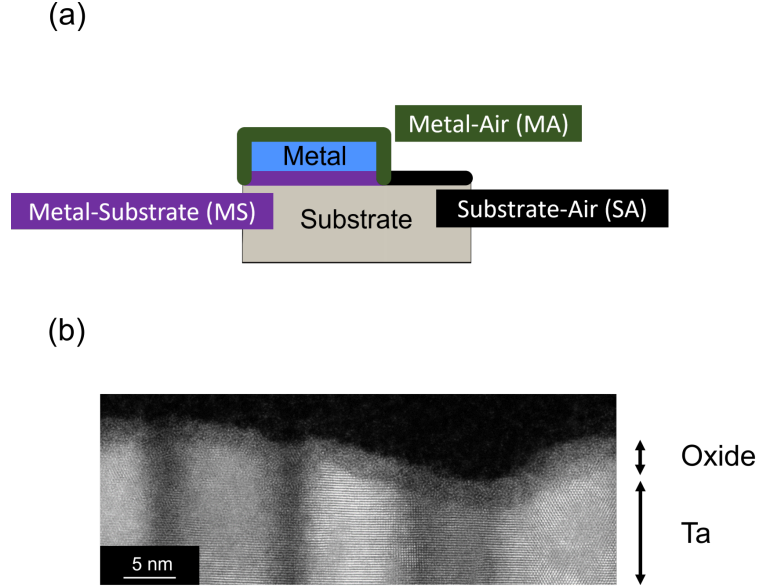


Figure 2.8: **Interface Participation Ratios.** (a) Schematic depicting the location of the three main interfaces. (b) TEM image of the tantalum-air interface. Columnar grains of tantalum are visible, capped by a 2-3 nm oxide.

resolution microscopy (figure 2.8 (b)).

An additional interface that is often overlooked is the oxide in the junction. This roughly $2 * 10^{-4} \mu\text{m}^3$ region has the largest field anywhere in an ideal qubit, but the small volume makes finding a TLS of the correct orientation and frequency less likely. [27] quantified the loss in aluminum junctions by making a qubit with a large junction-oxide participation ratio. They showed that these losses are a similar order of magnitude to the decay observed in our qubits.

2.4 Quasiparticles

Ideally, all of the non-bound electrons in the superconducting metal of a transmon would be partnered into cooper pairs. Unfortunately, there are electrons which remain unpaired—called “quasiparticles”. A consequence of our device being at a finite temperature is a non-zero thermal population of quasiparticles. However, non-thermal quasiparticles generated by the environment are also significant sources of decay. In the following section we will first discuss how quasiparticles induce loss in both resonators and qubits,

then we will focus on the sources that create quasiparticles.

2.4.1 Junction Quasiparticle Losses

First, consider the case where a quasiparticle tunnels across a transmon's junction. A tunneling event changes the charge on each pad, which perturbs the qubit. We can write the charge transfer operator as the exponential of the conjugate variable: $e^{i\frac{\hat{\phi}}{2}}$. Considering both electrons and holes, as well as making the approximations outlined in [35]:

$$H_{perturbation} \sim e^{i\frac{\phi}{2}} - e^{-i\frac{\phi}{2}} \sim \sin(\frac{\phi}{2}). \quad (2.53)$$

Therefore, according to Fermi's golden rule, the transition rate from quasiparticles is

$$\Gamma_{01} \sim \langle 0 | \sin(\frac{\phi}{2}) | 1 \rangle S_{QP}(\omega). \quad (2.54)$$

Both [36, 37] use offset charge sensitive transmons to extract this transition rate.

One route to lowering quasiparticle losses is to reduce the matrix element by engineering the Hamiltonian of new qubit designs. However, if our goal is to make a quantum processor out of transmons then we have to focus on reducing the quasiparticle noise spectral density, $S_{QP}(\omega)$.

2.4.2 Resonator QP Losses

The fields in a resonator propagate into the superconductor a finite penetration depth. Any quasiparticles in this region will experience resistive losses. Properly simulating both the penetration depth and the associated losses for a general case requires numerical integration, though in some cases (including aluminum) the integrals simplify to a simple form [26, 38]:

$$Q_\sigma(\omega, T) \approx \frac{\pi}{4} \frac{e^{\frac{\Delta_0}{k_b T}}}{\sinh(\frac{\hbar\omega}{2k_b T}) K_0(\frac{\hbar\omega}{2k_b T})} \quad (2.55)$$

where Δ_0 is the superconducting gap and K_0 is the modified Bessel function of the

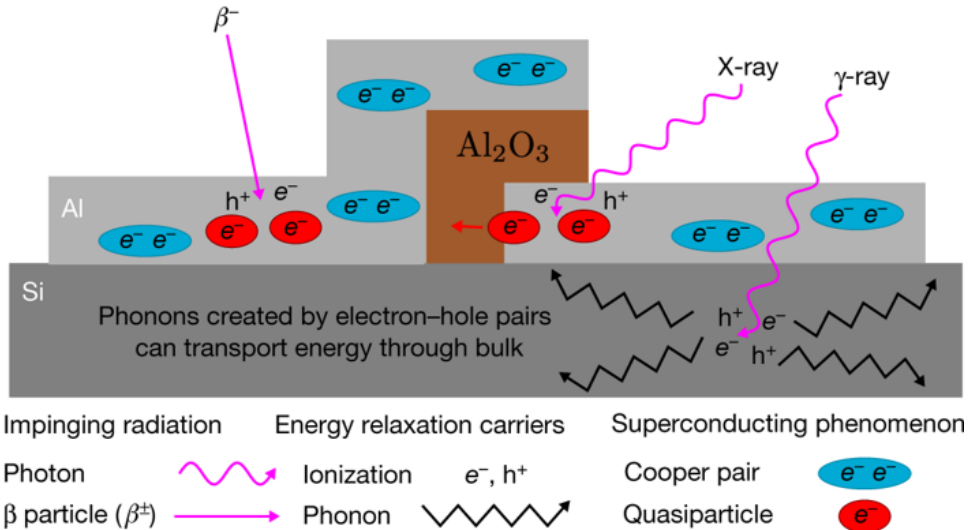


Figure 2.9: **Proposed Quasiparticle Generation Channel.** Figure reproduced from [39].

second kind of order 0.

It is also important to note these resistive quasiparticle losses also affect the pads of transmons. However the quasiparticle losses from the junctions and the surrounding aluminum are more significant because $T_{c,Al} < T_{c,Ta}$.

2.4.3 Sources of Quasiparticles

Number-Conserving Parity Switching (NUPS)

Exposing transmon qubits to ionizing radiation such as β -particles, γ -rays, and X-rays can reduce qubit relaxation times. To demonstrate this, Vepsäläinen et al. [39] measured the T_1 of a transmon as a function of the amount of incident radiation from an in-situ ^{64}Cu source. The losses increased with the amount of radiation. Likewise without the source installed, they attempted to reduce the residual radiation from outside their fridge by surrounding five of six sides of their fridge with lead bricks. This caused a statistically significant decrease in quasiparticle loss.

Vepsäläinen proposed that microscopically, the radiation ionizes electron-hole pairs in the substrate (and metal). These excitations relax via other ionizations and phonons, which then couple to the qubit to break cooper pairs (figure 2.9). This hypothesis is

consistent with recent experiments by Wilen et al. [40]. They look at the correlation between charge noise in transmons separated by increasing distances. The further the distance between two transmons, the smaller the correlations between changes in offset charge. This could be explained by localized ionization events in the substrate and the subsequent phonon cascade, which decays with distance, generating quasiparticles.

2.4.4 Photon-Assisted Parity Switching (PAPS)

Another way quasiparticles can be created is when a spurious photon induces a voltage across the qubit junction. If this photon has enough energy, it can break a Cooper pair and cause a single charge to tunnel across the junction [41]. This theory has been verified in two ways: changing the antennae modes of devices, and examining the flux-dependent parity switching.

Antennae Modes The ability for a transmon to act as an antennae is dependent on its geometry, quantified in [42]. Following this theory, [43] shows the effect of device layout on quasiparticle tunneling rates. [44] demonstrates that the charge switching rate roughly follows the coupling efficiency of a transmon to spurious photons.

Flux-Dependent Parity Switching Diamond et al. [45] measured the parity switching rate of a tunable offset-charge sensitive transmon as a function of qubit frequency. They engineered the device to have a starkly different frequency dependence for PAPS and NUPS. This allowed them to fit the relative contributions of the two processes. They concluded that PAPS and NUPS had similar rates in their device.

2.5 Decay Into Environment: Purcell and Packaging

2.5.1 Purcell Limit

Initializing and reading out a qubit state requires coupling between the qubit and microwave equipment. However, if the qubit is too strongly coupled to its support elec-

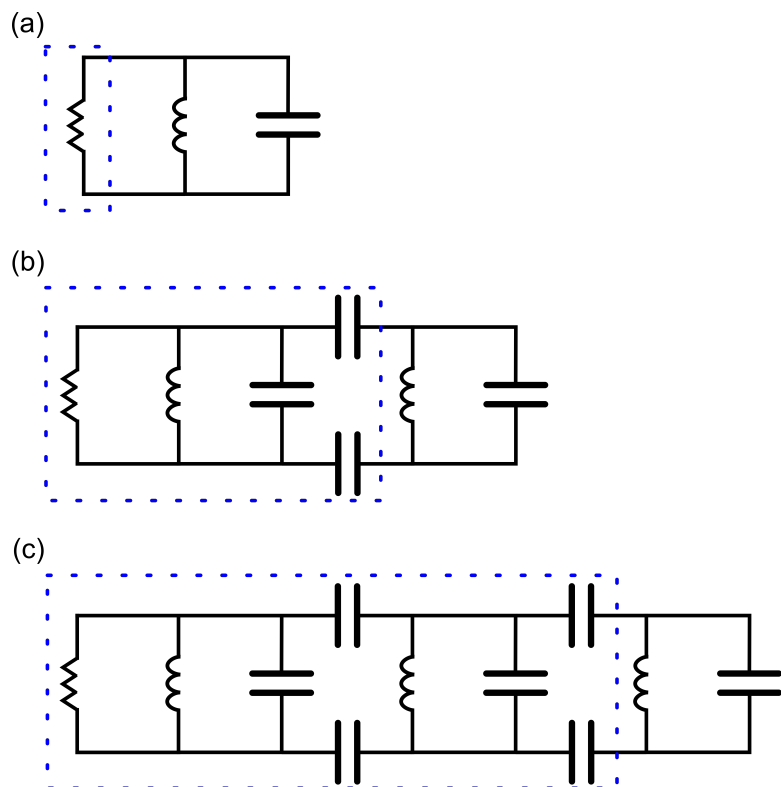


Figure 2.10: **Basics of Purcell Filters.** (a) Schematic of a RLC oscillator. (b) Dispersive readout adds a resonator between the qubit (simplified to an LC oscillator) and the readout electronics, modeled as a resistor. (c) To add extra protection from decay into the readout electronics, an extra resonator which acts as a bandpass filter can be added. In all panels the blue box denotes the qubit's environment.

tronics, the signal loss through these lines could dominate the qubit T_1 . The signal that enters into the waveguides connected to the qubit should never return, in the same way a resistor dissipates energy. Approximating the qubit as an LC oscillator, the measurement equipment add an effective spurious resistance and the calculation of the Purcell limit simplifies to finding the dissipated power.

Unfortunately the system is not as simple as an RLC oscillator (figure 2.10 (a)) with time constant

$$\tau = RC. \quad (2.56)$$

Instead most devices will be capacitively coupled to a resonator, which is then connected to the effective resistance (figure 2.10 (b)) [12]. However, a generalized version of equation 2.56 still holds [46]:

$$\tau = \frac{C}{Re[Y(\omega_q)]} \quad (2.57)$$

where $Y(\omega_q)$ is the admittance of the environment (the blue boxes in figure 2.10). This admittance can be calculated using standard circuit simulation software including Cadence AWR Microwave Office (see appendix E).

If the Purcell limit is too low, the admittance of the environment can be decreased at the qubit frequency. To preserve a fast readout, however, it is important that the admittance at the readout frequency remains high. One method to do this is to add another resonator centered near the readout frequency, which acts as a bandpass filter (figure 2.10 (c)) [47].

2.5.2 Packaging Decay

Most qubits are mounted in metal boxes with dimensions on the order of centimeters—and likewise resonant frequencies in the microwave regime (figure 4.4). This box can be made of normal or superconducting metal, but even the superconducting metal may have an oxide and machining residue. To interface with the chip, a PCB protrudes into this box

with normal metal and large amounts of dielectric. The qubit can either directly couple to these loss sources or couple via the modes of the box (similar to figure 2.10 (b))—in either case the loss can be modeled in a similar way to section 2.5.1.

In order to reduce decay, employing a package that doesn’t have any resonances close to the qubit frequency eliminates loss through box modes. This thesis uses two different packages—a homemade variety (figure 4.4) and the QCage from QDevil APS, which doesn’t have any packaging modes below 18GHz. Preliminary results suggest the commercial packaging may increase resonator Q_{other} in some devices, though more experiments are required to understand the Q_{other} behavior in this sample holder (see section 5.6).

2.6 Other Sources of Loss

2.6.1 Vortex Loss

Local non-superconducting regions can form in type II superconductors as well as sufficiently thin type I films [48]. These non-superconducting regions, each of which contain a single flux quantum of magnetic field, are called vortices. No longer superconducting, as they move they generate loss.

Vortices can be introduced in films by cooling past the device’s T_c in a residual magnetic field. This has been measured for both resonators [33, 49] and qubits [50]. [49] saw a decrease in Q with increasing number of vortices in resonators. Interestingly, [50] initially saw an increase in T_1 as a small number of vortices were introduced, likely because of the vortex quasiparticle trapping power. However, once a significant number of vortices were introduced T_1 decreased.

2.6.2 Quasiparticles Forming TLS

Interestingly we can connect two of our dominant loss sources: quasiparticles that form TLS. [51] noted that the variation in the superconducting gap across a film can create shallow traps for quasiparticles with several energy levels. A quasiparticle in these energy

levels could have TLS-like behavior.

2.7 Comparing Loss Source Contributions

Figuring out which loss source is limiting state-of-the-art devices is critical to increasing coherence times. The focus of chapter 5 is on delineating the strength of the sources of loss. For the time being, we will briefly examine the expected relative contributions.

Two-level systems: Wang et al. found that the T_1 of qubits made with Al and TiN scaled with interface participation ratio, suggesting that interface two-level system loss is significant in these materials. Chapter 5 will quantify the magnitude of TLS loss in tantalum devices.

Quasiparticles: [39, 45] estimate quasiparticles to limit T_1 to 2 ms and 4 ms, respectively. Quasiparticles are important to consider but likely not limiting T_1 .

Classical Dielectric Loss: As noted in section 2.2, rough estimates of the sapphire loss tangent would limit a transmon to a Q of 50 million, which translates to a T_1 of roughly 2 ms. Further measurements of classical dielectric loss are needed to better constrain this estimate, but if the losses are slightly higher then sapphire could be limiting transmon T_1 . Classical sapphire loss is further discussed in section 5.6.

Purcell and Packaging: The Purcell limit of a well designed qubit should not be limiting T_1 (see appendix E.1.2). However, unintentional coupling to the environment is important to consider. As we will see in chapter 5, some resonator devices have losses that are temperature and power independent (and therefore likely either sapphire or packaging related) which limit the quality factor to the low millions ($T_1 \approx 100\mu\text{s}$), though we present ways to mitigate this loss. Regardless, packaging decay is important to keep in mind when designing devices.

Chapter 3

Qubit Materials: Overview

3.1 Introduction

In chapter 2 we saw that many of the transmon loss sources originate in the material (such as dielectric loss) or their effects depend on material properties (such as quasiparticles). Especially important are the natural or fabrication-induced defects near interfaces which may host TLS.

As a starting point in the search for better qubit materials, this chapter first discusses the properties that may reduce materials-related qubit decay. This is not close to exhaustive but rather meant to stimulate further discussion. The second portion of the chapter focuses on how to screen potential qubit materials: an overview of imaging tools is presented.

3.2 Desired Materials Properties: Superconductors

3.2.1 T_c

The superconducting metal in a qubit should operate at a temperature well below its critical temperature, T_c . Otherwise the device may be limited by equilibrium quasiparticles either passing through the junction (section 2.4.1) or resistively dissipating energy (section 2.4.2).

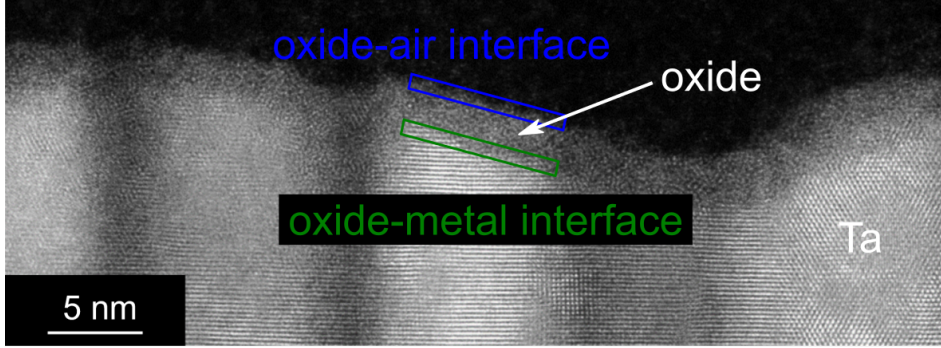


Figure 3.1: **Oxide Interfaces.** TEM image of the oxide on top of tantalum with the oxide interfaces labeled. If an oxide doesn't lattice-match the metal, there may be strain or other non-uniformity at the interface between the layers. Likewise the top of the oxide, without a layer of oxide atoms above to bond to, could have additional unpassivated bonds or adsorption sites.

To estimate the minimal T_c necessary, note that the number of quasiparticles, and quasiparticle loss, roughly scale as $e^{-\alpha \frac{T}{T_c}}$ for some constant α , according to a Boltzmann argument. Equilibrium quasiparticles in aluminum, with a T_c of around 1.3 K, limit qubit T_1 at around 140 mK [20]. If a quantum processor sits at 20 mK the same ratio of $\frac{T}{T_c}$ is achieved with a T_c of 186 mK.

Reducing the T_c to such a low value is risky, however. A scalable quantum processor will likely have a large density of devices and control lines, leading to significant heating. Further, if there is a coupling mechanism between incoming photons and the breaking of cooper pairs, reducing T_c could increase the nonequilibrium quasiparticle generation rate since the energy required to form a quasiparticle would be lower.

3.2.2 Oxide

Aluminum, niobium, tantalum, and many other materials form a several nanometer thick non-crystalline oxide when exposed to air. This oxide likely hosts two-level systems. However, it is important to note that there are three possible locations for TLS around an oxide: at the interface between the bulk and the oxide, inside the oxide itself, and at the interface between the oxide and air (figure 3.1). The following are several properties to consider when evaluating the potential TLS density of a superconductor's interface

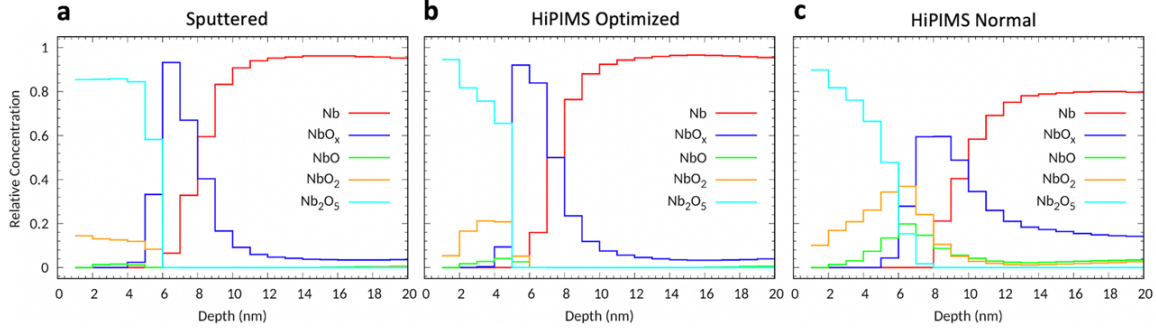


Figure 3.2: Measured Niobium Oxide Composition as a Function of Depth. Depth-dependent oxide composition of three different niobium deposition recipes. The profile was reconstructed from X-ray photoemission spectroscopy data using a maximum-entropy method algorithm. From [52].

with air:

- The more disordered and amorphous the oxide, the more degrees of freedom available to form TLS. A crystalline oxide likely has less possible TLS sites. In this line of thought, a tantalum oxide with one or two suboxide variants is better than a niobium oxide with many suboxides (shown in figure 3.2).
- If the TLS reside in the bulk of the oxide, a thinner oxide has less loss.
- The dielectric constant, ϵ , of the oxide will change the interface's participation ratio. On the one hand the participation ratio has an explicit dependence on ϵ in equation 2.3. On the other hand, a field matching argument [53] shows the primary component of the electric field in the interface will be reduced by a multiple of $\frac{1}{\epsilon}$. Because the participation ratio scales with the square of the field, the net dependence goes as $\frac{1}{\epsilon}$.

3.2.3 Crystallinity and Grain Boundaries

Though we haven't found any significant correlation between grain size and quality factor of resonators in tantalum, it is conceivable that there could be resistive loss at the grain boundaries. Further, the less crystalline a material the more degrees of freedom that could form TLS. However, TLS inside the superconducting metal likely won't couple capacitively but instead could couple inductively to the qubit.

3.2.4 Patterning

Electric field concentrates near sharp features at the etched edge of a film. Ensuring the edges of the capacitor are free of TLS is accordingly crucial. While lift-off processes are a possibility, they have been shown to be lossier than etching processes on some material systems [54]. Therefore, finding a subtractive process that creates clean edges is important. Further, whatever gases used to create these edges should either not affect the oxide or if they do, not increase the TLS density.

3.3 Desired Materials Properties: Substrate

The majority of a two-dimensional transmon's field is stored in the substrate—the participation ratio is about 0.9 (see appendix F). Picking a low loss substrate is critical.

3.3.1 Classical Loss

Most crystalline materials do not have a low enough loss tangent to be used as a substrate. If we assume the substrate participation ratio is 0.9, a loss tangent of 1e-7 would limit the devices quality factor to 10 million, roughly the current state-of-the-art.

3.3.2 Substrate-Air Interface

The substrate-air interface has a participation ratio roughly an order of magnitude higher than the metal-air interface (see appendix F). Ensuring this interface is disorder free reduces the possibility of two-level systems.

If a subtractive etch was used to pattern the superconductor, the substrate-air interface was likely exposed to that etch. This may roughen or change the composition of the interface, especially in the case of plasma etches.

3.3.3 Substrate-Metal Interface

The substrate-metal interface also has a participation ratio roughly an order of magnitude higher than the metal-air interface (see appendix F). If the lattice constants between the substrate and metal don't match, the lowest layers of the metal won't form a perfect crystal structure. Further, it may be important to ensure atoms from the substrate don't migrate from the metal (or the other way around)—especially during any high-temperature steps in the fabrication process.

3.3.4 Substrate Defects

Defects in the substrate could arise during growth or during the thinning and polishing process. Given the significant field in the substrate, crystalline imperfections could host strongly-coupled TLS's.

3.3.5 Dielectric Constant

If the substrate loss tangent is large, the substrate losses can be reduced by lowering the dielectric constant and consequently the participation ratio of the substrate (equation 2.3). Likewise, from a boundary matching argument [53], the field in the substrate-metal and substrate-air interfaces normal to the plane of the interface is proportional to $\epsilon_{substrate}$. Therefore, reducing the dielectric constant of the substrate can significantly reduce potentially lossy participation ratios.

On the other hand, if the substrate, substrate-metal, and substrate-air interfaces are all clean of TLS, increasing $\epsilon_{substrate}$ can reduce the participation of the metal-air interface by increasing the denominator of equation 2.3.

3.3.6 Quasiparticle Coupling

As discussed in section 2.4.3, high-energy particles and photons can interact with the substrate and create a cascade of events that generate quasiparticles. Reducing the substrate thickness can reduce the number of high-energy impacts, and likewise exploring materials

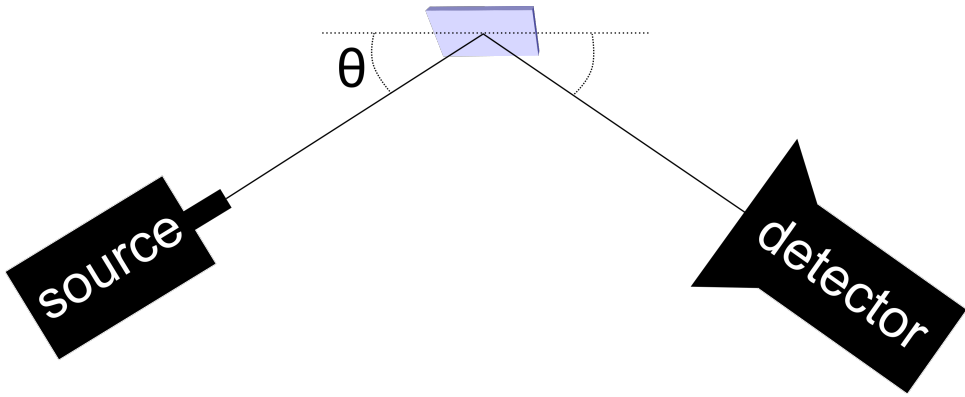


Figure 3.3: **XRD Overview.** In an XRD setup, an X-ray source is directed at the sample at a variable angle θ . The response at the detector as a function of θ is used to determine the crystal structure.

properties that reduce the number of these interactions is an interesting possibility.

3.4 Probing Materials

The rest of this chapter focuses on a brief overview of imaging tools that probe properties of materials and interfaces, though it isn't close to exhaustive. The main goal is to familiarize non-materials scientists interested in making high T_1 qubits with methods to verify and iterate their fabrication procedure.

3.4.1 X-ray Diffraction (XRD)

X-ray diffraction (XRD) is a technique used to determine the shape of a material's underlying crystal structure. This can be helpful in determining the phase of the superconductor (which can affect T_c) and finding the orientation of the superconductor and substrate for lattice-matching considerations. One major benefit of XRD is its speed. A single measurement involves little preparation and can be taken in a matter of hours.

Conceptually, an X-ray with wavelength λ on the order of nanometers is directed at a variable angle θ towards the film in question (figure 3.3). As the angle is swept, when Bragg's law is met there will be a peak at the detector:

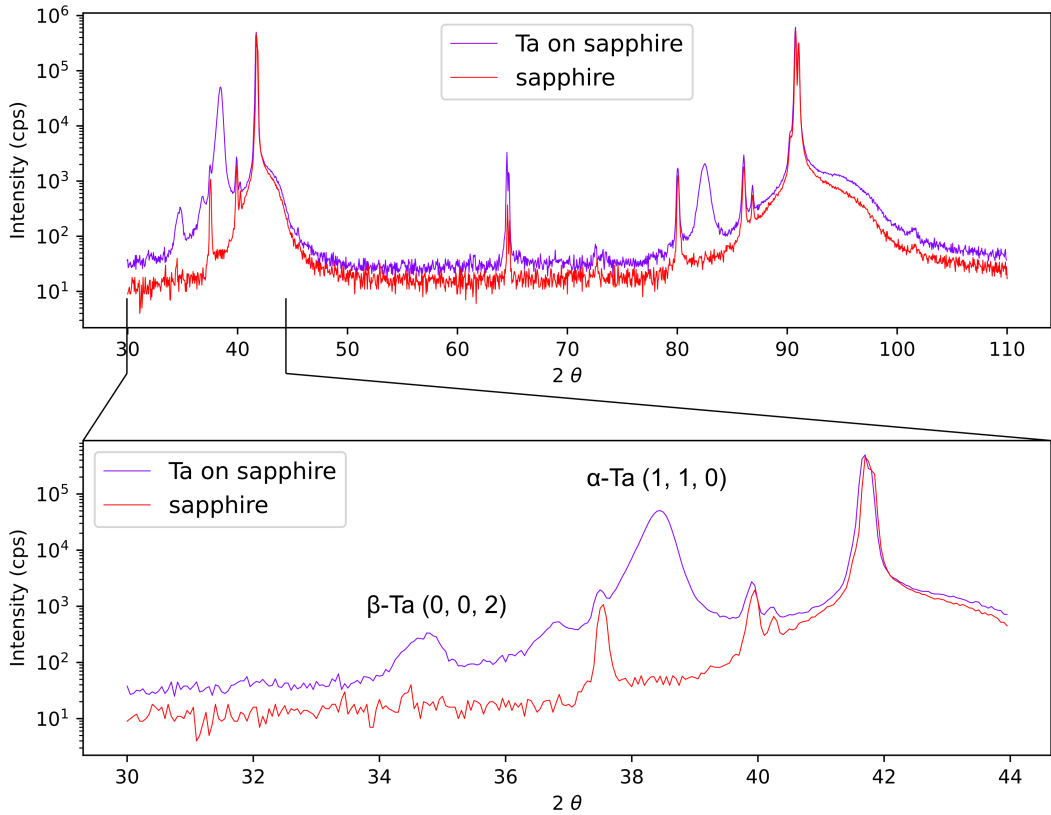


Figure 3.4: XRD Measurement of Tantalum and Sapphire. Example XRD measurement of a roughly 200nm thick tantalum film on top of sapphire, as well as sapphire alone.

$$n\lambda = 2ds\sin(\theta) \quad (3.1)$$

where d is the spacing between the crystal planes and n is an integer. The angles at which the signal is maximized correspond to distances between lattice planes, allowing the crystal structure to be determined.

An example XRD measurement of tantalum is shown in figure 3.4. When developing a tantalum deposition recipe, the XRD can be used to quickly detect the presence of β -tantalum by finding the height of the labeled peak [55].

3.4.2 XPS

X-ray photoelectron spectroscopy (XPS) is used to probe the surface of a material (on the order of 10nm deep). The method can provide significant amounts of information about

the metal-air and substrate-air interfaces, including chemical composition and thickness of the oxide layer. Surface residues can also be characterized. XPS has the benefit of being a very quick-feedback tool, with measurements taking on the order of one hour.

An XPS directs X-rays with energy $h\nu$ towards the surface in question. Through the photoelectric effect the X-rays are absorbed and electrons are emitted. The kinetic energy of the emitted electrons is measured and used to find the binding energy:

$$\text{Binding Energy} = h\nu - \text{Kinetic Energy} - \Phi_{spec} \quad (3.2)$$

where Φ_{spec} is the work function of the spectrometer [56]. Further, the relative intensity of the signal corresponding to different binding energies can be used to find how prevalent a material is in the surface layer.

Helpful XPS measurements include optimizing cleaning procedures to reduce residual carbon, measured by the carbon peak shown in figure 4.1. Further XPS can be used to quantify oxide thickness—for example the height of the tantalum oxide peak and the metal peak can be compared as surface processing steps are modified (figure 5.6).

3.4.3 AFM

Atomic force microscopy (AFM) is used to measure a height map of surfaces with sub-nanometer resolution. AFM can give surface morphology, detect the presence of fabrication imperfections, and measure the profile of etched edges of films.

Atomic force microscopy works by rastering a cantilever over a surface and detecting the response of the cantilever. Images of sapphire surface morphology and contamination can be found in figure 4.1.

3.4.4 PPMS

Physical property measurement systems (PPMS) measure electrical properties as a function of both temperature and magnetic field. This is useful to determine a film's T_c and likewise feedback on the quality of a deposition recipe. Furthermore, changing the

field can delineate unwanted phases and materials in a film by unequally changing the resistance vs. temperature curves as a function of field (figure B.2).

3.4.5 SEM and TEM

Scanning electron microscopy (SEM) is a tool that allows for the characterization of the sub-micron to millimeter scale morphology of a film. It is particularly useful for identifying fabrication problems. Due to its common use it won't be elaborated on here.

Similar to SEM, transmission electron microscopy (TEM) sends a beam of electrons at a sample. The electrons travel through the sample, which has been thinned to $\lesssim 200\text{nm}$ thickness, to a detector on the opposite side of the beam source. This can allow for nearly atomic-level resolution (see figure 4.10). In addition, diffraction patterns can be generated to determine sample orientation and elemental mapping techniques including energy-dispersive X-ray spectroscopy can be used to provide compositional analysis.

TEM applied to qubits can determine the grain size and composition of metal films (figures 4.10, 4.13). It can also directly probe the thickness of interfaces (figure 4.12). The downside of TEM is the process is time consuming.

Chapter 4

Tantalum Transmons

In this chapter we show that engineering the materials in qubits can significantly impact coherence times. We correlate spectroscopic and time domain measurements of tantalum transmons. In order to cleanly measure the properties of tantalum devices a large portion of the chapter is focused on optimizing fabrication recipes to reduce non-tantalum related losses. This chapter is a modification of [57].

4.1 Introduction

Steady progress in improving gate fidelities for superconducting qubits over the last two decades has enabled key demonstrations of quantum algorithms [58–60], quantum error correction [61–63], and quantum supremacy [64]. These demonstrations have relied on either improving coherence through microwave engineering to avoid losses associated with surfaces and interfaces [20, 53, 65] and to minimize the effects of thermal noise and quasiparticles [36, 50, 66, 67], or by realizing fast gates using tunable coupling [68, 69]. By contrast, little progress has been made in addressing the microscopic source of loss and noise in the constituent materials. Specifically, the lifetime (T_1) of the two-dimensional (2D) transmon qubit has not reliably improved beyond 100 μs since 2012 [17, 70], and to date the longest published T_1 is 114 μs [19], consistent with other recent literature reports [71–73].

The lifetimes of current 2D transmons are believed to be limited by microwave di-

electric losses [23, 74, 75]. However, the expected loss tangent of the bulk constituent materials should allow for significantly longer lifetimes. For example, if the only source of loss is high-purity bulk sapphire with loss tangent less than 10^{-9} [76, 77], T_1 would exceed 30 ms. Although it is notoriously difficult to pinpoint microscopic loss mechanisms, this suggests that losses are dominated by uncontrolled defects at surfaces and interfaces, by material contaminants, or by quasiparticles trapped at the surface [51]. Here we demonstrate that a significant improvement over the state of the art in 2D transmon qubits can be achieved by using tantalum as the superconductor in the capacitor and microwave resonators, replacing the more commonly used niobium. We hypothesize that the complicated stoichiometry of oxides at the niobium surface can include non-insulating species [52, 78, 79] leads to additional microwave loss, and that the insulating oxide of tantalum [80, 81] reduces microwave loss in the device. We observe a time-averaged T_1 exceeding 0.3 ms in our best device and an average T_1 of 0.23 ms averaged across all devices, a significant improvement over the state of the art.

4.2 Fabrication

In the following section several fabrication recipes are presented. The devices processed with each procedure and the corresponding measurements are given in Table 4.1.

4.2.1 Sapphire Preparation

During recipe development we aggressively cleaned and etched some wafers before tantalum was deposited. After dicing the resist-covered sapphire wafers, stripping the resist, and sonicating in solvents we found surface contamination. In particular, AFM revealed an abundance of particulates (figure 4.1 (a)) which were removed by cleaning in piranha solution (figure 4.1 (b)). The etched and piranha cleaned surface was smooth (R_a of 80 pm) and did not show any signs of roughening (figure 4.1 (b)). Additionally, the carbon signal in XPS was attenuated by a factor of 5 after piranha cleaning, illustrating a reduction in carbon contamination (figure 4.1 (c)). XPS also revealed zinc contamination that

Device	Average T_1 (μs)	Max T_1 (μs)	Q (millions)	Average T_{2R} (μs)	Average T_{2E} (μs)	Average T_{2CPMG} (μs)	Purcell Filter	Al Coated Enclosure	Mylar Shielding	Piranha Clean	Sapphire Etch	Optimized Wet Etch	Enclosure Lid Removed	Thin Al Layer	Geometry
1a*	98 \pm 2 [†]	99	1.9	-	-	-									Double Pad
1b*	127 \pm 4 [†]	130	2.5	-	-	-									Double Pad
2a	150 \pm 2 [†]	151	4.2	-	-	-	x								Double Pad
2b	157 \pm 19	179	4.4	98 \pm 8	153 \pm 12	-	x	x	x						Double Pad
2c	147 \pm 15	181	4.1	-	-	-	x	x	x						Double Pad
2d*	171 \pm 26	223	4.8	-	-	-	x	x	x						Double Pad
3	146 \pm 2 [†]	151	3.6	-	-	-	x	x	x						Double Pad
4	200 \pm 11	219	5.3	40 \pm 4	44 \pm 7	-	x	x	x	x					Double Pad
5	146 \pm 9	169	4.4	47 \pm 5	76 \pm 7	-	x	x	x	x					Double Pad
6	58 \pm 2 [†]	58	1.8	-	-	-	x	x	x	x					Double Pad
7a	166 \pm 1 [†]	176	5.4	18 \pm 1 [†]	49 \pm 1 [†]	-	x	x	x	x					Double Pad
7b*	184 \pm 18	220	6.1	-	-	-	x	x	x	x					Double Pad
8	135 \pm 1 [†]	135	4.5	-	-	-	x	x	x	x					Double Pad
9	127 \pm 1 [†]	133	3.0	-	-	-	x	x	x	x	x				Double Pad
10	139 \pm 3 [†]	139	3.9	-	-	-	x	x	x	x	x				Double Pad
11a	212 \pm 11	255	5.2	41 \pm 1	53 \pm 4	-	x	x	x	x	x	x			Double Pad
11b	273 \pm 27	303	6.7	101 \pm 5	144 \pm 9	-	x	x	x	x	x	x	x		Double Pad
11c	257 \pm 19	301	6.2	68 \pm 6	87 \pm 9	281 \pm 20	x	x	x	x	x	x	x		Double Pad
12	253 \pm 11	290	6.0	53 \pm 2	71 \pm 2	-	x	x	x	x	x	x			Double Pad
13a	288 \pm 35	351	6.6	68 \pm 6 [†]	-	-	x	x	x	x	x	x			Single Pad
13b*	247 \pm 22 [†]	277	5.6	-	-	-	x	x	x	x	x	x			Single Pad
14*	154 \pm 9	175	4.0	-	18 \pm 1 [†]	-	x	x	x	x	x	x			Single Pad
15	194 \pm 13	215	4.6	-	123 \pm 7	-	x	x	x	x	x	x			Double Pad
16	247 \pm 14	283	5.5	-	62 \pm 2	122 \pm 4 [†]	x	x	x	x	x	x			Double Pad
17	205 \pm 8	217	5.0	58 \pm 1 [†]	78 \pm 4	93 \pm 6 [†]	x	x	x	x	x	x			Double Pad
18	303 \pm 32	362	7.1	105 \pm 3 [†]	201 \pm 28	377 \pm 111	x	x	x	x	x	x	x		Double Pad
Nb1*	23 \pm 1 [†]	23	0.4	-	42 \pm 1 [†]	-									Double Pad
Nb2	79 \pm 1 [†]	82	2.0	-	-	-	x	x	x						Double Pad
Si1	118 \pm 2 [†]	124	2.3	44 \pm 2 [†]	-	-	x	x	x						Double Pad

Table 4.1: Summary of Devices. Here we include measurements of devices with different designs, fabrication procedures, and packaging. Devices labeled “Nb” were made with niobium instead of tantalum (Nb1 was heated to 350°C then cooled for 20 minutes before deposition, Nb2 was deposited at approximately 500°C) and all other devices were made from tantalum. Device Si1 was composed of about 200 nm of tantalum deposited on high-resistivity silicon. Each individual device is labeled with its own number. Devices marked with an additional letter indicate different thermal cycles of the same device. Entries marked with a “†” had three or fewer repeated measurements, and the reported errors were calculated by propagating the fit uncertainties. Otherwise the errors were calculated by finding the standard deviation of multiple measurements. Devices labeled with a “*” were fit without constraining the line of best fit to be normalized and have the proper offset. The average $T_{2,CPMG}$ column denotes the time averaged dynamical decoupling decoherence time at an optimal gate number. The quality factor is calculated using $Q = \omega_q T_1$ where ω_q is the qubit frequency.

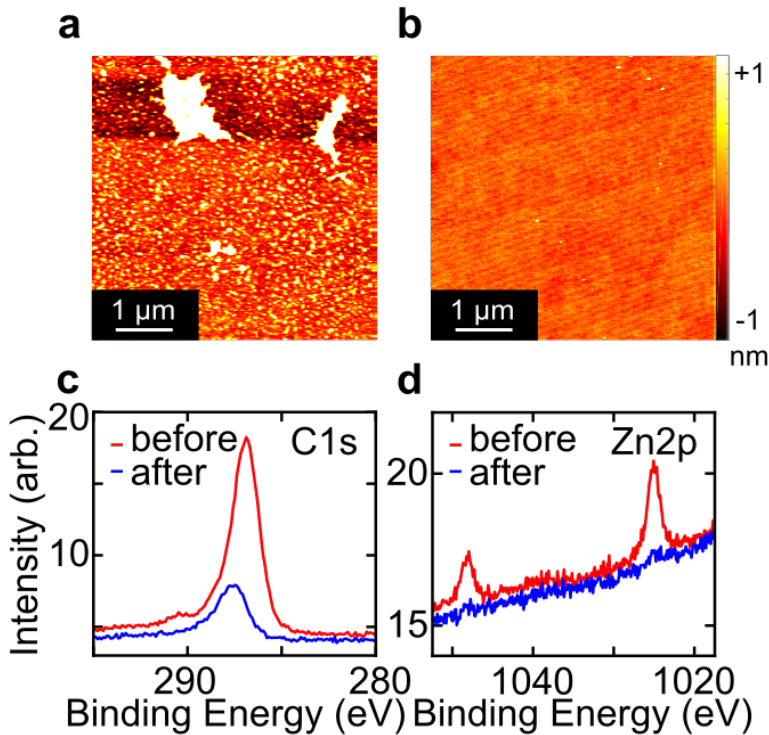


Figure 4.1: Characterization of Sapphire Surface. AFM images of sapphire after dicing, stripping resist, and solvent cleaning ((a)) and after subsequent piranha cleaning and etching ((b)), showing the removal of particulates from the surface. Average roughness values (R_a) are 400 and 80 pm for (a) and (b), respectively. XPS of sapphire identifies carbon ((c)) and zinc ((d)) contaminants on the sapphire surface. After piranha cleaning and etching, carbon is reduced by around a factor of five, and zinc is no longer detected. “Before” corresponds to the surface after dicing and solvent cleaning but before acid procedures, and “after” is following acid cleaning steps.

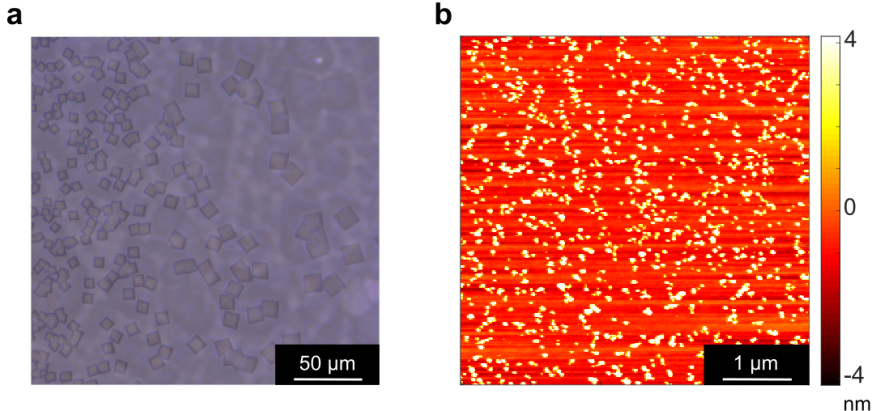


Figure 4.2: Sapphire Processing Pitfalls. (a), Optical microscope image of crystals on sapphire after etching in refluxing sulfuric acid for 30 min. (b), AFM image of sapphire surface showing particulate contaminants after etching and piranha cleaning in borosilicate glassware.

persisted through a piranha clean, but was removed by etching the sapphire substrate in heated sulfuric acid (figure 4.1 (d)). We note that sapphire wafers that had not been diced, stripped of resist, and sonicated in solvents displayed few particulates in AFM, and XPS showed a minimal carbon signal and no detectable zinc signal.

We prepare the sapphire surface using this sulfuric acid etch in Devices 9-14 and 17. In these devices, the wafers are covered with a protective layer of photoresist and then diced into 1 inch squares. After removing resist, the squares are TAMI cleaned and piranha cleaned. Next, the sapphire is placed into a quartz beaker filled with H_2SO_4 sitting on a room temperature hotplate. The hotplate is set to 150°C for 20 minutes, followed by a 10 minute cooldown period before removing the device. We estimate less than 1 nm of the surface is removed through this procedure [82]. To avoid residue from the etch, the device is piranha cleaned again. The device is then packaged, shipped, and loaded into a sputterer without further cleaning.

Calibrating the time and temperature of the sapphire etch is critical to maintaining a smooth surface morphology while still removing zinc. In particular, polycrystalline aluminum sulfates form on the sapphire surface after heating in sulfuric acid for too long and at too high of a temperature (figure 4.2 (a)) [82]. We developed our sapphire etch recipe by (1) looking for crystal formation in an optical microscope, (2) ensuring that zinc was removed in XPS, and (3) checking that we preserved smooth surface morphology in AFM. We note that the zinc appeared to be inhomogeneously distributed on the surface and so we routinely checked multiple spots in XPS. After adjusting the time and temperature to the optimum procedure outlined above, we did not detect any crystal formation.

Additionally, we observed surface contamination with AFM from etching sapphire in borosilicate glassware. An example of surface particulate contamination is shown in figure 4.2 (b). Switching to a quartz beaker solved this issue.

We note that Devices 16 and 18 were not processed using the sapphire etch, and they exhibited T_1 over 0.2 ms. In the future we are interested in studying the impact of sapphire material properties on device performance. We plan to fabricate devices on higher-purity sapphire, remove polishing-induced strain by etching more of the substrate, and anneal to form an atomically smooth surface [82].

4.2.2 Deposition and Lithography

The 2D transmon qubits are fabricated on c-plane sapphire substrates (Crystec GmbH) that are 0.53 mm thick and double-side polished (figure 4.3). Prior to deposition, the wafer is cleaned either by the method given in section 4.2.1 or by the commercial deposition company, Star Cryoelectronics, by dipping in a piranha solution (H_2SO_4 and H_2O_2) then cleaning with an oxygen plasma (Technics PE-IIA System) immediately before loading into the sputterer.

Tantalum is deposited on the sapphire substrate at high temperature (Star Cryoelectronics, alpha tantalum, 500°C deposition, 200 nm thickness, no seed layer, sapphire preclean with piranha and oxygen plasma). Before photolithography, the tantalum-coated

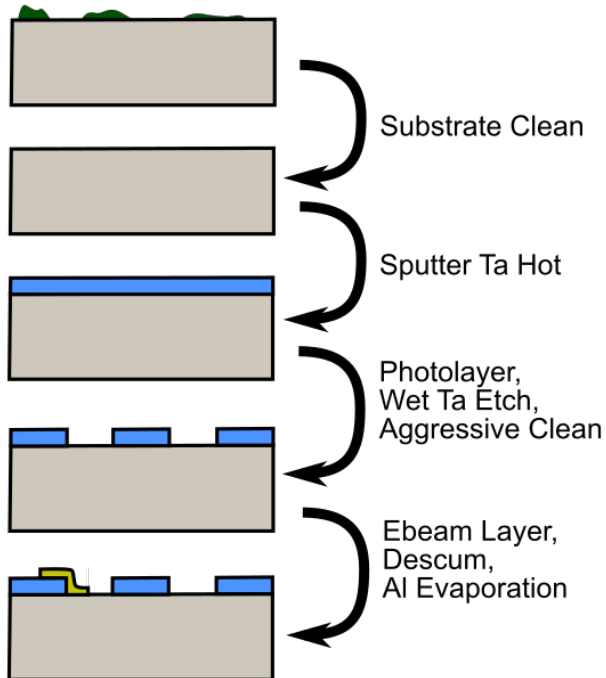


Figure 4.3: Qubit Fabrication Process. The sapphire substrate (gray) is initially contaminated with carbon (green) which is reduced through substrate cleaning. Tantalum (blue) is then deposited and subsequently patterned with a wet etch. Finally, the Josephson junctions (yellow) are lithographically defined and deposited.

substrates are placed in a 2:1 mixture of H_2SO_4 and H_2O_2 for 20 minutes (hereafter in this chapter “piranha-cleaned” refers to this specific chemical ratio and time duration) then heated on a hotplate for 5 minutes at 140°C before AZ 1518 resist is spun (Merck KGaA). The resist is patterned using a direct-write process (2 mm write head on a Heidelberg DWL 66+ Laser Writer). After developing (85 sec in AZ 300MIF developer from Merck KGaA), the resist is hard-baked for 2 min at 115°C . Unwanted residual resist is removed using a gentle oxygen descum (2 min in 30 mTorr O_2 with 20 W/200 W RF/ICP coil power in a Plasma-Therm Apex SLR). Next, the tantalum is etched in a 1:1:1 ratio of HF:HNO₃:H₂O (Tantalum Etchant 111 from Transene Company, Inc.) for 21 sec. After stripping resist, the device is solvent-cleaned by sonicating in sequential baths of toluene, acetone, methanol, and isopropyl alcohol for approximately 2 minutes each (“TAMI-cleaned”) then piranha-cleaned. The patterned tantalum is prepared for electron beam lithography to define Josephson junctions (resists MMA 8.5 MAA and 950 PMMA, with a 40 nm layer of evaporated aluminum to dissipate charge), then the chips

are diced into 7x7 mm squares.

Liftoff patterns for Manhattan junctions [83] with overlap areas of approximately $0.03 \mu\text{m}^2$ are then exposed (Elionix ELS-F125). The anticharge layer is removed through a 4 min bath in MF 319 (Rohm and Haas Electronic Materials LLC) followed by a 50 sec bath in a 1:3 mixture of methyl isobutyl ketone to isopropyl alcohol. Next, the device is loaded into a Plassys MEB 550S electron beam evaporator and ion-milled (400 V, 30 sec along each trench of the junction). Immediately after, 15 nm of aluminum is deposited at 0.4 nm/sec at a pressure of approximately 10^{-7} mBar, followed by a 15 min, 200 mBar oxidation period. Finally, 54 nm of aluminum is deposited to form the second layer of the junction, with the same evaporation parameters (for Device 18, 15 nm and 19 nm of aluminum are deposited, respectively). The resist is then removed by soaking the sample in Remover PG (Kayaku Advanced Materials, Inc.) for approximately 3 hours at 80°C, briefly sonicating in hot Remover PG, then swirling in isopropyl alcohol.

4.2.3 Device Packaging

The completed devices are first mounted to a printed circuit board (PCB). The edge of the tantalum ground plane is firmly pressed against the PCB's copper backside, sandwiched between the PCB and a piece of aluminum-coated oxygen-free copper (figure 4.4 (b)). The device is then wirebonded (figure 4.4 (a), (d)). An aluminum-coated oxygen-free copper lid is sometimes placed above the qubit (table 4.1 column “Enclosure Lid Removed”), forming a superconducting enclosure partially surrounding the qubit. The device is mounted in a dilution refrigerator with a base temperature of approximately 9-20 mK. The qubit and PCB are wrapped in several layers of aluminized mylar sheeting and suspended by an oxygen-free copper rod in the middle of an aluminum cylinder coated with microwave-attenuating epoxy or sheeting (Laird Performance Materials Ec-cosorb Cr or Loctite Styccast). This cylinder is enclosed in a mu-metal can to reduce the penetration of ambient magnetic fields into the aluminum during the superconducting transition. Both cans are then wrapped in several layers of mylar sheeting.

We note that all of the double-pad transmons presented in this text are positioned

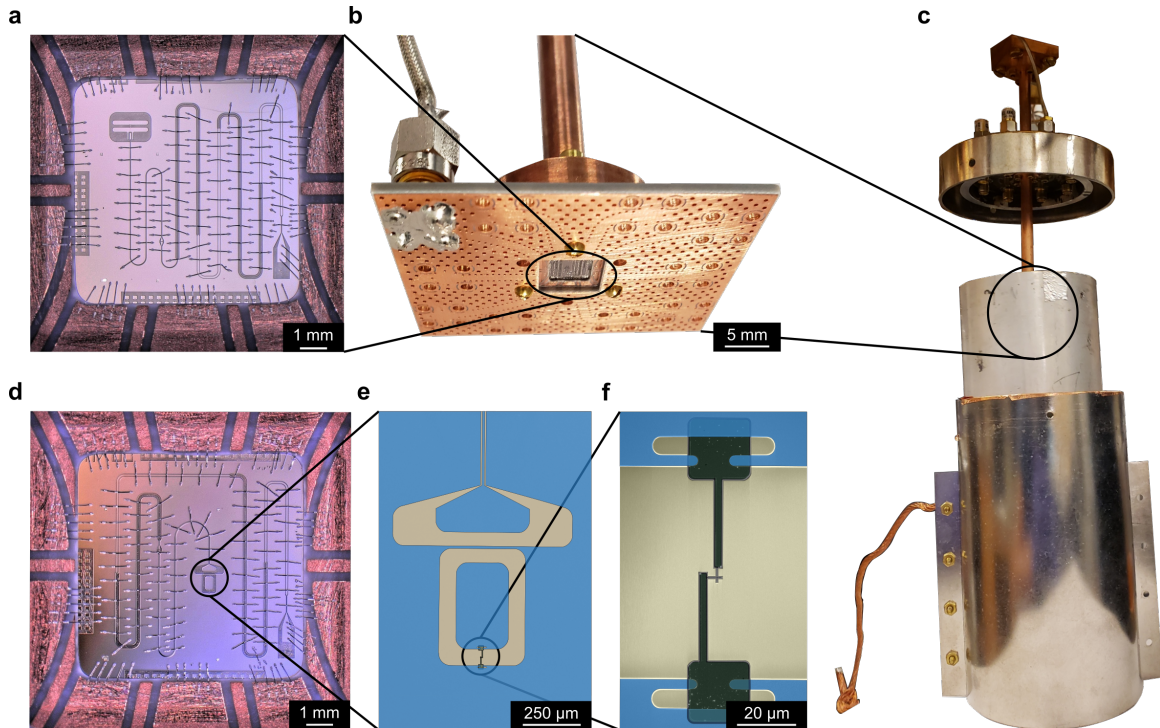


Figure 4.4: Device Geometry Overview. (a), Double-pad and ((d)) single-pad geometry transmons mounted to a PCB. In both cases the copper traces of the PCB are visible around the outside of the images, along with the wirebonds providing electrical connections. The excitation and measurement pulses first enter the curving Purcell filter, go through a capacitive coupler to the resonator, then to the qubit. We note in ((d)) that we moved the qubit to the center of the chip. (b), Device sandwiched between a PCB and aluminum-coated copper which is thermally anchored to the dilution refrigerator. (c), Exploded view of aluminum (inner) and mu-metal (outer) shields. (e), Close-up, false-colored SEM image of the single-pad qubit and coupler as well as ((f)) the Josephson junction. The leads from the capacitor pads to the Josephson junction are approximately $2 \mu\text{m}$ wide.

approximately 2 mm away from the copper traces on the PCB (figure 4.4 (a)), which could result in loss due to parasitic coupling of the qubit to the resistive traces. In order to reduce this possible source of loss, devices fabricated with the single-pad geometry were moved close to the center of the sapphire chip (figure 4.4 (d)).

4.2.4 Design and Fabrication Notes

Note: Tantalum Etching

Initially we etched tantalum using a reactive-ion etch (8:3:2 CHF₃:SF₆:Ar chemistry at 50 mTorr, RF/ICP power of 100 W/100 W). We then switched to a wet etch composed of 1:1:1 HF:HNO₃:H₂O. Comparing Devices 4-10 with Devices 11-18 in table 4.1, we note the optimized wet etch likely improved T_1 . Further details can be found in appendix C.

Note: Device Geometry

We measured two different types of transmons: devices with double-pad capacitors, where neither pad has a direct ground connection (figure 4.5 (a)), and single-pad devices [84], where the ground plane serves as one side of the transmon's capacitor (figure 4.4 (d)). Two different geometries of double-pad devices were tested on sapphire: Devices 1-6 had a 60 μ m gap between capacitor pads, while Devices 7-12 and 15-18 had a 70 μ m gap and a smaller charging energy.

Cavity and Purcell Filter

The coupling capacitor design between the resonator and Purcell filter was consistent across all devices on sapphire. The cavity linewidth of Device 18 was 380 ± 2 kHz.

To limit Purcell decay we capacitively couple the readout resonator to a stepped impedance filter [46]. The filter is composed of two repetitions of two alternating sections with impedances of 26 Ω and 127 Ω with lengths 5.5 mm and 8 mm, respectively.

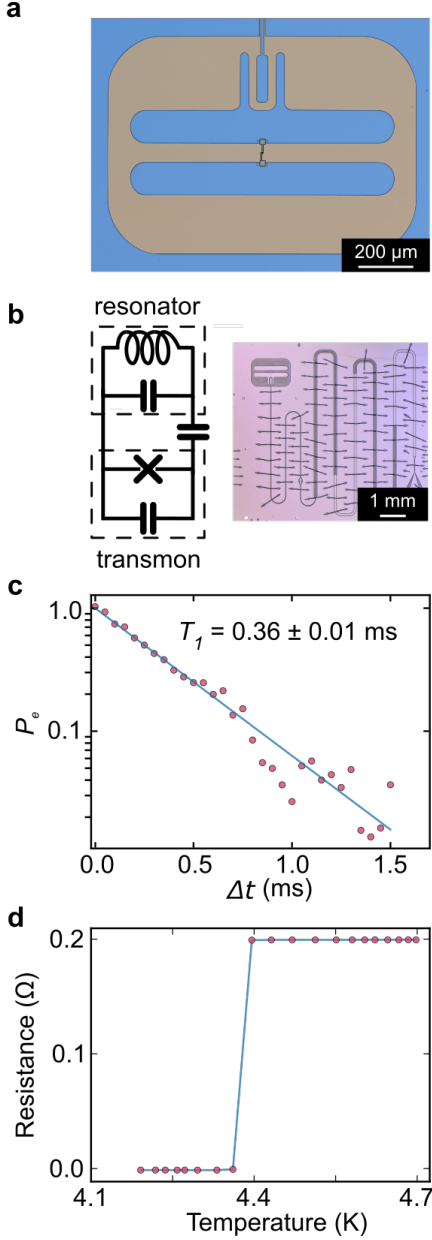


Figure 4.5: **Tantalum-Based Transmon Superconducting Qubit.** (a), False-colored optical microscope image of a transmon qubit. The transmon consists of a Josephson junction shunted by two large capacitor islands made of tantalum (blue) on sapphire (gray). (b), Device layout image and corresponding circuit diagram of the transmon qubit coupled to the resonator via a coupling capacitor. (c), T_1 measurement of Device 18, showing the excited state population P_e as a function of delay time Δt . Line represents a single exponential fit with a characteristic T_1 time of $0.36 \pm 0.01 \text{ ms}$. (d), Four-probe resistance measurement of the tantalum film showing $T_c = 4.38 \pm 0.02 \text{ K}$, consistent with the critical temperature of α -tantalum.

Participation Ratio

To isolate geometric contributions to relaxation we simulated the participation ratios of the $70\ \mu\text{m}$ gap double-pad geometry using a method similar to Wang et al. [23], assuming the same simplified junction geometry. A device with a dielectric layer of thickness 3 nm and dielectric constant $\epsilon = 10$, similar to the aluminum oxide layer simulated in [23], gave a substrate-metal interface participation ratio of $1.6 * 10^{-4}$, excluding the areas within $1\ \mu\text{m}$ of the junction.

4.3 Measurement

Each transmon is capacitively coupled to a microwave resonator, allowing the state of the qubit to be measured dispersively [85]. The transmon frequencies range from 3.1 - 5.5 GHz while the resonators range in frequency from 6.8 - 7.3 GHz. An overview of the setup used to measure a majority of the devices is given in figure 4.6. An Agilent E8267D vector signal generator, Holzworth HS9004A RF synthesizer, and Keysight M9330A Arbitrary Waveform Generator are used to synthesize the excitation and measurement pulses. The input signals are combined into a single line and then attenuated on each plate of the dilution refrigerator. An additional filter made of Eccosorb CR110 epoxy is placed in the aluminum can to attenuate high-frequency radiation. Measured in reflection, the output signal is sent through a circulator (Raditek RADC-4-8-cryo-0.01-4K-S23-1WR-ss-Cu-b), two isolators (Quinstar QCI -075900XM00), superconducting wires, and then a high-electron-mobility transistor amplifier (Low Noise Factory LNF-LNC4_8C) at 4 K. After the signal is amplified at room temperature (through two MITEQ AFS4-00101200 18-10P-4 amplifiers), it is measured in a homodyne setup by first mixing it with a local oscillator (Holzworth HS9004A), further amplifying (Stanford Research Systems SR445a), and then digitizing (Acqiris U1084A).

To determine T_1 , we excite the qubit with a π -pulse and measure its decay over time at a temperature between 9 and 20 mK. In our best device, our highest T_1 measurement is 0.36 ± 0.01 ms (figure 4.5 (c)). We verify that the deposited tantalum film is in the

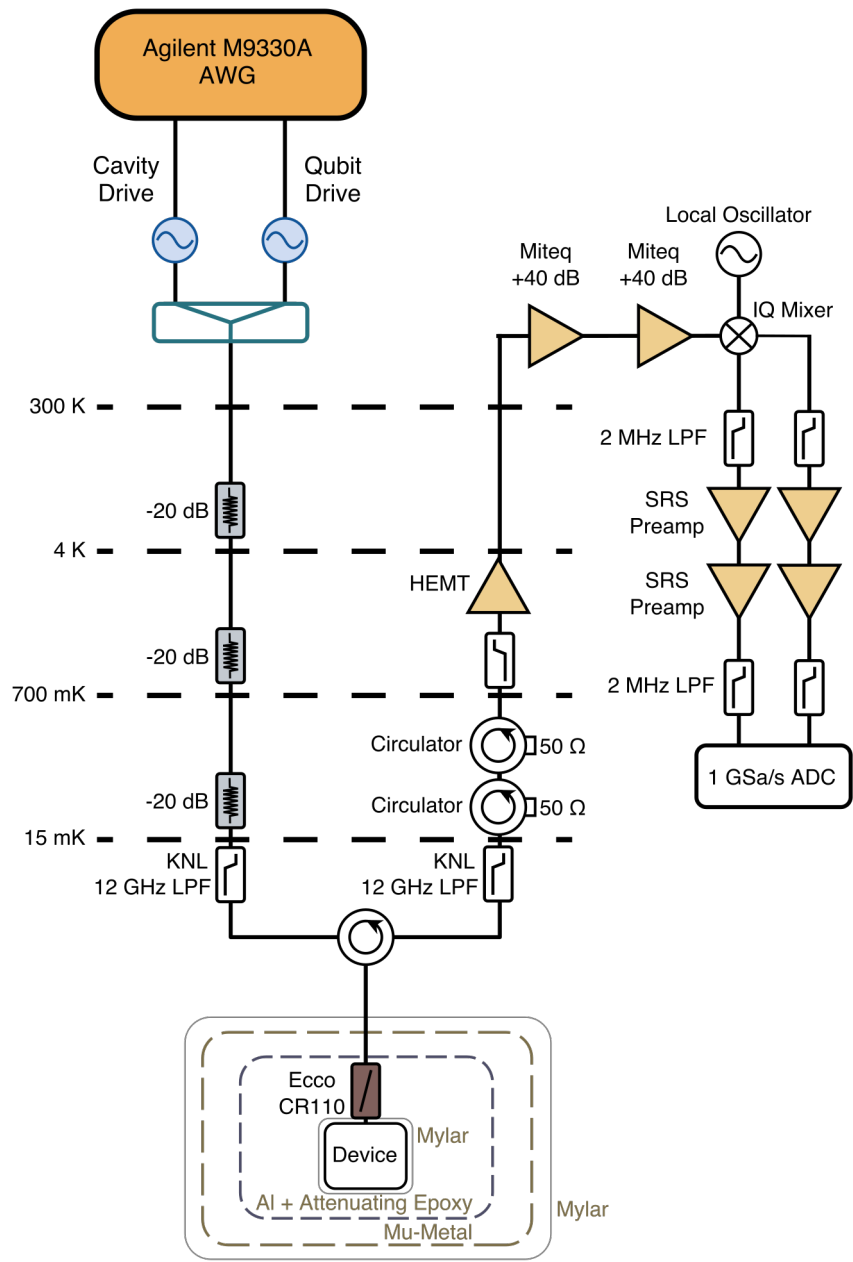


Figure 4.6: Schematic of the Measurement Electronics and Device Shielding.

α phase by measuring resistance as a function of temperature. The observed superconducting critical temperature (T_c) is around 4.3 K, which is consistent with the intended phase (figure 4.5 (d)) rather than the tetragonal β phase which has a T_c below 1K [86, 87].

We observe reproducible, robust enhancement of T_1 across all devices fabricated with this process. The lifetime of a given qubit fluctuates over time, with a standard deviation of around 7% of the mean (figure 4.7 (a)). Results for eight devices are presented in figure 4.7 (b), with the time-averaged T_1 ranging from 0.15 ms to 0.30 ms, and an average T_1 of 0.23 ms across all devices, qualitatively exceeding the T_1 of prior 2D transmon devices. We note that the highest observed T_1 and T_2 is achieved in a device with a thinner aluminum layer (Device 18, see Methods). The time-averaged coherence time, $T_{2,Echo}$, in our best device is 0.20 ± 0.03 ms (a trace is shown in figure 4.7 (c)). We can extend the coherence time using a Carr-Purcell-Meiboom-Gill (CPMG) pulse sequence [88] (figure 4.7 (d)), and we achieve a time-averaged $T_{2,CPMG}$ of 0.38 ± 0.11 ms in our best device (figure 4.7 (a)). The spectral noise density extracted from dynamical decoupling measurements is consistent with $1/f$ noise (figure 4.8) suggesting this noise can be mitigated with a Floquet drive [89]. We note that there are small variations in processing and packaging between these eight devices which are outlined in Methods and table 4.1.

4.3.1 CPMG

To reduce our devices' low-frequency noise sensitivity we applied a sequence of π -pulses [88]. Each pulse had a Gaussian envelope with σ around 20-50 ns and was truncated at $\pm 2\sigma$. Due to the large number of sequential pulses, we found that reducing gate error through frequent calibration was important.

To derive the qubit's noise spectral density (figure 4.8) from such a pulse sequence, we follow the procedure in [88]. The signal-to-noise ratio decreases as the overall delay time between initial excitation and measurement increases. For clarity, we include only delays spanning up to approximately T_1 . For simplicity we assume the gates are instantaneous. We find a noise power spectral density that is well fit by $A/f^\alpha + B$ with $\alpha = 0.7$.

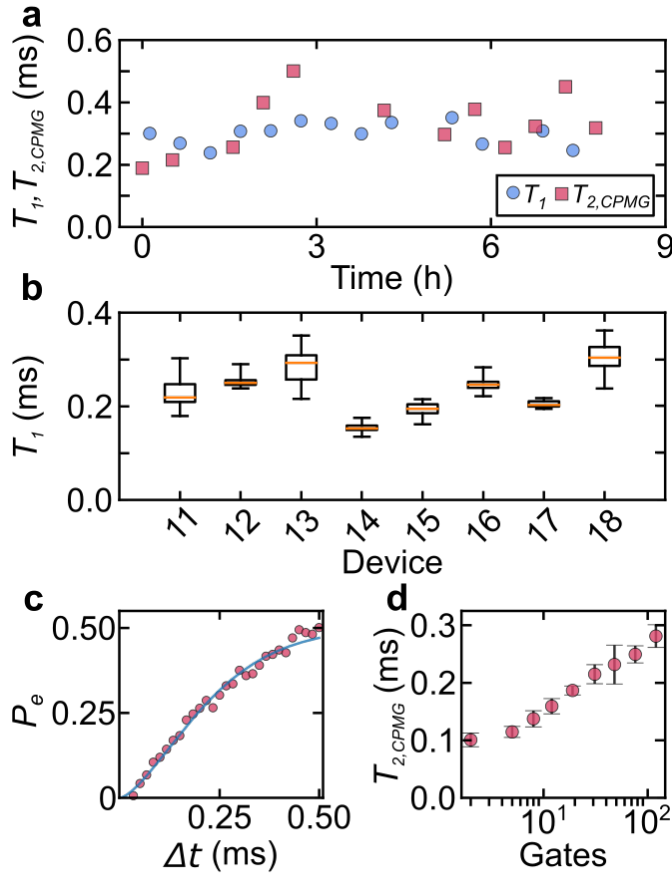


Figure 4.7: Lifetime and Decoherence Measurements. (a), Lifetime (T_1) and coherence time with dynamical decoupling ($T_{2,CPMG}$) of Device 18 over time. (b), Summary of T_1 time series measurements of all devices fabricated with a wet etch and piranha cleaning steps. Details about the specific processing steps for each device are given in table 4.1 and the Methods. The yellow line shows the median, while the box spans the middle two quartiles of the data. The whiskers show the extremal measurements. Data for devices 13, 14, and 17 are the average of 19, 14, and 7 individual T_1 measurements, respectively, while the rest are the average of at least 32 measurements. Each device was measured over a period of hours to days, and devices 11 and 13 include data from multiple dilution refrigerator cycles. (c), $T_{2,Echo}$ measurement of Device 18, showing the excited state population P_e as a function of delay time Δt . Solid blue line shows a stretched exponential fit to the data. The fit gives $T_{2,Echo} = 249 \pm 4 \mu\text{s}$. (d), $T_{2,CPMG}$ of Device 11 as a function of the number of gates in a CPMG pulse sequence. The error bars denote one standard deviation in the data.

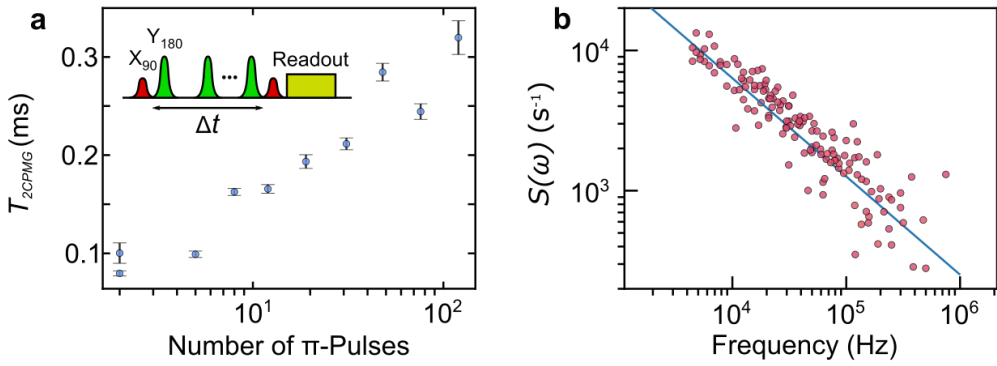


Figure 4.8: **Spectral Decomposition for Device 11c.** (a), $T_{2,CPMG}$ as an increasing number of pulses reduce the qubit's sensitivity to low-frequency noise. At each point we apply the pulse sequence shown in the inset with a fixed number of π -pulses and vary the delay, Δt , with values ranging from $16 \mu\text{s}$ to 2 ms . Error bars give the standard deviation in the $T_{2,CPMG}$ fit parameter. Inset: Measurement pulse sequence. X and Y identifies the axis of rotation. Subscripts 90 and 180 refer to a $\pi/2$ and π pulse, respectively. (b), Noise power spectral density $S(\omega)$ of the same data as ((a)), following [88]. The blue dashed line indicates a fit by eye to $A/f^\alpha + B$ where $\alpha = 0.7$, $A = 2\text{e}6\text{s}^{-1}$, and $B = 3\text{e}2\text{s}^{-1}$.

4.3.2 Fitting Procedure

We fit our transmon T_1 data to $f(\Delta t) = e^{-\Delta t/T_1}$, where T_1 is a fit parameter and the function represents the population in the excited state. We fit any T_2 data taken with fringes to the fit $f(\Delta t) = 0.5e^{-\Delta t/T_{2R}} \cos(2\pi\Delta t\delta + \phi_0) + 0.5$ where T_{2R} , δ , and ϕ_0 are fit parameters. For echo and CPMG experiments, we fit our T_2 data with a stretched exponential, $f(\Delta t) = 0.5e^{-(\Delta t/T_2)^n} + 0.5$, where T_2 and n are fit parameters. If $n < 1$, the data is refit to a pure exponential. Figure 4.9 shows a representative decay for a low, average, and high value of $T_{2,CPMG}$ for the data shown in figure 4.7 (a). In time sequences, data traces with obvious abnormalities or poor fits as measured by root-mean-square error are discarded.

4.4 Device iterations

Table 4.1 summarizes different iterations of the fabrication procedure. Initially we made a tantalum transmon using our standard niobium processing techniques (reactive ion

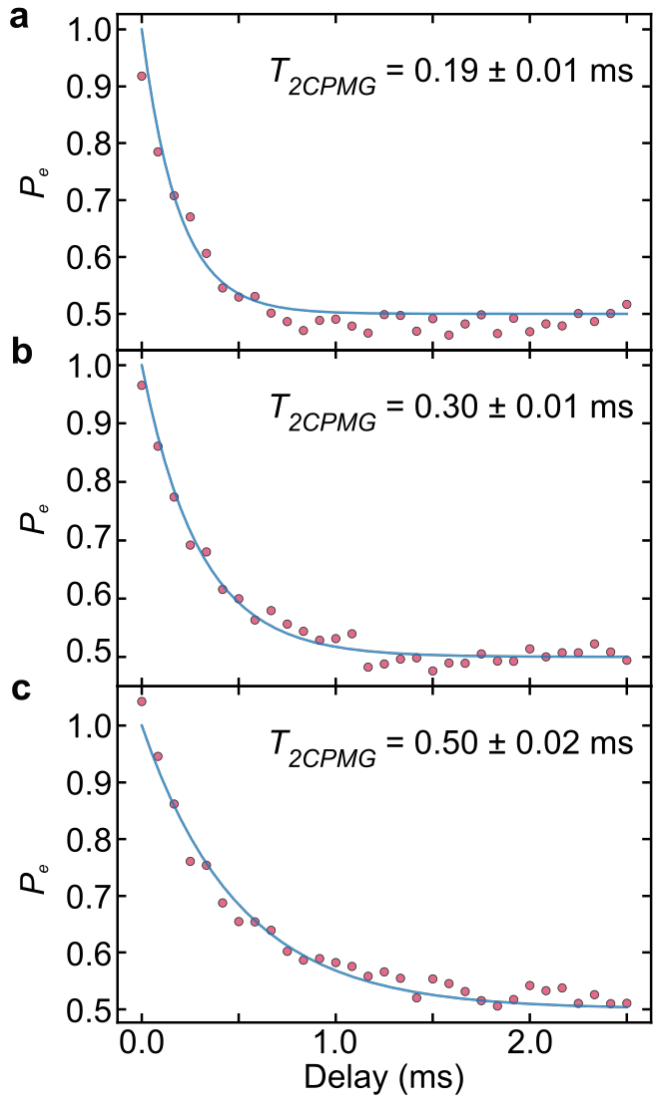


Figure 4.9: **CPMG Traces.** Low ((a)), middle ((b)), and high ((c)) $T_{2,CPMG}$ traces from the data in figure 4.7 (a), showing the excited state population P_e as a function of delay time. All three traces were fit to a stretched exponential with the exponent constrained to be larger than one.

etching, no acid cleaning). This material switch alone improved the coherence time by more than a factor of four compared to the control sample (table 4.1, Devices 1a and Nb1). We then began to iterate our packaging and fabrication techniques to explore the new dominant loss mechanisms.

First we minimized losses unrelated to the qubit materials and interfaces. We reduced the density of photonic states at the qubit frequency by means of a Purcell filter (Device 2a and all subsequent devices) [90]. We also deposited aluminum shielding on a majority of the copper enclosure immediately surrounding the device to reduce dissipative currents induced by the qubit in the surrounding metal. At the same time, we introduced a mylar sheet wrapped around the PCB as an extra layer of shielding. Both added layers give additional protection from high-energy radiation (Device 2b and all subsequent devices). To check if the improvements in T_1 were from these environmental changes or from the heating of the substrate during deposition, a

To study the impact of these packaging improvements as well as the effect of heating the substrate during deposition, we made a device from niobium sputtered at 500°C (Device Nb2). This resulted in a T_1 of $79 \pm 1 \mu\text{s}$, an improvement over our previous niobium devices, but qualitatively lower than tantalum-based devices. This indicates that thermal cleaning of the substrate, Purcell filtering, and better packaging may play a role in enhancing T_1 , but does not completely explain our improved coherence.

Next we focused on reducing material contaminants. XPS measurements revealed significant carbon residue that persisted after solvent-based cleaning. Accordingly, we reduced carbon contamination by adding a piranha clean before spinning e-beam resist (Device 4 and all subsequent devices). Removal of particulates was verified using atomic force microscopy (AFM), and the signal due to adventitious carbon measured by x-ray photoelectron spectroscopy (XPS) is attenuated after cleaning (figure 4.1). As mentioned above, we also cleaned the sapphire substrate prior to tantalum deposition. For Devices 1-8, 15-16, and 18 as well as Nb1 and Nb2, the sapphire substrate was dipped in a piranha solution and cleaned with an oxygen plasma (Technics PE-IIA System) immediately before loading into the sputterer. For the rest of the sapphire devices, we cleaned the

substrate with the sapphire etch described above (Supplementary Note 2), packaged and shipped the samples, then deposited the tantalum.

We then focused on the tantalum etch, described in more detail in appendix C. Devices 1-6, Nb 1-2, and Si1 were all fabricated with reactive ion etching. Devices 7-10 were made using initial versions of the wet etch (using different resists, etch times, and acid concentrations), where the etch clearly roughened the sidewalls (figure C.1 (c)). Devices 11-18 were made using the optimized wet etch.

Of the ten devices measured prior to the optimized wet etch, none had a T_1 in excess of 200 μs ; of the eight patterned with the optimized wet etch and fabricated with our cleaning procedure, six had a T_1 greater than 200 μs . These observations imply that residue and poor edge and surface morphology may limit qubit lifetimes for our tantalum devices.

4.4.1 Transmon on a Silicon Substrate

We fabricated a 2D, double-pad, tantalum transmon on silicon (Device Si1) with a similar design to that used for the devices on sapphire. The primary elements that changed during the fabrication process were: (i) a different plasma etch time to avoid overetching into the silicon, (ii) no aluminum layer was deposited on top of the e-beam resist prior to e-beam lithography, and (iii) the e-beam intensity was adjusted during the lithography step. We found that reactive-ion etching severely roughened the silicon surface (17 nm RMS surface roughness, measured with a Keyence Optical Profilometer). We plan to optimize this fabrication process in the future.

4.5 Characterization of tantalum films.

4.5.1 Overview

Because thin film structure has been observed to affect qubit performance for niobium-based qubits [52], and because the crystal structure of thin tantalum films sensitively depends on deposition parameters [55, 86], we present detailed characterization of the

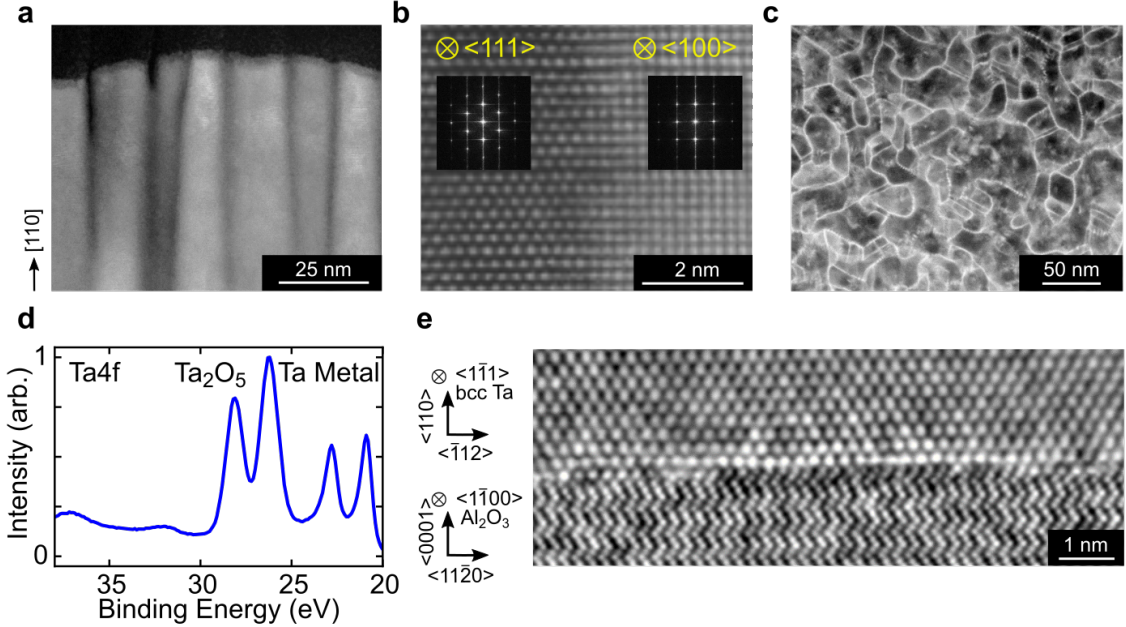


Figure 4.10: Microscopy and Spectroscopy of Tantalum Films. (a), STEM image of the tantalum film, showing single-crystal columns with the growth direction oriented along the $[110]$ axis. (b), Atomic resolution STEM image of an interface between two columns, viewed from $\langle 1\bar{1}1|1\bar{1}1 \rangle$ and $\langle 001|001 \rangle$ zone axes respectively. Fourier transforms (insets) of the image show that the columns are oriented with the image plane perpendicular to the $\langle 111|111 \rangle$ or $\langle 100|100 \rangle$ directions. (c), STEM image of a horizontal device cross section, showing grain boundaries. Image contrast at grain boundaries results from diffraction contrast caused by interfacial defects. (d), XPS spectrum of a device, exhibiting peaks from tantalum metal and Ta₂O₅. Other oxidation states of tantalum are expected to have binding energies between 22.2 and 23.8 eV [91, 92]. (e), High-resolution STEM with integrated differential phase contrast imaging of the interface between the sapphire and tantalum showing epitaxial growth.

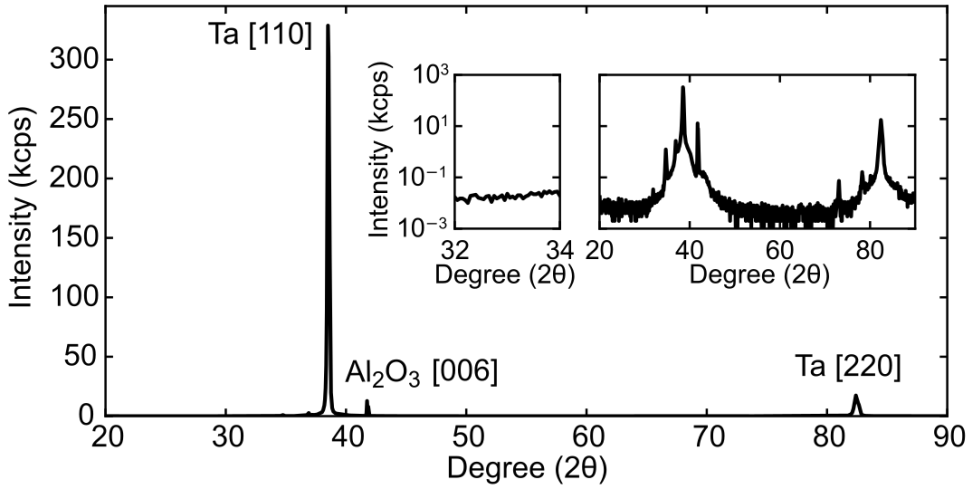


Figure 4.11: X-ray Diffraction Spectrum of a Sputtered Tantalum Film on Sapphire. XRD spectrum of sputtered tantalum on sapphire shows clear peaks corresponding to α -tantalum and sapphire. Inset left, small region of scan plotted on a log scale, showing that we do not detect a β -tantalum [002] peak at 33.7° (2θ) [55]. Inset right, entire scan range on a log scale, showing a few unassigned small peaks which could be caused by contamination, instrumental artifacts, or impurities or defects in the films.

deposited tantalum films. Scanning transmission electron microscopy (STEM) of a film cross section reveals a columnar structure, with the growth direction oriented along the [110] axis (figure 4.10 (a)) and these observations are corroborated by probing a larger area with x-ray diffraction measurements (figure 4.11). Atomic-resolution STEM confirms the BCC structure of the film and reveals that the individual columnar grains are single-crystal, with the front growth face perpendicular to either the $\langle 100|100 \rangle$ or $\langle 111|111 \rangle$ directions (figure 4.10 (b)). The different orientations result from the underlying three-fold symmetry of the sapphire crystal structure about its c-axis [93]. A top-down plane view cross-sectional STEM shows that the grains range in size from around 5 to 50 nm (figure 4.10 (c)). We study the tantalum oxide on our devices using XPS, which shows two sets of spin-orbit split doublet peaks with binding energy between 20 and 30 eV associated with $4f$ core ionization of Ta metal (lower binding energy) and Ta_2O_5 (higher binding energy) (figure 4.10 (d)) [91, 92]. The relative intensity of the metal and oxide peaks indicates that the oxide is approximately 2 nm thick (see Supplementary Information), consistent with angle-resolved XPS and high-resolution STEM measurements

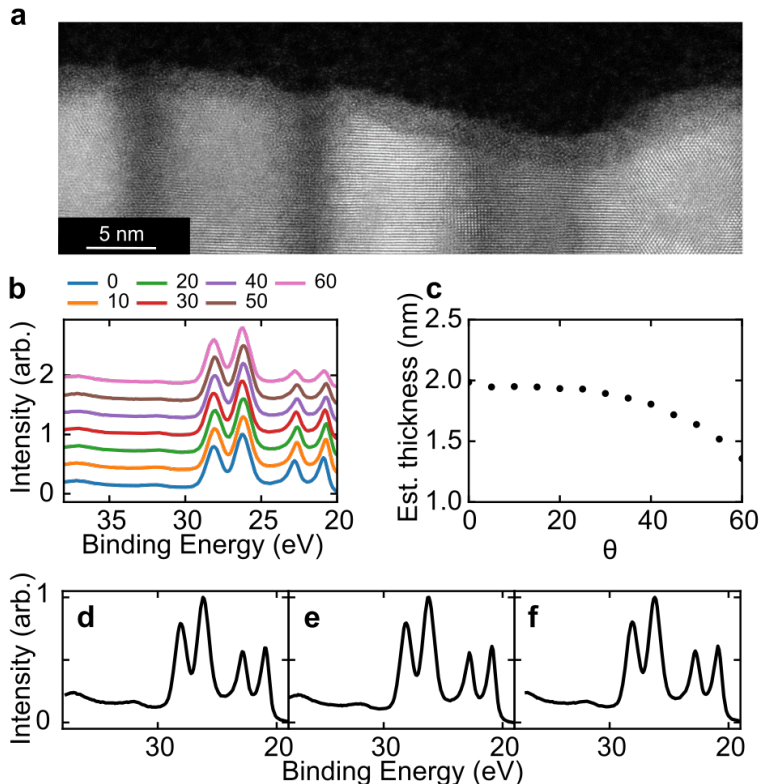


Figure 4.12: Oxide Characterization. (a), Atomic resolution STEM image showing an amorphous oxide layer about 2-3 nm thick on the tantalum surface. (b), Angle-resolved XPS measurements of Ta4f region of a fabricated device, offset vertically for clarity. Colors indicate the angle in degrees between sample and detector. (c), Estimated oxide thickness as a function of angle between sample and detector. (d-f), Ta4f normal incidence XPS data of three completed devices showing nearly identical spectra. The devices were from different tantalum depositions and underwent different fabrication steps. In addition to other variations in fabrication, the device in (d) was only solvent cleaned while the devices surveyed in (e) and (f) were piranha cleaned.

(figure 4.12). Lastly, we directly image the interface between the sapphire surface and the sputtered tantalum using integrated differential phase contrast imaging (iDPC) under STEM (figure 4.10 (e)). The interface shows an atomically sharp boundary with clear evidence of epitaxial growth, in which the tantalum atomic layer is directly grown on top of the oxygen atomic layer in the sapphire.

4.5.2 X-ray Diffraction

We use XRD to study the crystal structure of our films over a much larger area than is feasible with STEM images (figure 4.11). An acquired spectrum of a film exhibits a strong peak corresponding to α -tantalum [110] [55], corroborating STEM images that suggest that our films grow uniformly along that direction (figure 4.10 (a)). Additionally, we observe peaks corresponding to sapphire [006] [82] and α -tantalum [220] [55]. We do not detect a β -tantalum [002] peak at 33.7° (2θ) (figure 4.11, inset left) [55]. This provides further evidence along with our T_c and STEM measurements that the tantalum films are uniformly in the α phase. We note that there are a few unassigned small peaks which could result from contamination, instrumental artifacts, or impurities or defects in the tantalum films (figure 4.11, inset right).

4.5.3 Grain Boundaries

We further interrogate the grain boundaries visible in a plane-view image (figure 4.13 (a)) by using energy dispersive x-ray spectroscopy (EDS) to perform spatially-resolved elemental analysis. We find a uniform distribution of tantalum (figure 4.13 (b)) and oxygen (figure 4.13 (c)) over the region, and no oxygen enrichment at the grain boundaries. This suggests that our films do not grow oxide between the grains, and that the image contrast observed in figure 4.13 (a) arises instead from diffraction contrast caused by interfacial defects.

A high-resolution STEM image of a grain boundary elucidates the crystal structure at the boundaries (figure 4.13 (d)). Taking a diffraction pattern of a grain boundary region indicated by a green square in figure 4.13 (d) gives a pattern consistent with twinning

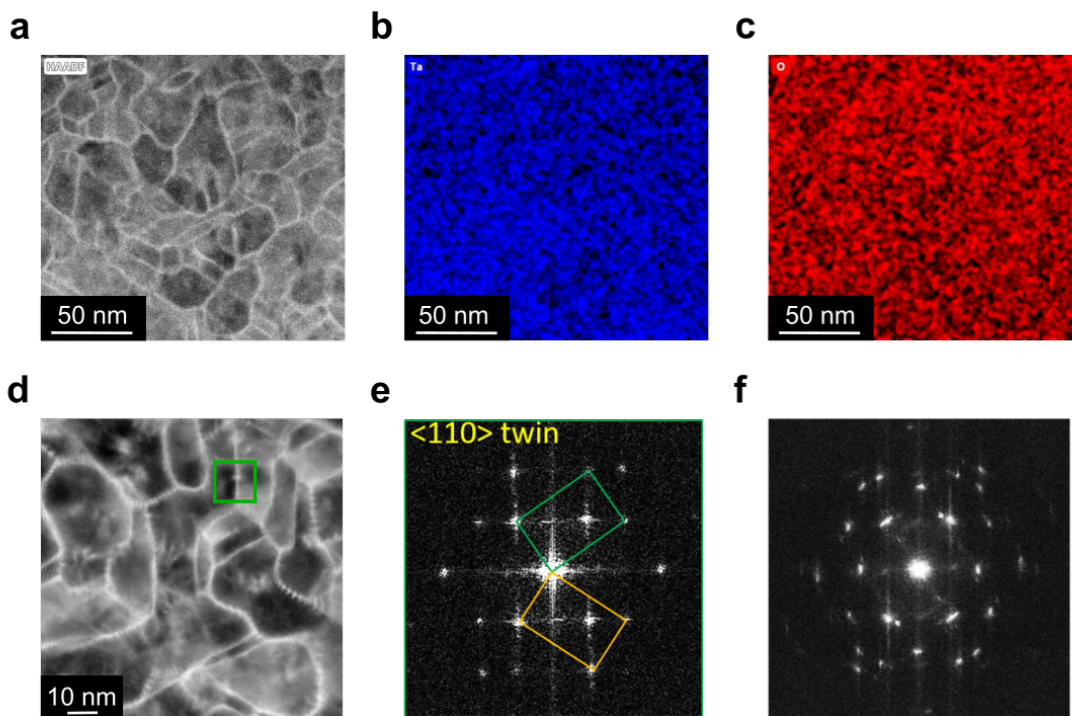


Figure 4.13: Grain Boundary Characterization. (a), Plane-view STEM image showing grain boundaries. (b), (c), EDS images of the same region shown in (a), displaying a uniform distribution of tantalum ((b)) and oxygen ((c)). (d), Atomic resolution STEM image of the boundaries. (e), Fourier transform of the STEM image at a grain boundary indicated by the green box region of (d), showing a pattern consistent with twinning. (f), Fourier transform of the entire image in (d) shows the rotational symmetries of the grains.

(figure 4.13 (e)). A diffraction pattern of the whole region in figure 4.13 (d) illustrates the rotational symmetries of the grains (figure 4.13 (f)).

4.5.4 Tantalum Oxide

An atomic-resolution STEM image of a 50 nm region of the tantalum surface reveals an amorphous oxide that is 2-3 nm thick (figure 4.12 (a)). We further study this oxide using XPS to estimate oxide thickness and composition over a larger area (250 μm spot size) (figure 4.12 (b), (d-f)). XPS scans of the tantalum film show two sharp lower binding energy peaks assigned to tantalum metal $4f_{7/2}$ and $4f_{5/2}$ orbitals (lower binding energy to higher binding energy, respectively), two peaks at higher binding energy corresponding to the same orbitals of Ta_2O_5 [91, 92], and two small $5p_{3/2}$ peaks corresponding to the metal and oxide, respectively [94]. Assuming the mean free path of electrons in tantalum is 2 nm at 1480 eV [95], and only taking into account inelastic scattering, a thickness can be estimated by comparing the ratio of oxide to metal peak areas. We corroborate this estimation using angle-resolved XPS (ARXPS), where we vary the angle between sample and detector, changing the relative distances that the emitted photoelectrons travel through the metal and oxide layers to reach the detector (figure 4.12 (b)). We account for this geometry in our modeling, and extract the oxide thickness at different angles (figure 4.12 (c)). The thickness estimation remains fairly consistent until higher angles, when other effects related to surface morphology or elastic scattering become more significant (figure 4.12 (c)) [96].

To investigate the variability of oxide thickness between devices, we show normal incidence XPS data from three devices from different tantalum depositions with different surface cleaning fabrication procedures (figure 4.12 (d-f)). In addition to variations in other fabrication steps, we note that the device shown in figure 4.12 (d) was only solvent cleaned, and the devices in figure 4.12 (e) and figure 4.12 (f) were piranha cleaned. The peak shapes and ratio of oxide to metal peak area are similar between all these devices, suggesting the oxide thickness and composition is robust to processing steps.

4.5.5 Sapphire-Tantalum Interface

We study the heteroepitaxial growth interface in our devices by directly imaging small regions of the sapphire-tantalum interface using iDPC STEM. In addition to the iDPC STEM image shown in figure 4.10 (e), we include an image showing the interface between sapphire and tantalum viewed from $\langle 1\bar{1}00|1\bar{1}00 \rangle$ sapphire and $\langle 100|100 \rangle$ tantalum zone axes (figure 4.14 (a)). We also propose atomistic models for an ideal sapphire-tantalum interface shown in figure 4.14 (b) and (c) to help visualize the lattice matching between sapphire and tantalum, and as a starting point for future studies on the impact of sapphire surface morphology on heteroepitaxial growth. For example, the interfacial dislocations visible in figure 4.10 (e) likely result from the 12.6% lattice mismatch between the $[1\bar{1}2]$ axis of tantalum and the $[11\bar{2}0]$ axis of sapphire (figure 4.14 (c)), as well as atomic layer steps in the sapphire that are evident in the STEM image.

4.5.6 XPS, AFM, XRD Characterization Details

All XPS, AFM, and XRD data were acquired using tools in the Imaging and Analysis Center at Princeton University.

XPS was performed using a Thermo Fisher K-Alpha and X-Ray Spectrometer tool with a $250 \mu\text{m}$ spot size. The data shown in figure 4.10 (d), figure 4.1 (c) and (d), and figure 4.12 (d-f) were obtained by collecting photoelectrons at normal incidence between sample and detector. The angle-resolved XPS (ARXPS) spectra shown in figure 4.12 (b) were collected by changing the angle between sample and detector. All AFM images were taken with a Bruker Dimension Icon3 tool operating in tapping mode (AFM tip from Oxford Instruments Asylum Research, part number AC160TS-R3, resonance frequency 300 kHz). The XRD spectrum shown in figure 4.6 was collected with a Bruker D8 Discover X-Ray Diffractometer configured with Bragg-Brentano optics. Two 0.6 mm slits were inserted before the sample, and a 0.1 mm slit was placed before the detector.

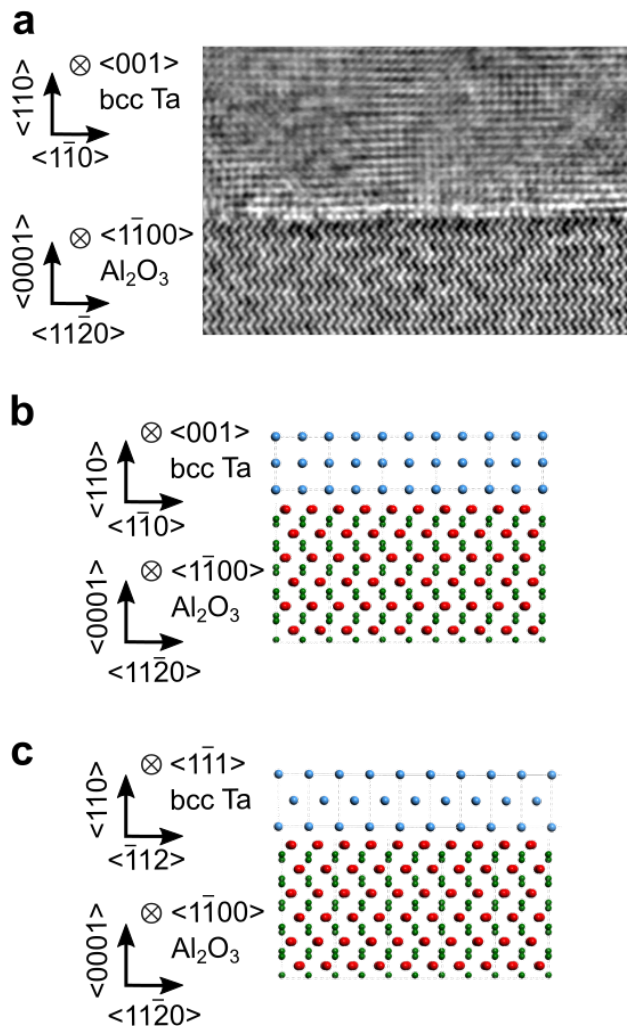


Figure 4.14: **Tantalum-Sapphire Interface Characterization.** (a), Atomic resolution iDPC STEM image showing the interface between tantalum and sapphire with the image plane perpendicular to the $\langle 100|100 \rangle$ direction of tantalum. (b), Atomistic model of the ideal interface for the tantalum column orientation shown in (a). (c), Atomistic model of the ideal interface for the tantalum column orientation shown in figure 4.10 (e). In both cases oxygen atoms are depicted in red, aluminum in green, and tantalum in blue.

4.5.7 Electron Microscopy Characterization Details

SEM and STEM images were also collected at the Imaging and Analysis Center at Princeton University. STEM thin lamellae (thickness: 70-1300 nm) were prepared by focused ion beam cutting via a FEI Helios NanoLab 600 dual beam system (FIB/SEM). All the thin samples for experiments were polished by a 2 keV Ga ion beam to minimize the surface damage caused by the high-energy ion beam. Conventional STEM imaging, iDPC, atomic-resolution HAADF-STEM imaging and atomic-level EDS mapping were performed on a double Cs-corrected Titan Cubed Themis 300 STEM equipped with an X-FEG source operated at 300 kV and a super-X energy dispersive spectrometry (super-X EDS) system.

Lithography and etching process development SEM images were collected with a FEI Verios 460XHR SEM and a FEI Quanta 200 Environmental SEM. Various tilt angles, working distances, and chamber pressures were used to eliminate charging effects.

4.6 Discussion

We have demonstrated that tantalum 2D transmon qubits exhibit longer T_1 and T_2 than the previous state of the art with remarkable consistency. Building on these relatively simple materials improvements, there are several areas of future research. First, $T_{2,Echo}$ is shorter than T_1 for all tantalum devices measured. Better shielding [97] and filtering [98] of tantalum transmons may enable measurements with unprecedentedly long T_2 , allowing for the exploration of microscopic mechanisms of relaxation and decoherence. Additionally, much can be learned from more systematic characterization of the effects of specific material properties on microwave losses. In particular, there are many open questions about the relative importance of oxide properties on device performance. An exciting avenue is to explore the detailed scaling of T_1 with surface participation by measuring tantalum qubits with different geometries. Additionally, we are exploring the impact of tantalum grain size and heteroepitaxial growth interface quality on T_1 and T_2 . Furthermore, it has been well-established that multi-qubit devices suffer from

significant variation between qubits [72], as well as variation over time in the same qubit [99]. An interesting question is how particular material choices quantitatively affect these variations, and whether judicious material choice can narrow the distribution of device properties. Finally, we note that while we have not made a direct comparison to all-aluminum qubits in this paper, the average T_1 achieved here is better than twice as long as the best published all-aluminum 2D transmon [73, 100]. Further, our process produces a higher and more consistent average T_1 than the reported state-of-the-art in 3D all-aluminum transmons [101–103]. The feasibility of eliminating aluminum by making all-tantalum qubits has yet to be explored.

More broadly, our results demonstrate that systematic materials improvements are a powerful approach for rapid progress in improving quantum devices. We have recently employed similar targeted materials techniques to improve spin coherence of shallow nitrogen vacancy centers in diamond [104], and we note that many other quantum platforms are also limited by noise and loss at surfaces and interfaces, including trapped ions [105, 106], shallow donors [107, 108], and semiconductor quantum dots [109]. Our general approach of modifying and characterizing the constituent materials may allow for directed, rational improvements in these broad classes of systems as well.

Chapter 5

Quantifying Sources of Loss

5.1 Introduction

What is the dominant source of loss in the transmons from chapter 4? T_1 measurements give a single number which could be influenced by many factors including quasiparticles, TLS, contact resistance, and packaging losses. Even if we knew the transmons are limited by materials, isolating the losses from tantalum, aluminum, and sapphire is nontrivial.

To study contributions of individual sources of loss, in this chapter we will move to a simpler device geometry: resonators. Composed only of tantalum (other than the substrate, wirebonds, and packaging), these resonators have an extra parameter that can be tuned: photon number. The photon-number saturation of Q gives a direct measurement of the materials loss of tantalum. Further, the rich temperature dependence of equation 2.51 can be used to fit for properties of the TLS in the device.

Once we establish a method to determine the sources of loss in our resonators, we employ this measurement to compare different processing steps and packaging techniques. Performing exploratory fabrication is significantly easier on resonators compared to qubits because Josephson junctions can easily be destroyed.

Finally we shift our focus back to qubits. We modify the resonator experiments to test the materials loss in transmons. Coupled with information about temperature and power independent losses from resonators, we narrow the likely dominant sources of loss

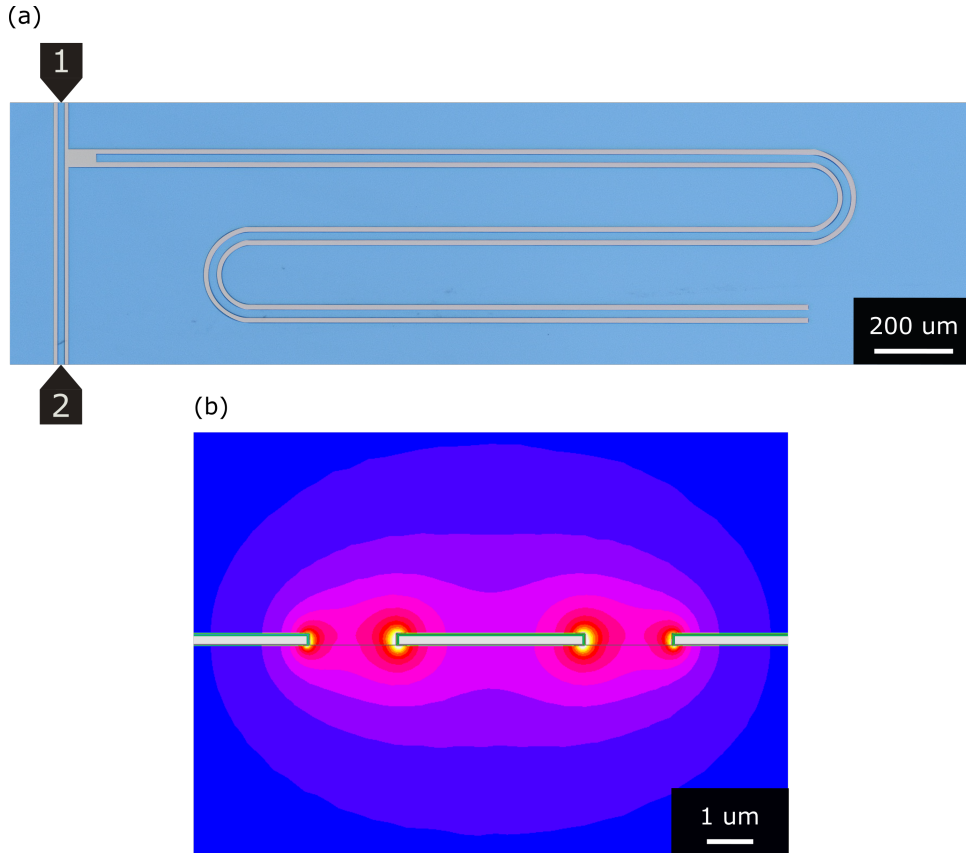


Figure 5.1: Coplanar Waveguide Resonator Overview. (a) Coplanar waveguide quarter wave resonator. The right end is shorted to ground, while the left end is floating and capacitively coupled to the feedline. The measurement equipment excite and readout the resonator through ports attached to the feedline. (b) Cross section simulation of a CPW using Ansys Maxwell. The electric field is overlayed over the substrate and vacuum regions. Note that the oxide regions, shown in green, are enlarged for visual clarity.

in our qubits.

5.2 Resonator Overview

This chapter presents measurements on two types of resonators. The first is a lumped element resonator, covered in section 1.2.1. The second type of resonator is a coplanar-waveguide (CPW) resonator, which we will introduce below.

5.2.1 Coplanar Waveguide (CPW) Resonators

A coplanar waveguide is a two-dimensional transmission line with a planar strip centerpin surrounded by ground planes on either side (figure 5.1). The centerpin acts as a geometric inductor while the gap to ground provides a capacitance.

Adding a reflecting element on either side of a strip of transmission line defines a cavity. In this case the reflecting element is either a break in the centerpin or a short to ground (figure 5.1 (a)). The resonance frequency of the cavity is determined by the speed of the propagating signal and the length of the transmission line:

$$\text{Length} = (2\pi\omega) \frac{v_p}{n} \quad (5.1)$$

where v_p is the phase velocity of the waveguide and n is 2 for a $\lambda/2$ resonator or 4 for a $\lambda/4$ resonator [110]. In order to drive and measure a resonator, we capacitively couple it to a “feedline” transmission line (figure 5.1 (a)). Modeling either end of the feedline as a 50Ω impedance to ground, we can calculate the analog of the Purcell decay (section 2.5.1) for resonators, the coupling quality factor, Q_c ([12], with an updated prefactor):

$$Q_c = \frac{\pi}{4} \frac{1}{\omega_0^2 Z_0^2 C_c^2} \quad (5.2)$$

where Z_0 is the characteristic impedance of the CPW and C_c is the coupling capacitance between the end of the resonator and the feedline.

5.2.2 Measurement Overview

To measure a resonator, a signal is sent in through port 1 of the feedline and measured at port 2 (figure 5.1 (a)). On resonance, part of the signal is diverted from the feedline and excites the resonator. A corresponding dip in transmission can be seen (figure 5.2 (c)). The width and depth of the dip can be used to calculate Q_c as well as the internal losses, Q_i [111]:

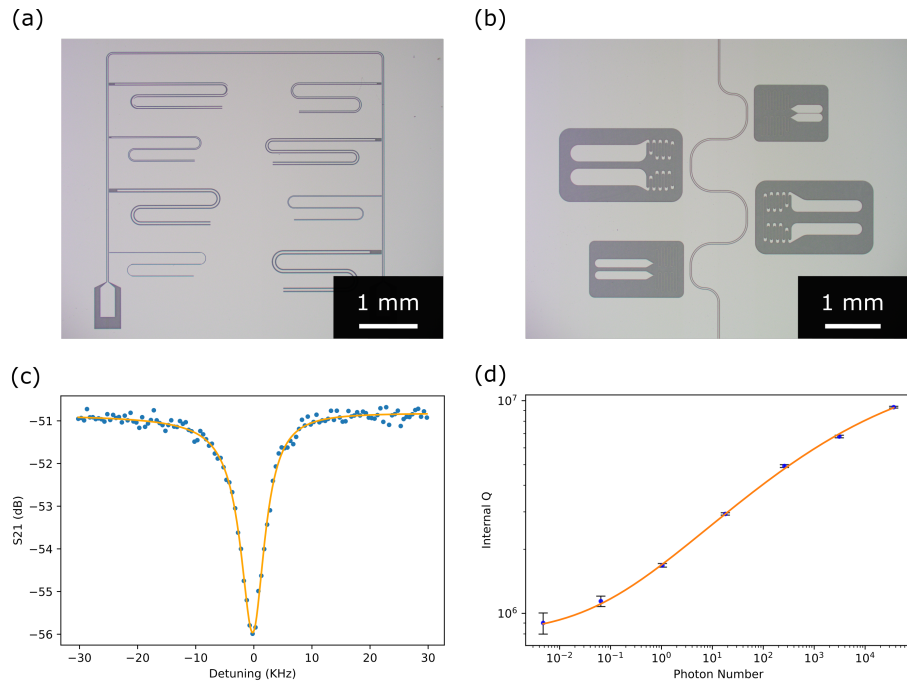


Figure 5.2: Multiplexed Resonator Measurements. Multiplexed CPW (a) and lumped element (b) resonator designs, allowing several different resonators to be measured on the same chip. (c) S21 measurement of a resonator which can be used to extract Q_i and Q_c . (d) Internal quality factor of a resonator as a function of photon number. Note the photon number is calculated assuming the measured attenuation on the drive line when the fridge is warm, leading to a possible systematic offset.

Q_{TLS0}	7.8e6
β_1	0.63
β_2	0.32
D	$14 \text{ K}^{-\beta_1}$
Q_{other}	13.5e6
T_c	4.1 K
η	9.1e-3

Table 5.1: **Fit Parameters of Resonator Temperature and Power Fit.** Fit parameters of figure 5.3. Note that η is a prefactor on the quasiparticle loss.

$$S21(\omega) = 1 - \frac{\frac{Q_0}{Q_c} - \frac{2jQ_0\alpha}{\omega_0}}{1 + 2jQ_0 \frac{\omega - \omega_0}{\omega_0}} + c \quad (5.3)$$

where $\frac{1}{Q_0} = \frac{1}{Q_i} + \frac{1}{Q_c}$, α is an asymmetry parameter, and c is an offset.

The internal resonator quality factor, Q_i , gives information about the dissipation in the resonator itself. Accordingly, Q_i can be used to determine the losses of a material, if other decay sources are accounted for.

5.3 Temperature Fits

Losses induced by TLS should saturate with both temperature and photon number¹. Measuring Q_i while changing the power and heat load applied to the device therefore can be used to distinguish the significance of TLS loss. Specifically, we fit to a model which includes TLS loss (equation 2.51), quasiparticle loss (equation 2.55), and a temperature-and power-independent loss source, Γ_{other} :

$$\Gamma = \Gamma_{TLS} + \Gamma_{QP} + \Gamma_{other}. \quad (5.4)$$

Figure 5.3 shows an example fit. We see that there are three different temperature regimes:

- **Low Temperature** In this regime the temperature dependence from the TLS T_2

¹Note that the photon numbers quoted throughout this thesis are an estimate calculated from a measurement of the attenuation of the fridge lines while warm. Cables were added and swapped throughout the measurements which could have further changed the photon number.

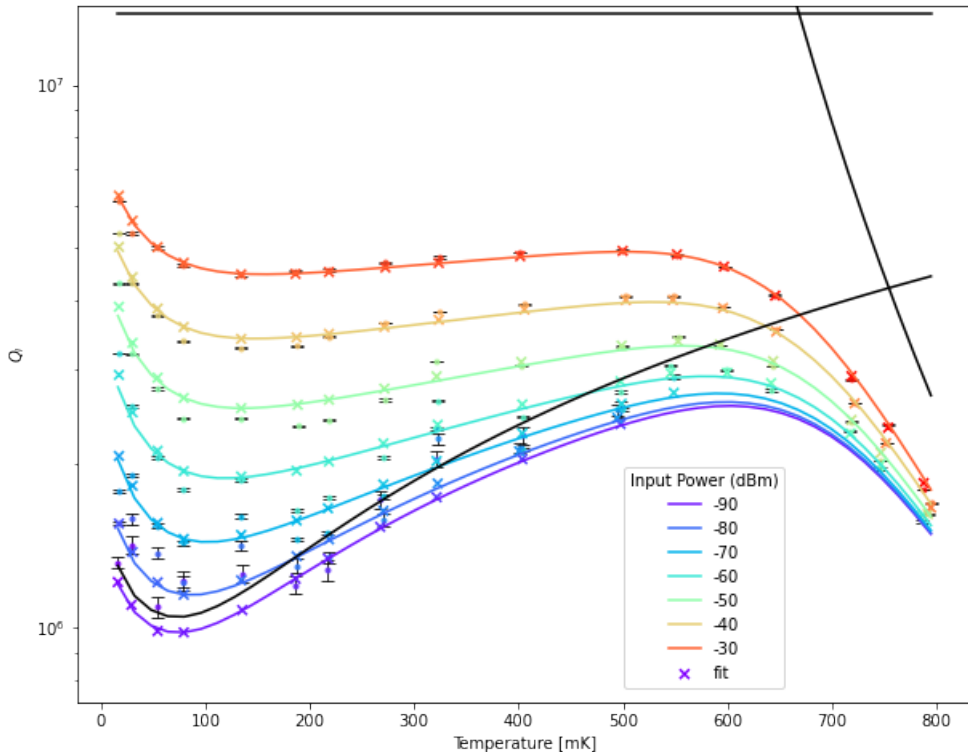


Figure 5.3: Resonator Temperature and Power Fit. Measurement of the internal quality factor of a resonator as a function of temperature and applied power. The circles represent experimental data points. The x's denote the fit to equation 5.4. Note that the photon number in equation 2.51 depends not only on applied power, but also how quickly the input power is dissipated. Given a single applied power, if Q_i changes the photon number in the cavity also changes. The colored lines are only guides to the eye. The black lines indicate the fit contributions of Q_{TLS} , Q_{QP} , and Q_{other} . The fit parameters are given in table 5.1.

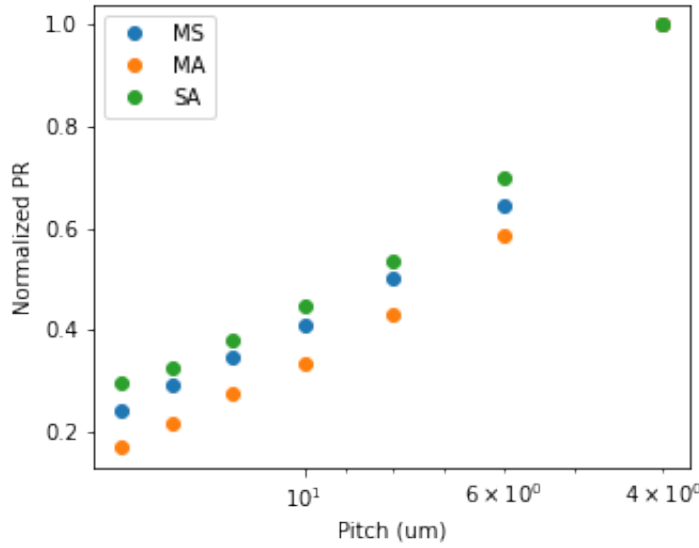


Figure 5.4: **Comparison of Resonator Interface Participation Ratio Pitch Dependence.** Metal-substrate, metal-air, and substrate-air interface participation ratio as a function of device pitch, normalized to the highest participation ratio.

dominates, giving a $1/T^{\frac{\beta_1}{2}}$ dependence (further discussed in section 2.3.7). This region is useful to determine the value of β_1 .

- **Medium Temperature (Approximately 150mK - 600mK)** Here the TLS are saturated by both thermal occupation (the numerator of equation 2.51) and changing TLS T_1 and T_2 . While the increasing TLS thermal occupation reduces decay, the TLS T_1 and T_2 temperature dependences both increase losses.
- **High Temperature** In this regime we are dominated by quasiparticle losses (section 2.4.2).

5.4 Varying Participation Ratios

Figure 5.3 shows that individual resonators are limited by TLS. We will now explore whether the limiting TLS are located in the interfaces or the bulk. If the TLS reside at the interfaces, then reducing the interface participation ratio should linearly increase Q_{TLS0} .

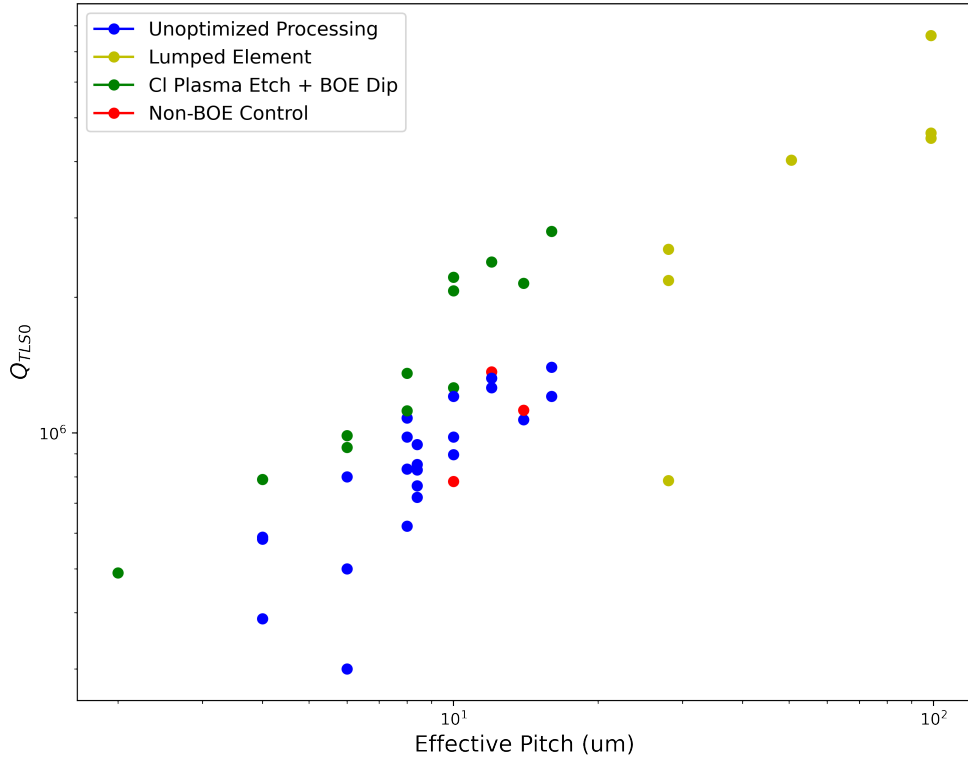


Figure 5.5: Q_{TLS0} Dependence on Pitch. Measurements of Q_{TLS0} extracted from temperature and photon number dependent resonator measurements as a function of pitch. The blue data points have a host of processing conditions, though none were dipped in BOE. We note that there are several uncontrolled variables in this dataset, including sapphire source and packaging method. This motivated the A-B comparison in section 5.5, for which the red data points are the control. The blue, green, and red data are from CPW resonators, while the yellow are from lumped element resonators. The effective pitch of the lumped element resonators is found by determining the CPW pitch that has the same metal-substrate participation as the measured design.

As figure 5.4 shows, the participation ratios of the metal-air, metal-substrate, and substrate-air interfaces change roughly linearly with resonator pitch, i.e. the distance between the centerpin and ground plane of a resonator. Accordingly we plot Q_{TLS0} against pitch in figure 5.5. The strong pitch dependence of the loss suggests the tantalum resonators are primarily interface TLS limited at low pitches.

5.5 Quantifying Effects of Fabrication Procedures: BOE

Now that we have the ability to quantify the TLS, quasiparticle, and temperature and power independent losses in our samples, we can measure the effect of changing processing conditions on these sources of decay. As an example, we will consider an optional buffered oxide etch (BOE) dip.

Dipping niobium resonators in BOE was shown to reduce resonator losses [112]. A similar BOE treatment can be shown to alter the oxide of tantalum (figure 5.6). Figure 5.5 shows that the BOE treated resonators on average perform better than non-BOE treated resonators. However, many of those data points have additional confounding variables.

In order to determine the effect of BOE on loss tangent, we measure two samples that are nominally identical other than a 20 minute 10:1 BOE dip at the end of processing. The fabrication procedure is similar to the photolayer in chapter 4 except the tantalum deposition (see appendix B), the substrate (sapphire from Crystal Systems, formerly GT Advanced Technologies), and a chlorine plasma etch (see appendix C). Further these samples are packaged in the QCage (QDevil APS). The results (figure 5.7) show that Q_{TLS0} improves with BOE treatment, though the sample size is currently small.

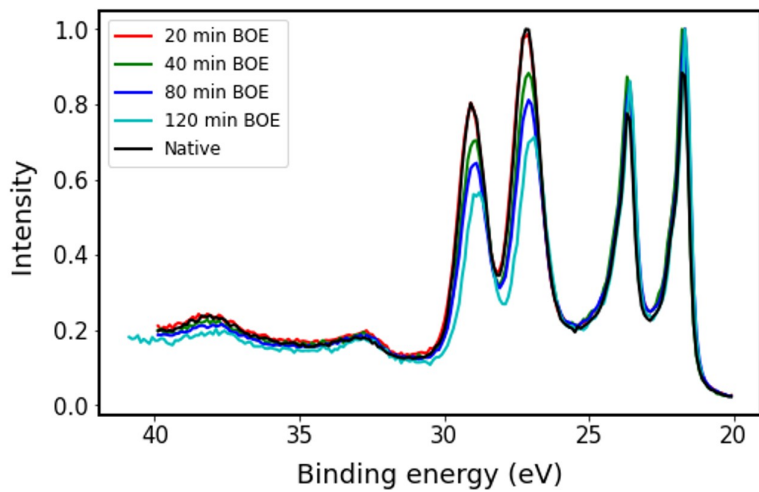


Figure 5.6: **BOE Oxide Thickness Measurement.** (a) XPS measurement of the tantalum oxide (26-30eV) and tantalum 4f metal (21-25eV) peaks as a function of 10:1 BOE dip timing. The decreasing height of the oxide compared to the metal signal shows the oxide thickness reduces with dip duration.

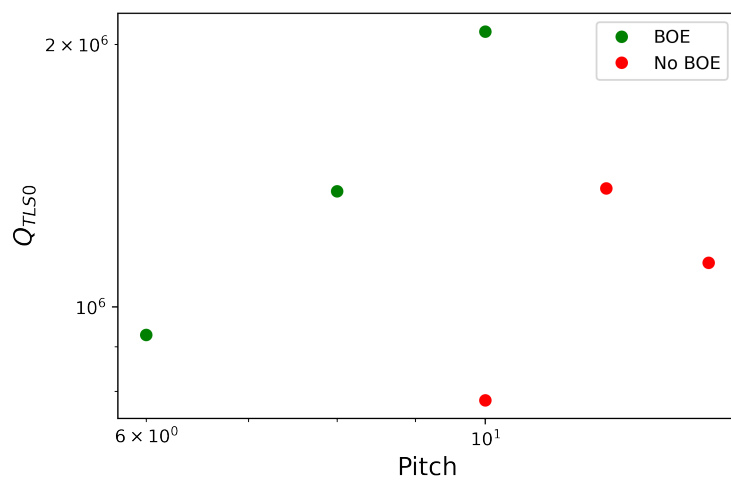


Figure 5.7: **Effect of BOE on Q_{TLS0} .** Simplified version of figure 5.5 with data from two samples that were processed nominally identically other than a BOE dip.

5.6 Q_{other} Comparison

The Q_{other} of many of the CPW resonators in figure 5.5 is less than 10 million—alarmingly close to the transmon quality factors measured in chapter 4. However CPW resonators have a much larger footprint than transmons, suggesting that if Q_{other} is packaging related then it could significantly differ between CPW resonators and transmons.

In order to gauge the Q_{other} of a geometry closer to a transmon, we measure lumped element devices. All of the lumped element data presented here is taken in the commercially available QCage packaging by QDevil APS. A comparison of Q_{other} for CPW and lumped element resonators is shown in figure 5.8. Note that high power measurements of resonators are plagued by nonlinearities in the S_{21} traces, limiting the maximum power used in the measurement. Accordingly, the highest power data taken in many high- Q_{other} device datasets (including figure 5.3) has minimal effect from Q_{other} , creating a large fit uncertainty. We can still rely, however, on these fits to indicate whether or not Q_{other} is much greater than the highest Q_i values measured, roughly 10 million. A further caveat to this dataset is that several other lumped element resonators are only partially measured and therefore aren't included in the dataset presented. However, the initial measurements indicate significantly lower Q_{other} —further investigation into the cause of these low Q_{other} is important future work.

Both substrate classical dielectric loss as well as packaging loss could contribute to Q_{other} —and both losses are likely similar between a lumped element resonator and a transmon. It is therefore unlikely that a transmon with quality factor 10 million, packaged in the same sample holder with a similar substrate to the measured lumped element devices, is limited by either packaging or classical sapphire losses². More trials are needed to confirm this result.

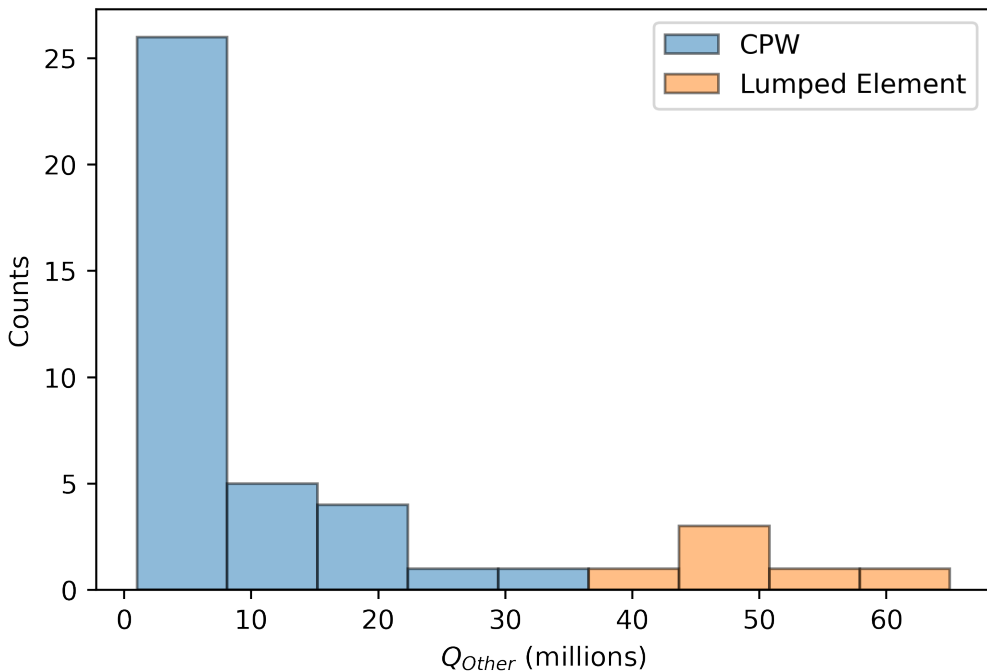


Figure 5.8: **Comparison of CPW and Lumped Element Q_{other} .** Comparison of Q_{other} from the power and temperature dependent fits used to make figure 5.5. One lumped element device with fitted $Q_{other} = 180e6$ was omitted to increase the resolution of the rest of the dataset. One set of lumped element resonators presented here was made on sapphire from Crystec GMBH with a commercial deposition from Star Cryoelectronics. The rest were fabricated on sapphire from GT Advanced (now Crystal Systems) with the deposition described in appendix B.

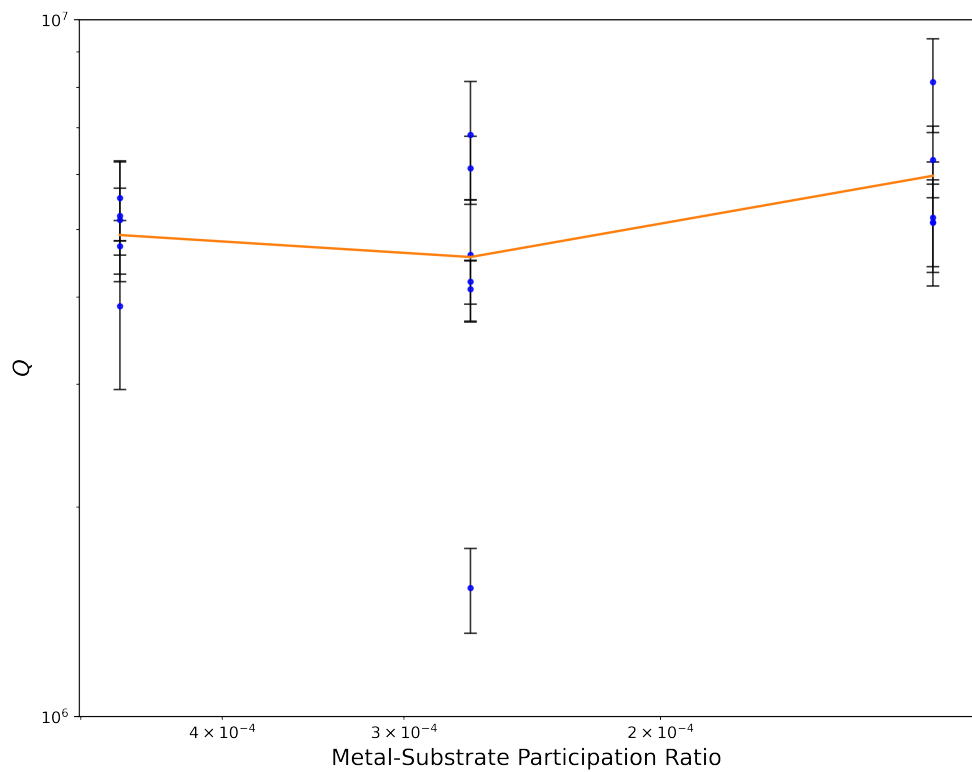


Figure 5.9: **Qubit Quality Factor Dependence on Participation Ratio.** Transmon quality factor as a function of the metal-substrate participation ratio. The orange line links the average quality factors for each design. The participation ratios are calculated following appendix F.

5.7 Comparison to Qubits

To determine if our transmons are also limited by the tantalum capacitor pad interfaces, we test if their quality factors scale with the corresponding participation ratios. The capacitor pad interface participation ratios can be changed by adjusting the distance between the pads (the qubit “pitch”), while reducing the width of the capacitor to maintain an approximately constant E_c (see appendix F). The aluminum junction design and all tantalum within about $10\mu\text{m}$ of any aluminum is kept fixed³.

We measure transmons with nominal pitches of 5, 15, and $65\mu\text{m}$. The transmons, presented in figure 5.9, are made with several different fabrication procedures. Modifications to section 4.2 on some devices include a BOE dip before spinning electron beam resist, a BOE dip after junction fabrication with a photoresist cover shielding the junctions, a chlorine plasma etch (appendix C), a new substrate source (sapphire from Crystal Systems, formerly GT Advanced Technologies), and packaging in the QCage from QDevil APS. None of these fabrication variations significantly change T_1 , though only a small sample size was measured.

Figure 5.9 shows the transmon quality factor pitch dependence is close to flat. This suggests a limiting loss source other than the interfaces of the transmon capacitor pads. Further discussion can be found in chapter 6.

²Note that we have not yet measured a qubit in the QCage (QDevil APS) with GT Advanced (now Crystal Systems) sapphire which didn’t have an obvious fabrication problem.

³Small changes in junction street width (see figure D.1) are made to adjust qubit frequencies.

Chapter 6

Conclusion and Outlook

In this thesis we show the importance of considering materials when designing superconducting qubits. The interfaces of the substrate and superconducting metals can be amorphous and contain fabrication debris. These may host two-level systems that spuriously couple to the qubit. Further, the critical temperature and response to magnetic fields of qubit materials affect quasiparticle decay and vortex dissipation. Many of these materials properties can be quickly measured with spectroscopic techniques.

We showed that switching the transmon capacitor pad from niobium to tantalum significantly increases qubit T_1 . The oxide layer of tantalum is both smaller and has a simpler stoichiometry, and the sampled tantalum-sapphire interface is almost atomically clean. The spectroscopic techniques employed to develop the optimized fabrication recipe may be helpful to future materials studies.

We then characterized the TLS loss in tantalum superconducting devices by measuring resonators. Power and temperature dependent measurements of the internal quality factor show the dominant decay mechanism is interface TLS loss. We find a low-temperature saturation of quality factor likely due to the freezing out of spurious TLS interactions. This measurement further allows us to delineate the loss sources in resonators. We use this to test the effects of both BOE treatments and packaging.

Though significant, we found the tantalum capacitor pad interface losses likely do not limit our transmon T_1 . Further, we have found a method to help determine if either

classical sapphire or packaging losses limit our transmons. Future work includes exploring the aluminum junction interface losses, held approximately constant in the transmons measured.

There are many promising qubit materials and fabrication techniques that haven't been characterized yet. Section 3.2 outlines several considerations for selecting new materials. The search for these materials could be critical for the current path to scalable superconducting quantum processors.

Appendix A

Detailed Fabrication Procedures

A.1 Detailed Transmon Fabrication Procedure

A.1.1 Substrate and Substrate Preparation

- Start with a high-purity sapphire wafer. The highest purity readily available sapphire wafers we use are HEMEX sapphire from Crystal Systems (formerly GT Advanced Technologies). Perform a 3:1 Piranha dip for 5min, remove the piranha in DI water, and then dip the wafer in IPA before blow drying. Blow drying water off sapphire can easily leave residue.
- Precondition the sputterer, then load the wafer and deposit 200nm of tantalum (see appendix B).

A.1.2 Photolithography

- To remove any liquid from the chip, bake at 110C for 2min, then load the sample onto a spin chuck. Perform a dry spin to ensure any dust is removed from the sample.
- Spin AZ 1518 at 4000rpm for 40s, then bake for 1min at 95C.
- Expose the photolithography pattern. We use a Heidelberg DWL with a 10mm write head, optical focus, and a 50% filter with a beam intensity parameter of 30.

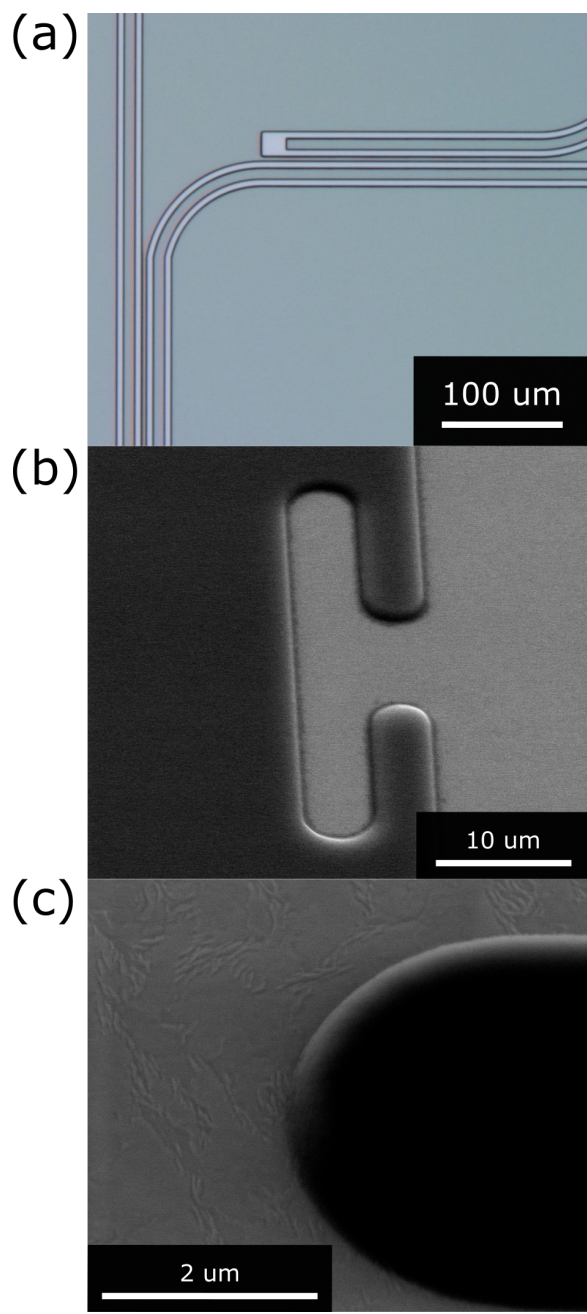


Figure A.1: **Lithography Overview.** (a) Optical image of developed photoresist patterned into resonators. (b) SEM image of photoresist on top of tantalum. (c) SEM image of a device similar to (b) except after the oxygen descum step.

- Develop for 90s in AZ300 MIF, swirling once per second. Finish in DI water.
- Hard bake the resist on the sample for 2min at 110C.

A.1.3 Etch

- Mount the sample to a silicon carrier wafer with thermal tape. We have seen the material of the wafer significantly change the results of the etch. Further, ensure good contact through the thermal tape—this can significantly change the etch time. Ensure that the thermal tape covers almost the entire backside of the sample (an uneven etch rate has been observed when the tape only partially covers the backside).
- Perform an oxygen descum for 1min: 30mTorr, 30sccm O_2 . 20/200W Bias/ICP. The resist should look similar to figure A.1 (c).
- Run the tantalum etch (see appendix C).

A.1.4 Clean

- Strip the resist for 1 hour in 1165 at 80C.
- Sonicate in the hot 1165 for 1min.
- Perform a "TAMI" clean: move the sample to toluene, sonicate for one minute, and then repeat for acetone, methanol, and IPA (sometimes methanol is excluded).
- Perform a 20min 2:1 piranha dip. Finish in DI water then blow dry.
- An optional 20min 10:1 BOE dip may be added here.

A.1.5 Electron Beam Lithography

- Mount the sample on the spinner and perform a dry spin to remove dust.

- Spin MMA 8.5 MAA (5000rpm for 70s), bake for 2min at 175C, then spin PMMA (we have used A3, A4, and A4.5, with spin parameters around 5000rpm for 60s). Bake for 5min at 175C.
- Deposit a 40nm Al anticharge layer using an ebeam evaporator at 0.4nm/s.
- Dice the sample to the desired size. Note that to mount the sample to the dicing tape, the chip is placed face down. The anticharge layer and two layers of resist protect the patterned tantalum.
- Expose with the ebeam. Ensure good contact between the sample stage and the top anticharge layer. We use a Raith EBPG. Typical doses are $1620/225 \frac{\mu C}{cm^2}$ full-clear/undercut (see recipe development notes in appendix D). Typical beam currents are 5nA with a 300um aperature.
- Remove the anticharge layer by letting the device sit in MF319 for 4min.
- Swirl the sample in DI water for 30s.
- Thoroughly blow dry.
- Swirl the sample in MIBK:IPA 1:3 for 50s, 1 swirl per second.
- Swirl the sample in IPA for 10s at 1 swirl per second.
- Thoroughly blow dry.

A.1.6 Junction Deposition

- Pump the evaporator down (in our case a Plassys MEB550S), then ion mill along the same directions and angles as the deposition for 30s at 400 V and 60mA. Pump 4scm of Ar into the chamber during the etch.
- Perform a getter by depositing 0.3nm/s of Ti for 1.5min.
- Deposit 20nm of aluminum (which results in 15nm on the tilted sample) at 0.4 nm/s at a pressure of $\sim 10^{-7}$ mBar along the first street (with the normal vector to the

substrate tilted at a 40° angle away from the target), keeping in mind the orientation of the already-patterned photolayer in order to create a good tantalum-aluminum contact (figure E.4).

- Oxidize for 15min at 200mBar. The gas fed to the chamber is 15% oxygen, 85% argon.
- With the same deposition conditions, deposit 70nm of aluminum (which results in 54nm on the tilted sample) in the second street (with the normal vector to the substrate tilted at a 40° angle away from the target).
- Oxidize for 20min at 40mBar.
- Strip the resist for 3h in Remover PG at 80C.
- Sonicate for 10s in hot Remover PG while holding the sample with tweezers to ensure it doesn't move much.
- Swirl in IPA for 10s.
- Thoroughly blow dry.

A.2 Detailed Resonator Fabrication Procedure

Resonators and qubits are processed identically up to and including the etching step (section A.1.3). In the case of resonators, after the etch we dice and perform the final cleans. In order to dice we put a protective layer of photoresist on the sample. However, we have found it is important to take the previous layer of resist used in the etch off first—if not this resist becomes very difficult to remove later. The steps are as follows:

- Strip the resist for 1h in 1165 at 80C, sonicate for 1min in the hot 1165, then perform a TAMI clean as described in section A.1.4.
- Spin and bake 1518 using the same parameters as section A.1.2.
- Dice the resonators.

- Strip and clean the device with the same procedure as section A.1.4. An optional BOE dip (10:1, 20 min) or other experimental fabrication steps may be added here.

Appendix B

Tantalum Deposition

B.1 Optimized Recipe

To deposit α -tantalum, we first precondition the sputtering chamber by heating the inconel chuck for 65 minutes at 875C followed by a 25 minute tantalum deposition. We then load a sapphire wafer and bake it for 25 minutes at 875C¹. Ramping the temperature to 750C, we deposit at a pressure of 3 mTorr and power of 250W for 1500s. We verified our deposition parameters with measurements of the diffraction pattern (figure B.1) as well as temperature and field dependent resistance (figure B.2).

¹Note that the temperatures quoted in this paragraph are nominal temperatures read by the instrument. The actual temperatures are on the order of 100C lower according to the tool manufacturer

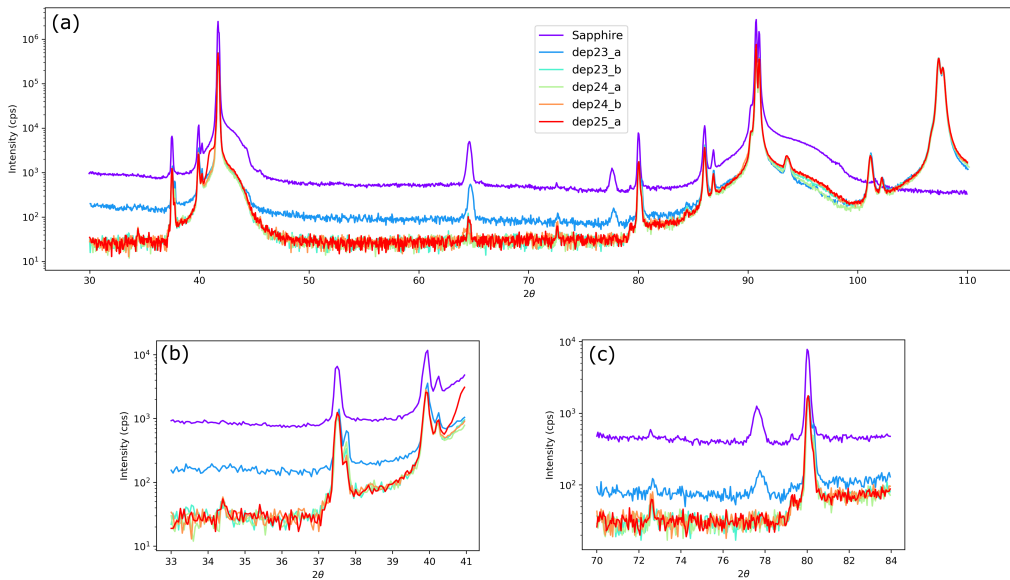


Figure B.1: XRD of Working Tantalum Deposition. (a) XRD measurement of a sapphire wafer as well as three nominally identical depositions. Two locations were measured for two of the depositions. (b) and (c) show zoomed-in regions of (a).

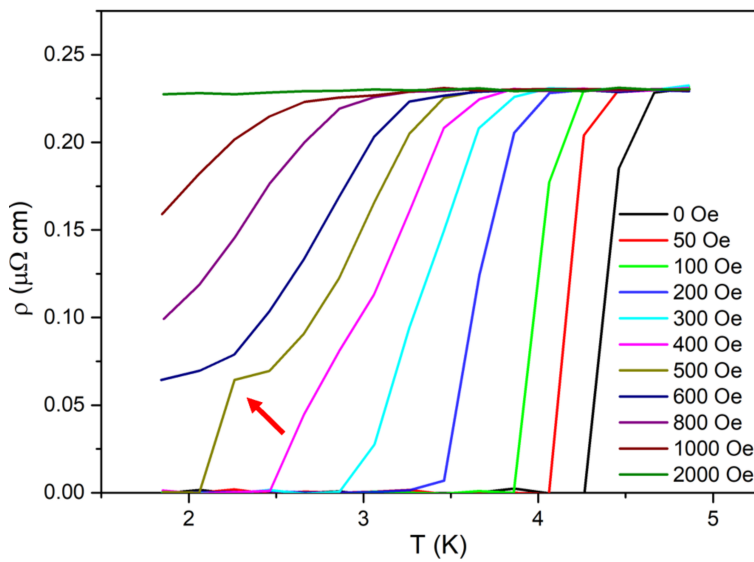


Figure B.2: PPMS Measurement of Working Tantalum Deposition. Measurement of the resistance across a tantalum film as a function of temperature and applied magnetic field. Note that the hump denoted by the red arrow may suggest the presence of two phases in the tantalum film.

Appendix C

Tantalum Etches

Initially we etched tantalum using a reactive-ion etch (8:3:2 CHF₃:SF₆:Ar chemistry at 50 mTorr, RF/ICP power of 100 W/100 W). However, scanning electron microscopy (SEM) images showed this and similar etches to produce rough edges as well as small pillars and boulders near the sidewalls, likely due to micromasking (figure C.1 (a), (b)). The anomalous objects in figure C.1 (b) remained after the device was cleaned in piranha solution and treated in an oxygen plasma. In order to avoid these fabrication problems, we employed a wet etch composed of 1:1:1 HF:HNO₃:H₂O. We found that several resists delaminated before the tantalum was etched through, leaving the sidewalls and nearby tantalum visibly rough in SEM (figure C.1 (c)). This problem was partially circumvented by using thick AZ 1518 resist (approximately 2 μ m tall) which left cleaner sidewalls (figure C.1 (d)). Comparing Devices 4-10 with Devices 11-18 in table 4.1, we note the optimized wet etch likely improved T_1 .

The resist delamination problem was helped by the thicker resist, though on some devices clear sidewall roughening persisted. To increase the fabrication yield, we optimized the dry etch to get rid of the rough sidewalls previously seen with the fluorine etch. Accordingly, we use a chlorine dry etch (1:1 Cl₂:Ar, 5.4 mTorr (though over time this number has fluctuated slightly), Bias 50W, ICP 500W, 2min). The resulting sidewall is shown in figure C.2.

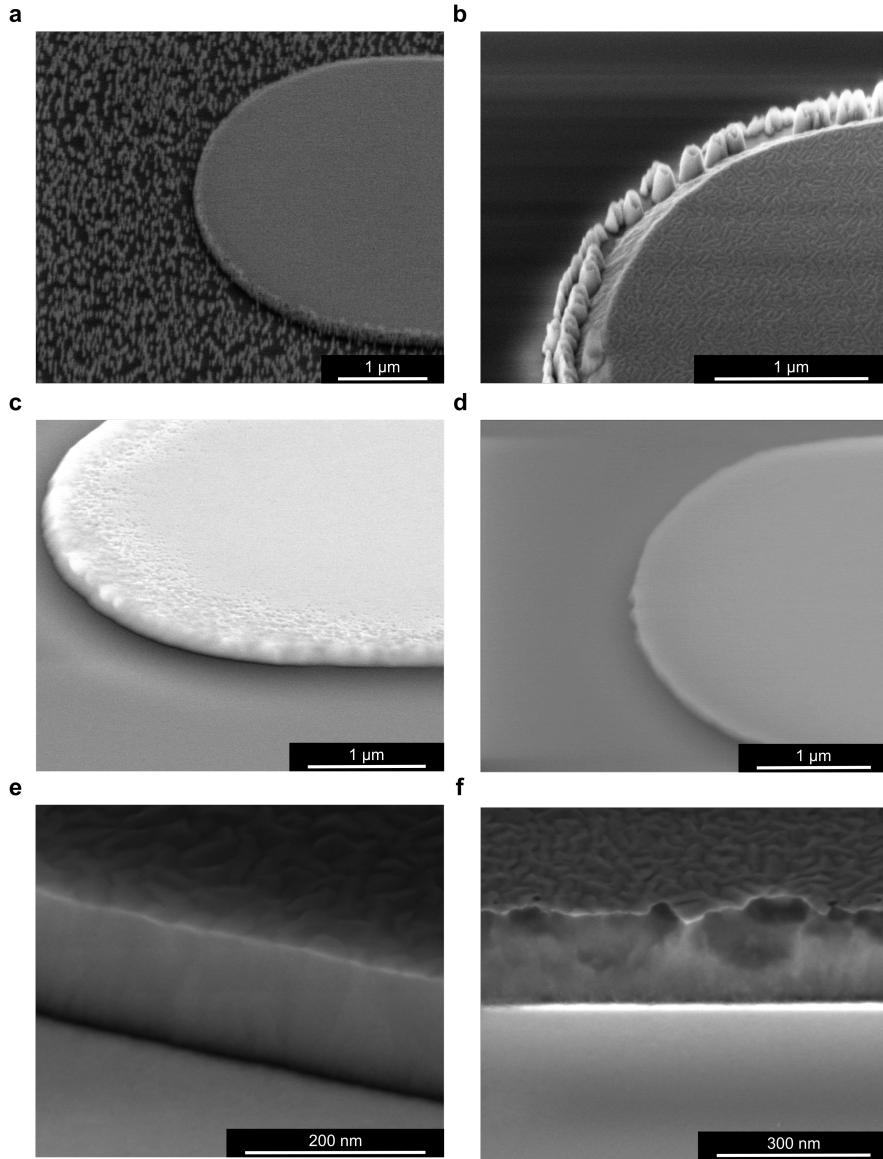


Figure C.1: Scanning Electron Microscopy Images of Tantalum Etch Development. All panels show etched tantalum on top of sapphire. (a), (b), Examples of surface roughening after a 8:3:2 CHF₃:SF₆:Ar dry etch with a 5-7 mTorr pressure and RF/ICP power 30 W/30 W ((a)) and 100 W/100 W ((b)). The rough features near the sidewalls in (b) survived both a piranha clean and an oxygen plasma etch. (c), Initial wet etch results showed roughening of the tantalum near the edge of the pad, which was circumvented ((d)) by employing a thicker photoresist. (e), (f), Higher magnification images of sidewalls etched with the optimized wet etch.

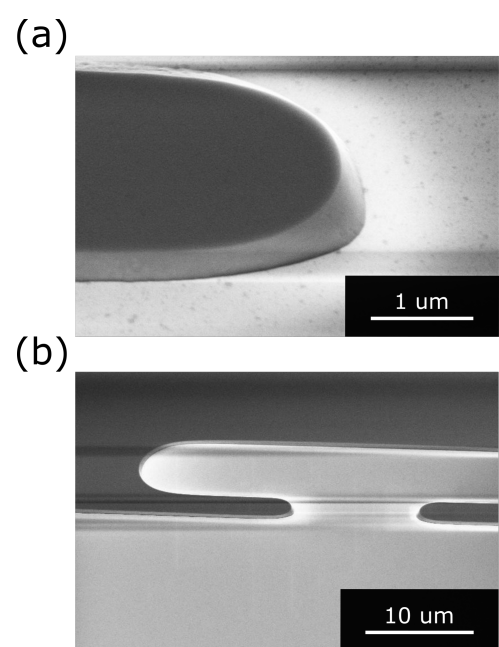


Figure C.2: **Chlorine Plasma Etch.** Tantalum etched on top of sapphire. Note the sloped sidewalls in comparison with the wet etch in figure C.1.

Appendix D

Josephson Junction Fabrication

D.1 Manhattan Junction Overview

We primarily use Manhattan Josephson junctions for their ease of fabrication. To make a Manhattan, first several trenches as shown in figure D.1 (a) are exposed in resist using electron beam lithography. The actual junction is formed at the intersection of the streets, while the highways connect the junction to the tantalum capacitor pads (not shown).

Next, aluminum is evaporated at roughly a 45° angle to the plane of the sample, in a direction selectively chosen to only coat one street. The other street is too narrow to allow aluminum to hit the sapphire. Instead, the aluminum coats the walls of the resist—when the resist is removed, so will this extra aluminum¹.

The evaporator chamber is then filled with oxygen and all exposed aluminum is oxidized, forming what will become our oxide barrier. Finally, aluminum is deposited along the second street, selectively coating the remaining empty exposed area. The oxide barrier resides where the two streets intersect.

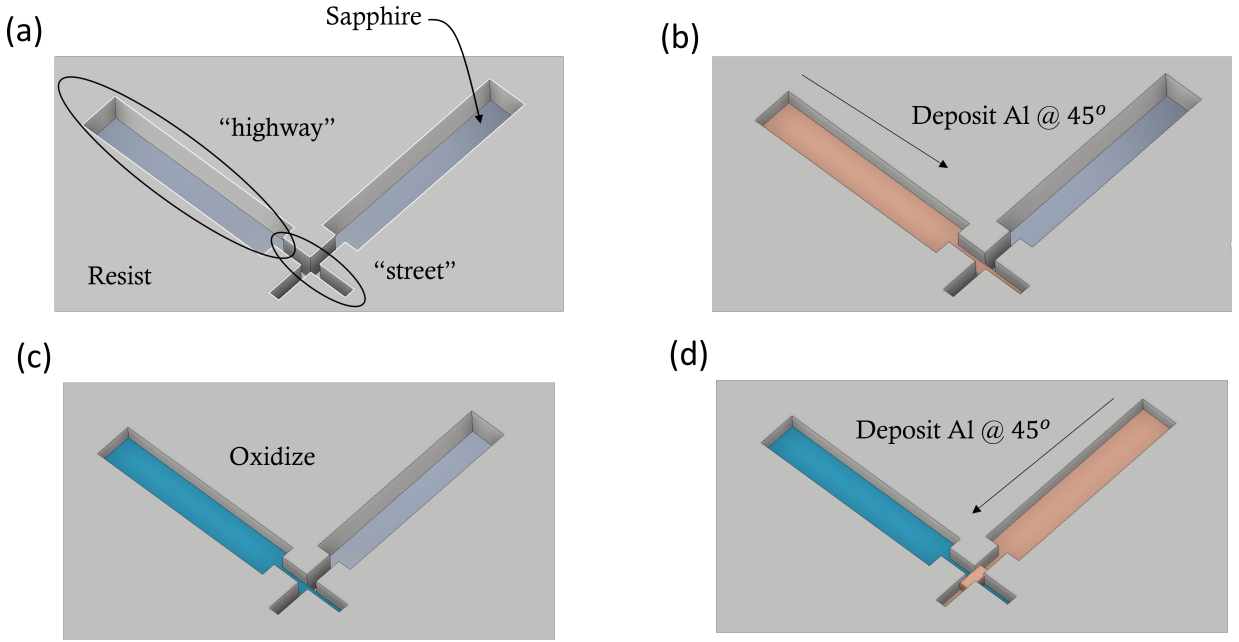


Figure D.1: Josephson Junction Fabrication Overview. Bare aluminum is shown in orange while oxidized aluminum is shown in blue.

D.2 Exposure Problems

D.2.1 Flagging

If aluminum is deposited at an angle to a wall of resist, the side of the wall will be covered (figure D.2 (a)). When the resist is removed, the aluminum coating the wall may not be. This is circled in red in figure D.2 (b) and is called "flagging". To stop this problem, an "undercut" region, which is essentially an awning overhanging the resist sidewall, can be used to disconnect the aluminum on the sapphire and the aluminum on the resist, leaving clean edges (figure D.2 (c)).

D.2.2 Residual Carbon

The full electron beam exposure pattern connecting two tantalum pads is shown in figure D.3. The large squares on either side are meant to give a large aluminum to tantalum contact area, which are then connected to the junction streets by highways (see figure

¹Note that the highway perpendicular to the deposition is sufficiently wide that some aluminum will coat the sapphire. To first order this can be ignored, though this may cause problems with unintended junctions later on.

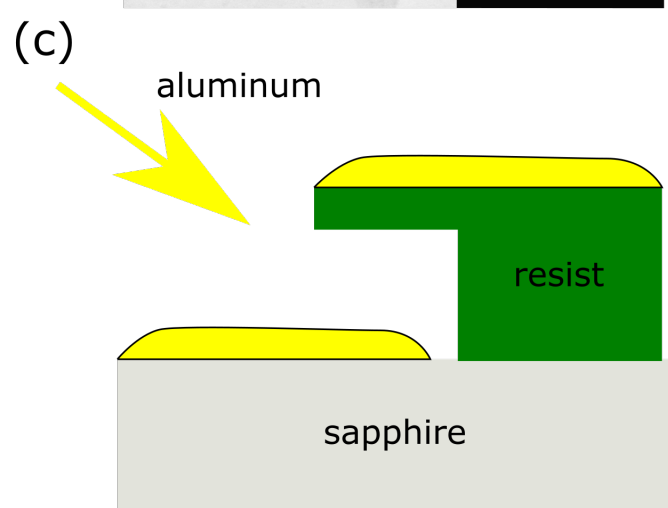
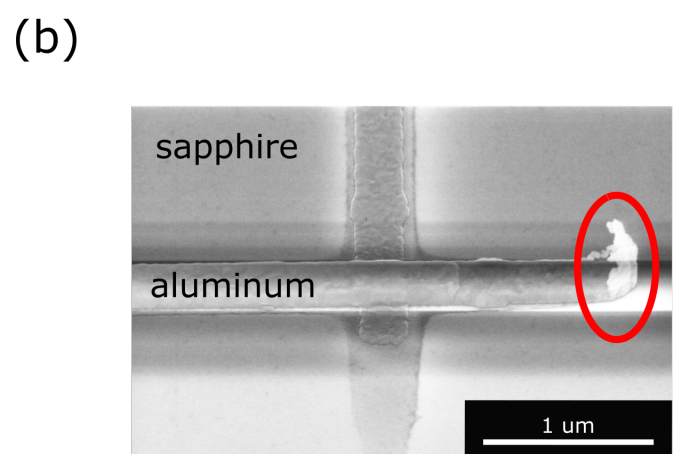
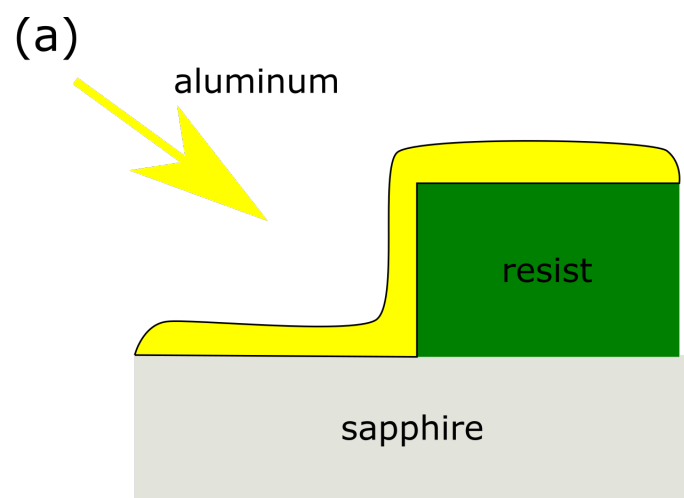


Figure D.2: Undercuts and Flagging.

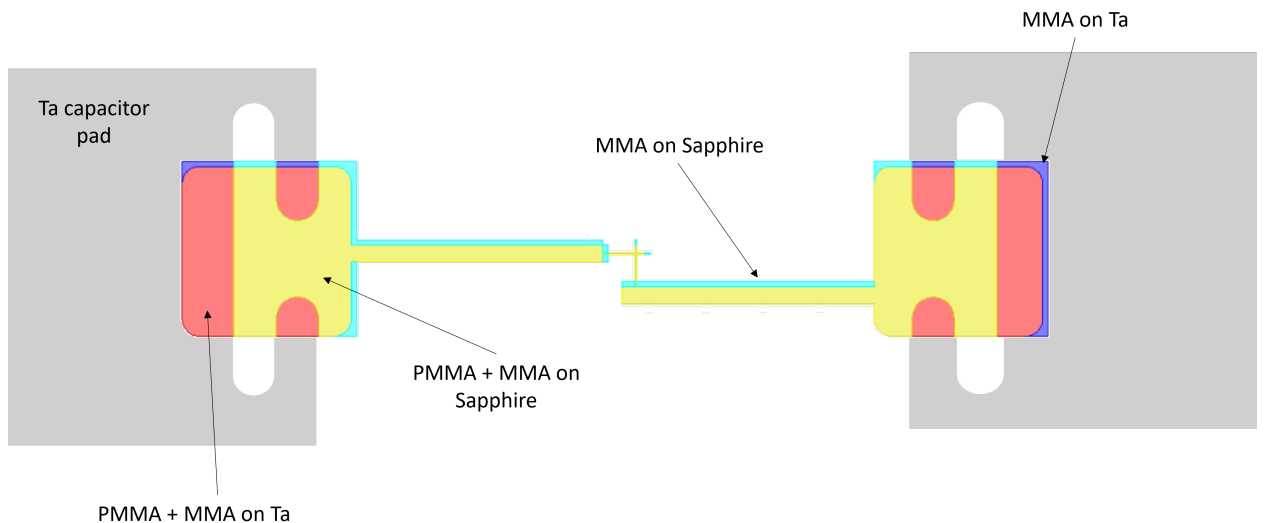


Figure D.3: **Dose Regions for Electron Beam Exposure.** Figure made using Beamer (GenISys GmbH).

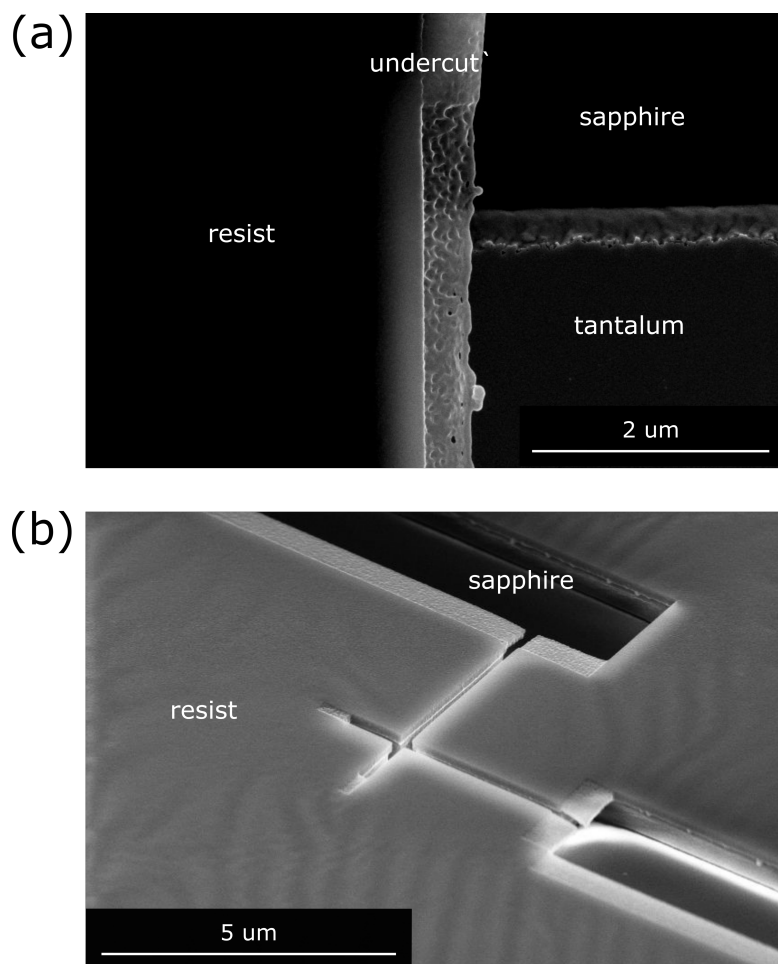


Figure D.4: **Undercut Problems.**

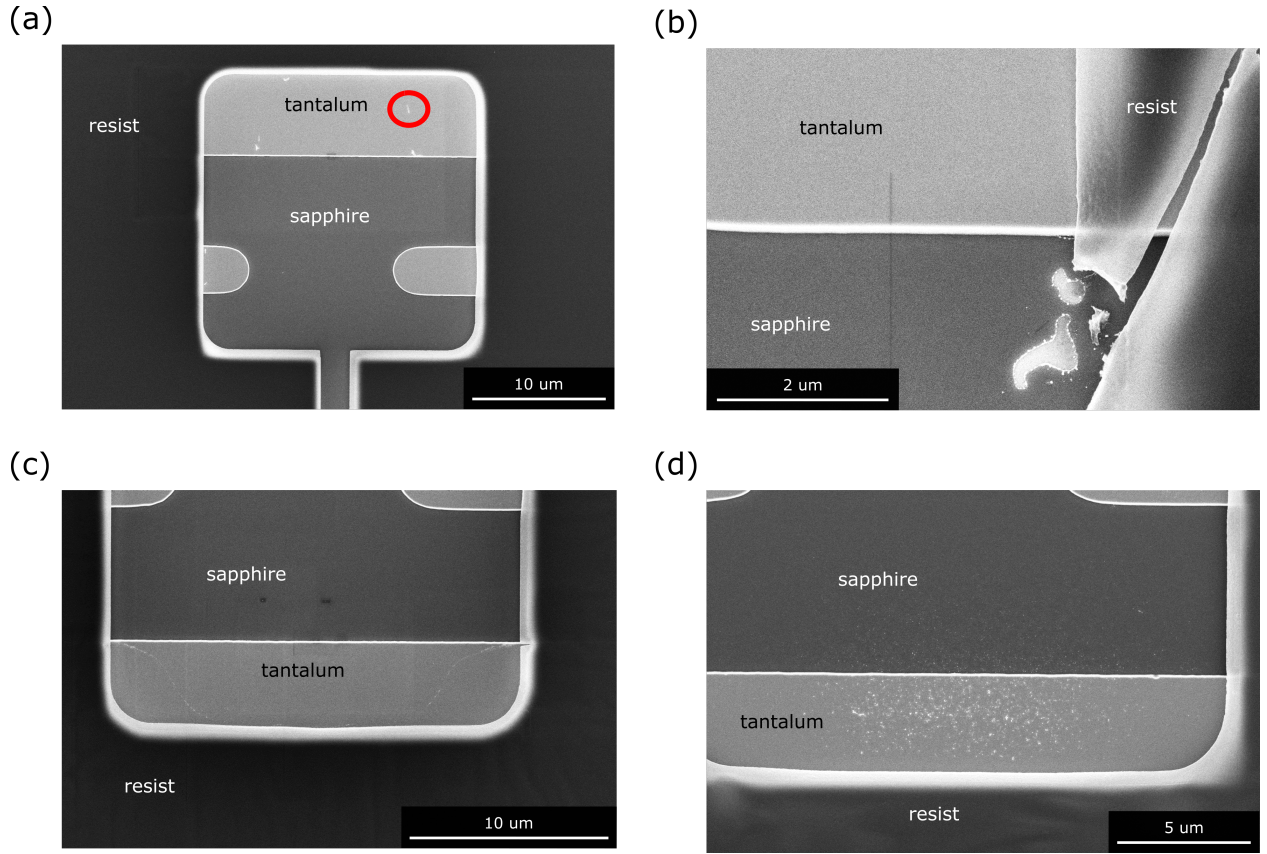


Figure D.5: **Unclean Exposure.**

D.1 for nomenclature).

In order to expose undercut regions (section D.2.1), we use a resist stack of around 600nm of MMA covered by roughly 100nm of PMMA. The MMA is exposed at a lower electron beam current than the PMMA, and therefore exposing an undercut region (light and dark blue in figure D.3) at the MMA dose will leave the PMMA “awning” intact.

To add to the complexity, the exposure dose of both MMA and PMMA is dependent on the material underneath—either tantalum or sapphire. This suggests that ideally four different doses are used to make a junction. An undercut dose that works on sapphire easily may not work on top of tantalum, as shown by the significant decrease in undercut width in figure D.4 (a). A properly dosed undercut should look similar to figure D.4 (b).

Improper dosing can lead to residual residue visible in scanning electron microscopy images, likely carbon. Figure D.5 (a) shows white spots which may be from underexposed resist. However, overexposing resist can also lead to residue: figure D.5 (b) shows cracking possibly from too large of a dose. Pieces of this crack could then roll, which likely left

the trail in figure D.5 (c), or explode which could have left the residue in figure D.5 (d).

Appendix E

How to Design a Transmon

The goal of this appendix is to help a reader with little superconducting qubit experience make a device. It serves as a recipe and doesn't attempt to derive many of the formulas. Theoretical justifications can be found in many previous publications, especially [12, 110, 113].

E.1 Transmon Design

First we'll cover the desired parameters of our transmon Hamiltonian, then we'll give a recipe for laying out the device design.

E.1.1 Transmon Hamiltonian Parameters

Designing a transmon requires several trade-offs. The following are important considerations:

- First of all, the anharmonicity ($\approx E_c$) should be large enough to ensure sufficiently fast gate speed. Devices in this thesis normally have an E_c of approximately 200MHz.
- Next, consider the desired E_J . E_J is important for several reasons:

1. The qubit frequency is given by:

$$\omega_{01} = \sqrt{8E_J E_C} \quad (\text{E.1})$$

The frequency should be compatible with the pulse generators you have, as well as any amplifiers or other microwave equipment. The other important consideration is the Purcell limit—which requires considering the cavity frequency and the type of Purcell filter you might have (see below bullet points).

The qubits in this thesis typically have frequency between 3.5-5GHz.

2. The ratio $\frac{E_J}{E_C}$ should be large enough to safely be in the transmon regime. The exact value of $\frac{E_J}{E_C}$ needed depends on the T_2 you expect [11], but keeping it around 70 is safe.
- The resonator frequency should be far enough detuned from the qubit to give a good Purcell limit (see below) while also being in the band of all of the circulators, amplifiers, and other microwave equipment on the input and output lines. This thesis typically uses a cavity around 7GHz.
 - The coupling between the qubit and the resonator, g , should be large enough to drive the qubit with reasonable drive powers. The trade-off is that too large of a g will lead to Purcell decay, so the value of g should be determined consecutively with the Purcell filter parameters (see below).
 - The dispersive shift, χ should be chosen to give a good readout fidelity while not being too large to lower the Purcell limit. In the case of a transmon without a Purcell filter, the optimal SNR is achieved when $\chi = \kappa/2$ [12].
 - Several different Purcell filter geometries are available. The simplest filter used in this thesis was demonstrated by [47]. It works by adding an additional strongly-coupled resonator in between the readout electronics and the transmon cavity with a bandpass around the resonator frequency and little transmission near the qubit frequency (see section 2.5.1 and figure E.2).

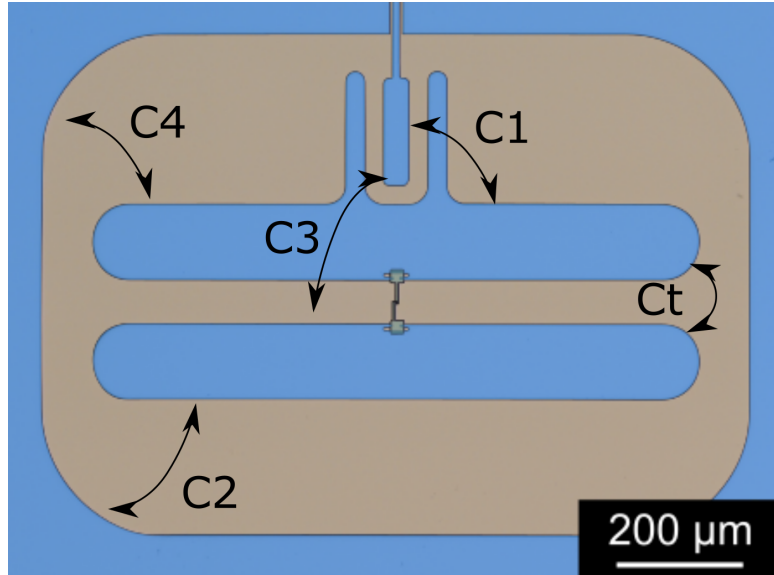


Figure E.1: Definitions of Capacitances.

E.1.2 Transmon Layout

Capacitor Pad Design

The layout of the device should then be updated to reflect the desired Hamiltonian parameters determined in the last section. Tuning the geometry of the capacitor pads, ground plane, and coupler at the end of the resonator requires a fair bit of trial and error. One way to go about this is:

Starting with an arbitrary design:

1. Import the design into a simulation software (Ansys Maxwell, for example) and extract the capacitances shown in figure E.1.
2. Using the equations below, calculate E_C , g , and χ .
3. Feedback from the calculated values to update the design and repeat the process.

First, here are some definitions that will be helpful:

$$C_\phi = \frac{(c_2 + c_3)(c_1 + c_4)}{c_1 + c_2 + c_3 + c_4 + c_t} \quad (\text{E.2})$$

$$C_{c,\text{eff}} = \frac{c_1^2 - c_3 c_4}{c_1 + c_2 + c_3 + c_4 + c_t} \quad (\text{E.3})$$

$$\beta = \frac{c_1 c_2 - c_3 c_4}{(c_2 + c_3)(c_1 + c_4) + (c_1 + c_2 + c_3 + c_4)c_t} \quad (\text{E.4})$$

$$\delta = \omega_r - \omega_{01} \quad (\text{E.5})$$

$$C_{resonator} = \frac{\pi}{2\omega_r Z_0} \quad (\text{E.6})$$

where Z_0 is the characteristic impedance of the resonator.

$$V_{rms} = \sqrt{\frac{\hbar\omega_r}{2C_{resonator}}} \quad (\text{E.7})$$

$$\omega_{01} = \sqrt{8E_J E_C} \quad (\text{E.8})$$

The primary parameters which we are trying to optimize are:

$$E_C = \frac{e^2}{2C_\phi} \frac{1}{\hbar} \quad (\text{E.9})$$

$$g = \frac{eV_{rms}\beta}{\hbar} \sqrt{2} \left(\frac{E_J}{8E_C}\right)^{\frac{1}{4}} \quad (\text{E.10})$$

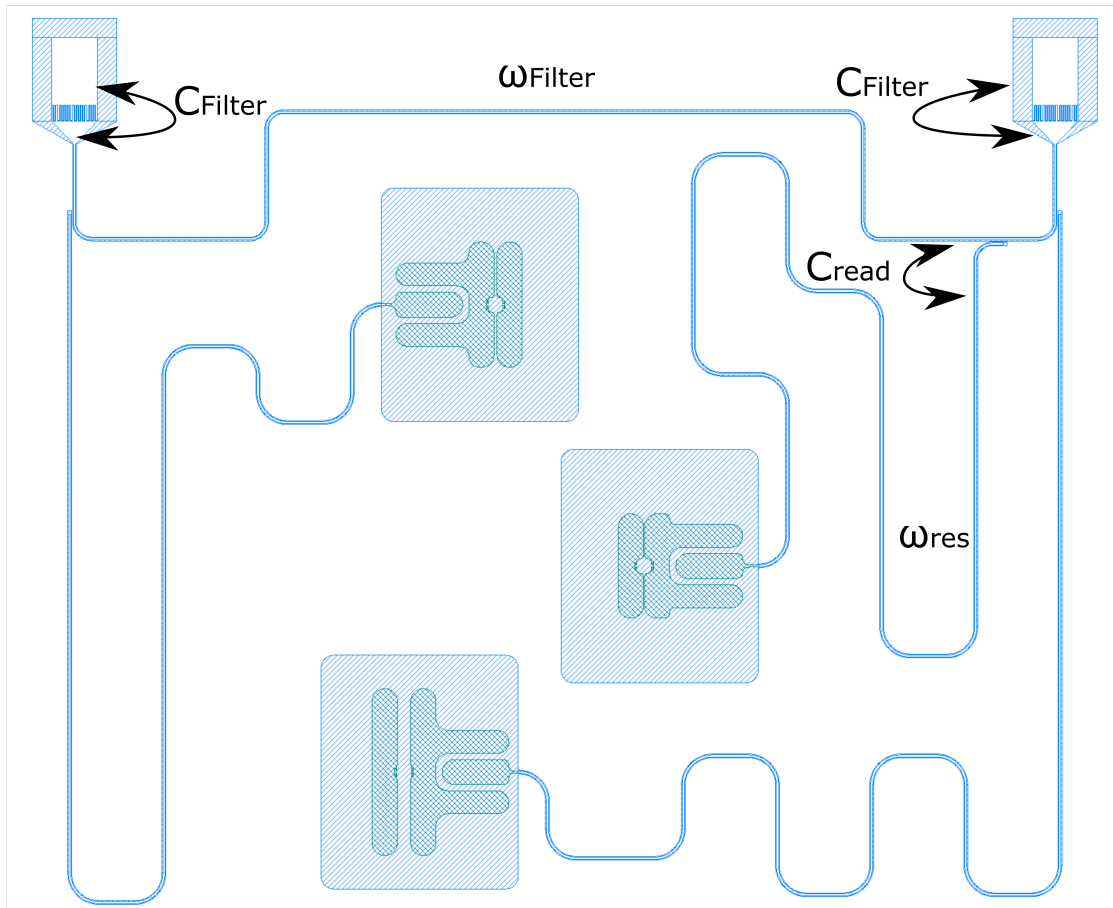
$$\chi = g^2 \frac{E_C}{\delta(\delta - E_C)} \quad (\text{E.11})$$

Purcell Filter Design

The parameters introduced by the Purcell filter are (see figure E.2):

- ω_{filter} : the resonant frequency of the filter resonator.
- C_{filter} : the capacitance between the bond pads and the filter resonator. In the case of figure E.2 the capacitance is given by interdigitated capacitors.
- C_{read} : the capacitance between the filter resonator and the readout resonator.

(a)



(b)

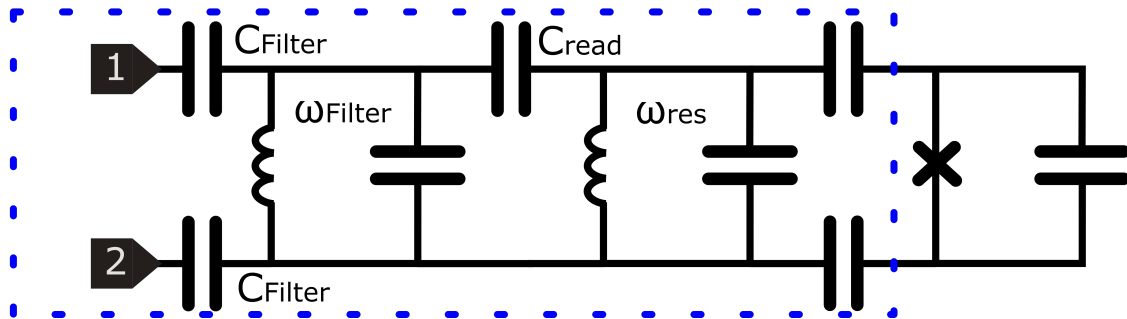
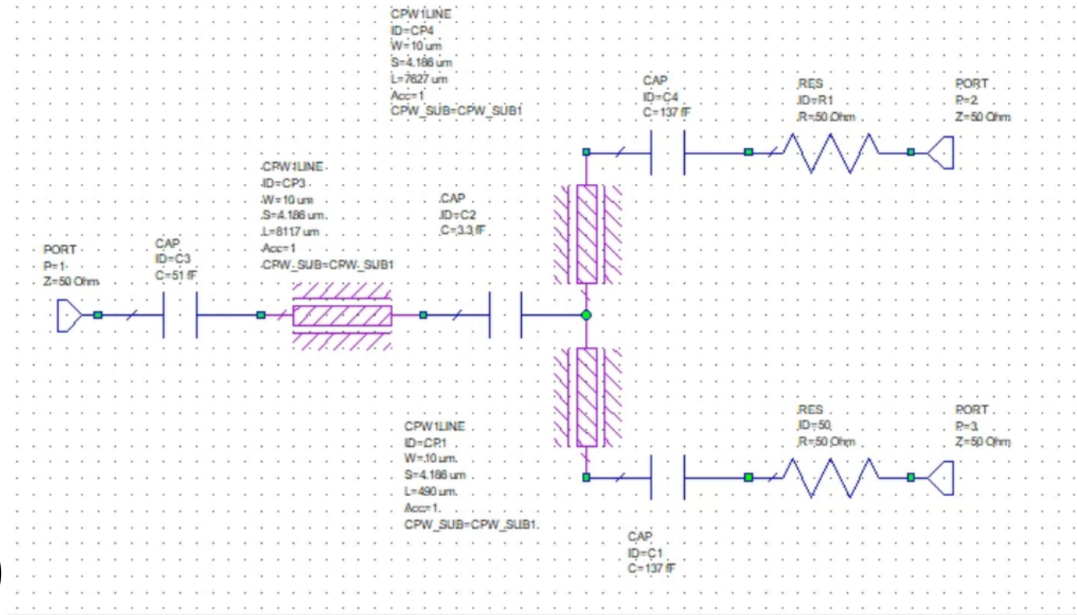


Figure E.2: **Purcell Filter Overview.** (a) Sample device layout labeled with capacitances (represented by arrows) and frequencies. (b) Approximate circuit for layout (only considering one resonator/qubit).

(a)



(b)

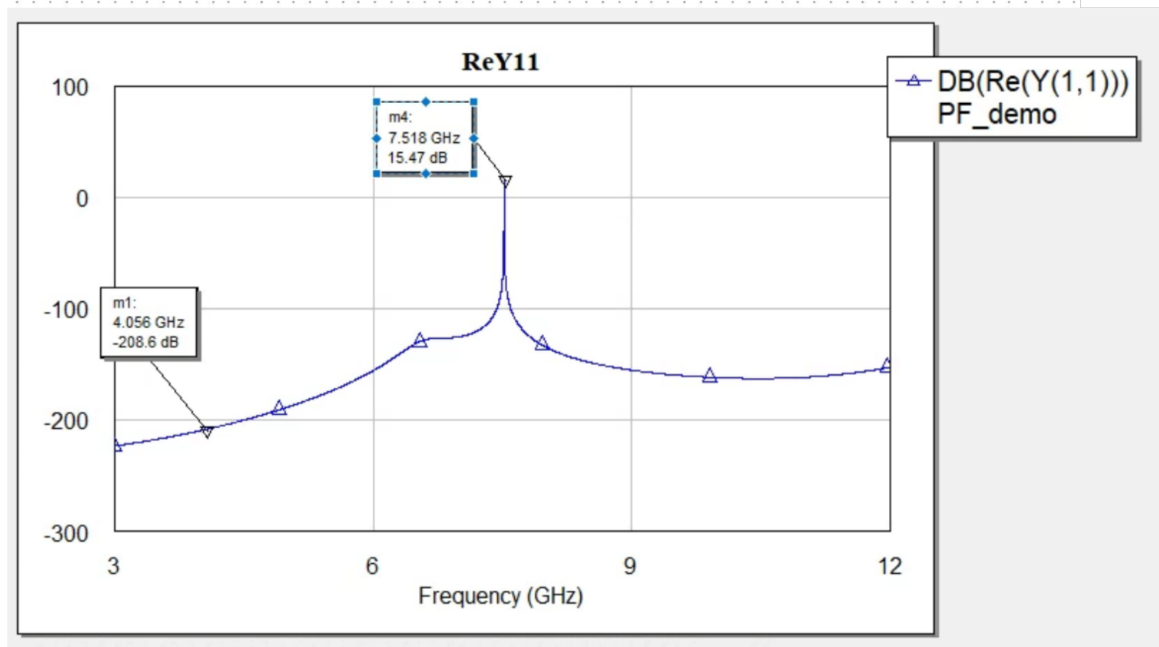


Figure E.3: **Microwave Office Simulation Overview.** (a) Device layout and (b) extracted admittance from AWR Microwave Office simulations of the Purcell filter.

One way to determine the Purcell limit is to simulate the design in AWR Microwave office (figure E.3). The admittance of the filter and readout electronics can be determined from this simulation, which using equation 2.57 leads to the Purcell limit.

Junction Design

Tuning E_J : The E_J of a junction is related to the junction resistance, R_n , through the Ambegaokar-Baratoff relationship [9]:

$$E_J = \frac{1}{2} \frac{h}{(2e)^2} \frac{\Delta}{R_n}. \quad (\text{E.12})$$

This relationship is well approximated by:

$$E_J = \frac{120}{R_n} 10^{12} \frac{Hz}{\Omega} \quad (\text{E.13})$$

Therefore tuning E_J reduces to modifying the resistance of the junction. In order to tune the resistance, we can simply change the width of the streets (see figure D.1 for nomenclature).

Contact Resistance: In order to minimize contact resistance between the junction and the capacitor pads, it may be helpful to have a large contact area (though more tests are needed to confirm whether or not this is important). Further, it is important to consider the aluminum deposition direction with respect to the edge of the tantalum to prevent breaks in the circuit (figure E.4).

Resonator layout

The length of the resonators can be determined from the desired frequency and equation 5.1. Note that at least one wirebond on the resonator should prevent spurious slotline modes of the CPW from forming. However, wirebonding can produce a fair bit of debris so be careful to keep the bond away from the qubit.

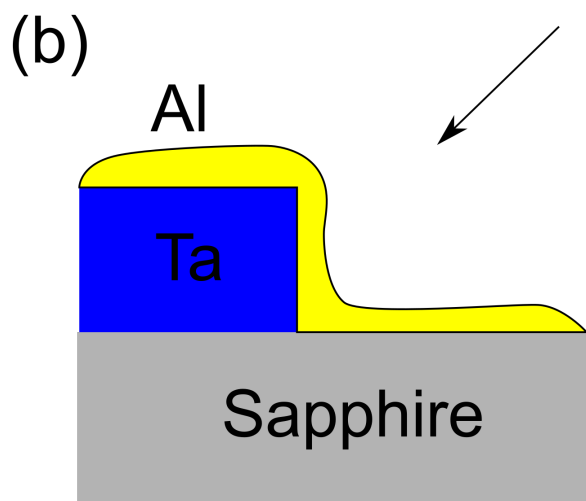
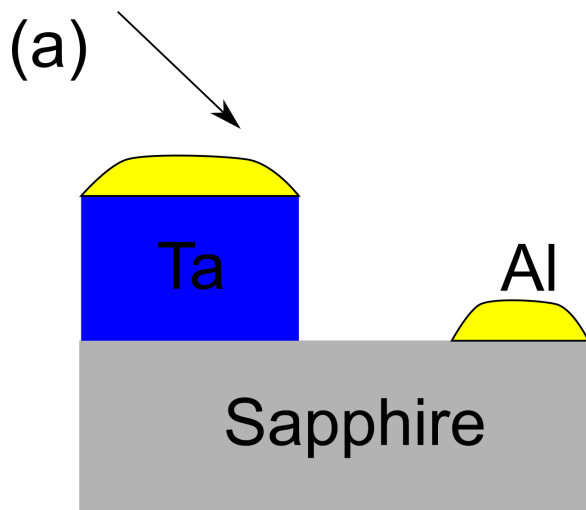


Figure E.4: Importance of Deposition Direction on Capacitor-Junction Contact. The black arrows denote the deposition direction of aluminum relative to the patterned tantalum on sapphire. If the direction is picked incorrectly (a) the tantalum may mask the aluminum, preventing contact between the two metals. However if the direction is picked to climb the edge of the tantalum (b) then a proper contact can be made.

R_n	11 $k\Omega$
E_J	11 GHz
E_C	204 MHz
$\frac{E_J}{E_C}$	54
ω_{01}	4.2 GHz
ω_r	7.3 GHz
β	0.13
g	130 MHz
χ	0.4 MHz
C_{filter}	137 fF
C_{read}	3.3 fF
C_1	51 fF
C_2	47 fF
C_3	2 fF
C_4	86 fF
C_t	58 fF
$Y_{environment@\omega_{01}}$	-206 dB
$T_{1,Purcell}$	1.2ms

Table E.1: **Example Transmon Parameters.**

E.1.3 Example Transmon Parameters

Example parameters are given in table E.1.

Appendix F

Participation Ratio Simulations

To determine the participation ratio of a qubit we primarily follow the procedure outlined in [23]. We will give a brief summary below.

F.1 Participation Ratio Simulations: Qubits

In an ideal world we could calculate the participation ratio of a design by simulating the field distribution in a three-dimensional model of a qubit which includes the several-nanometer thick interfaces. However, simulating the electric field in a roughly 1 mm^3 volume at the nanometer scale in order to find the electric field in the interfaces is computationally intensive. To reduce the simulation time, we break the simulation down into several parts:

1. **Main Capacitor Simulation** The superconductor is simulated as infinitely thin two-dimensional sheets on a three-dimensional substrate (figure F.1 (a)). The electric field around the metal far from the sheet edges (i.e. in the bulk of the capacitor) can be used to extrapolate the participation ratio at the corresponding interfaces. However, this simulation isn't accurate near the edges of the capacitor or near the junction, which will require separate simulations.
2. **Two-Dimensional Edge Simulation** The electric field near the edges of a two-dimensional sheet is very different to that around a 200nm thick superconductor.

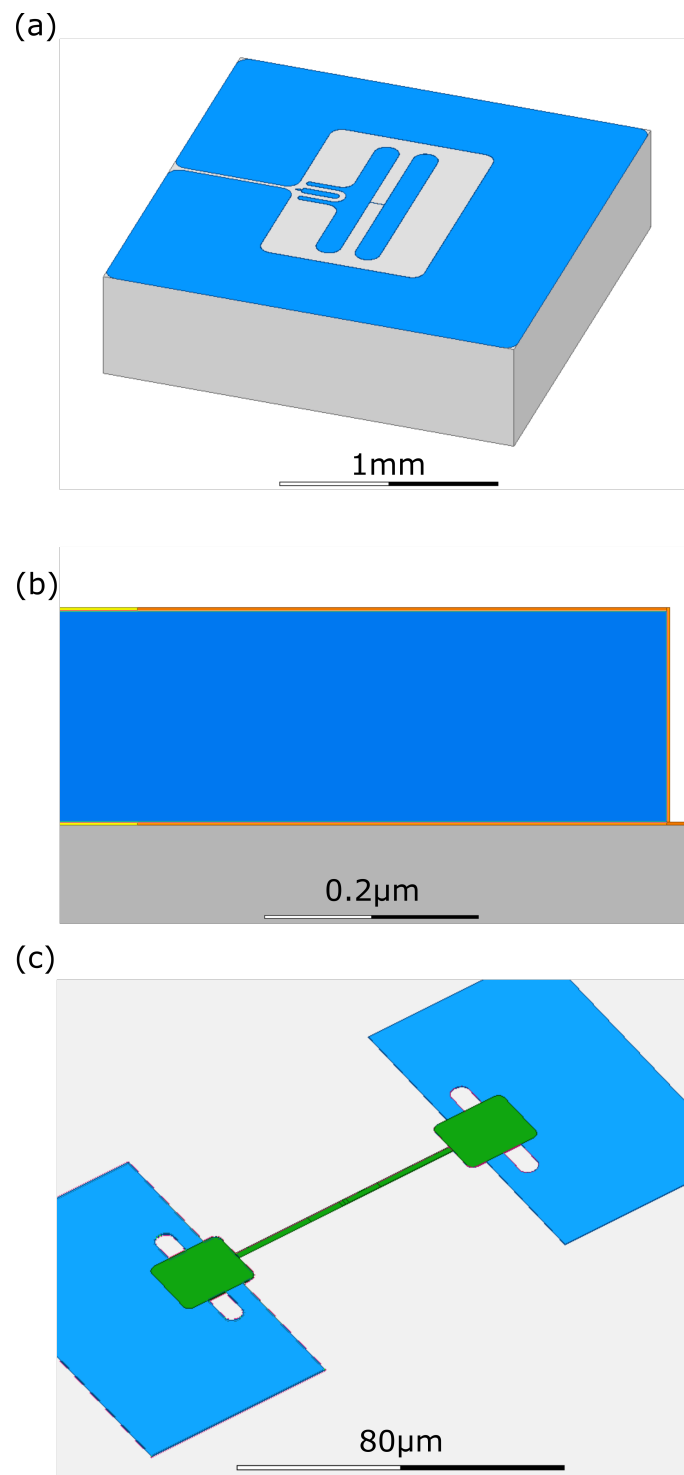


Figure F.1: Overview of Simulation Components. Sapphire is shown in grey, tantalum in blue, and aluminum in green in all panels. (a) Main capacitor simulation, composed of two-dimensional perfect conductivity capacitor pads shorted by an inductive element. (b) Zoomed-in edge simulation. Interfaces too close to the edge to be well simulated in (a) are shown in orange. The bulk interface used to scale the electric field to that of (a) is shown in yellow. (c) Full three-dimensional simulation of the junction region, with several nanometer thick interfaces included. Figures are made using Ansys Simulation Software.

Pitch (μm)	Substrate-Air	Metal-Air	Metal-Substrate
5	7.9	0.53	4.5
15	4.5	0.25	2.5
65	2.2	0.11	1.3
70	2.4	0.12	1.4

Table F.1: **Capacitor Pad Participation Ratios.** Interface participation ratios of the designs shown in figure F.2, excluding the aluminum highways and junctions (note that the ground planes and couplers, included in the simulation, are not shown). All participation ratio values are in units of 10^{-4} .

To account for this difference, we perform a high-resolution simulation of the edge region of a 200nm thick superconductor (figure F.1 (b)). This gives the relative strength of the field within $1\mu\text{m}$ of the edge to the field near the bulk capacitor. At each point of the edge in simulation (1), scaling the electric field in the bulk of this zoomed-in simulation to the nearby-bulk of the planar simulation, we can find the electric field near the edges of simulation (1).

3. **Junction Simulation** The junction region is small enough that a nanometer-resolution simulation of only the region close to the junction is practical (figure F.1 (c)).

Note that the region within $1\mu\text{m}$ of the junction is ignored. This is partly because of the difficulty of simulating this complicated geometry. However, it is also unclear whether or not this region contributes significantly to losses (see section 2.3.8).

F.1.1 Results

Tantalum Capacitors

We simulate four different tantalum capacitor designs, all with E_c near 200MHz, shown in figure F.2. The participation ratio results ignoring the junctions are shown in table F.1. The corresponding sapphire substrate participation ratio is 0.91 for all four geometries.

Aluminum Junction

The participation ratios of the aluminum junction are given in table F.2. Note that the metal-substrate interface of aluminum is only about a factor of 8 lower than the

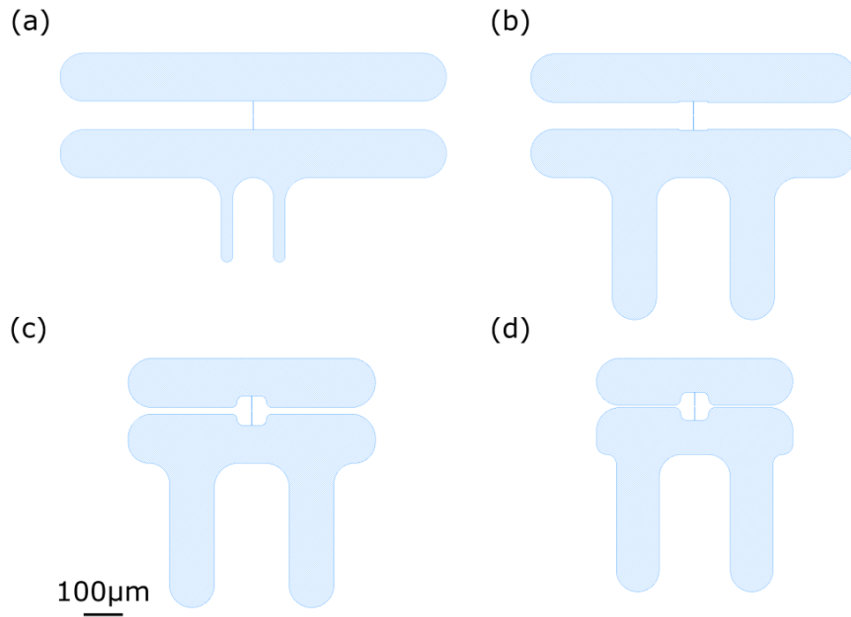


Figure F.2: **Simulated Designs.** Capacitor pad geometries with (a) $70\mu\text{m}$, (b) $65\mu\text{m}$, (c) $15\mu\text{m}$, and (d) $5\mu\text{m}$ pitch. Note the junction region is consistent across all panels. The scalebar applies for all designs shown.

Metal-Air	Metal-Substrate
0.018	0.16

Table F.2: **Aluminum Participation Ratio.** Interface participation ratios of junctions for all designs shown in figure F.2, ignoring the region within $1\mu\text{m}$ of the junction. All participation ratio values are in units of 10^{-4} . Note that for ease of simulation any region with aluminum stacked on top of tantalum was approximated to be only aluminum.

Pitch (μm)	Substrate-Air	Metal-Air	Metal-Substrate
2	28.3	3.0	23.5
4	15.4	1.5	13.0
6	10.8	1.0	9.1
8	8.3	0.76	7.1
10	6.8	0.61	5.9
12	5.8	0.51	5.0
14	5.1	0.44	4.4
16	4.5	0.38	3.9

Table F.3: **Coplanar Waveguide Participation Ratios.** All participation ratio values are in units of 10^{-4} .

metal-substrate interface of the $65 \mu\text{m}$ pitch capacitor pads, suggesting that it is not inconceivable that the aluminum is a significant source of TLS.

F.2 Participation Ratio Simulations: Resonators

Simulating resonators is far simpler than qubits. The reason is that resonators, if we ignore the impedance mismatch at the ends and any curves, are a two-dimensional cross section swept along the length of the centerpin. Accordingly a two-dimensional simulation of this cross section which includes a several-nanometer thick oxide layer at the interfaces is sufficient (see figure 5.1 for example, which has an exaggerated metal-air interface). The results of these simulations are given in table F.3.

Appendix G

Sample Resonator Temperature and Power Dependent Fits

This thesis relies heavily on parameters extracted from temperature and power dependent resonator fits. Figures G.1, G.2, and G.3 give an idea for the minimum goodness of fit used to make figure 5.5. Some devices with worse fits were excluded from the data set.

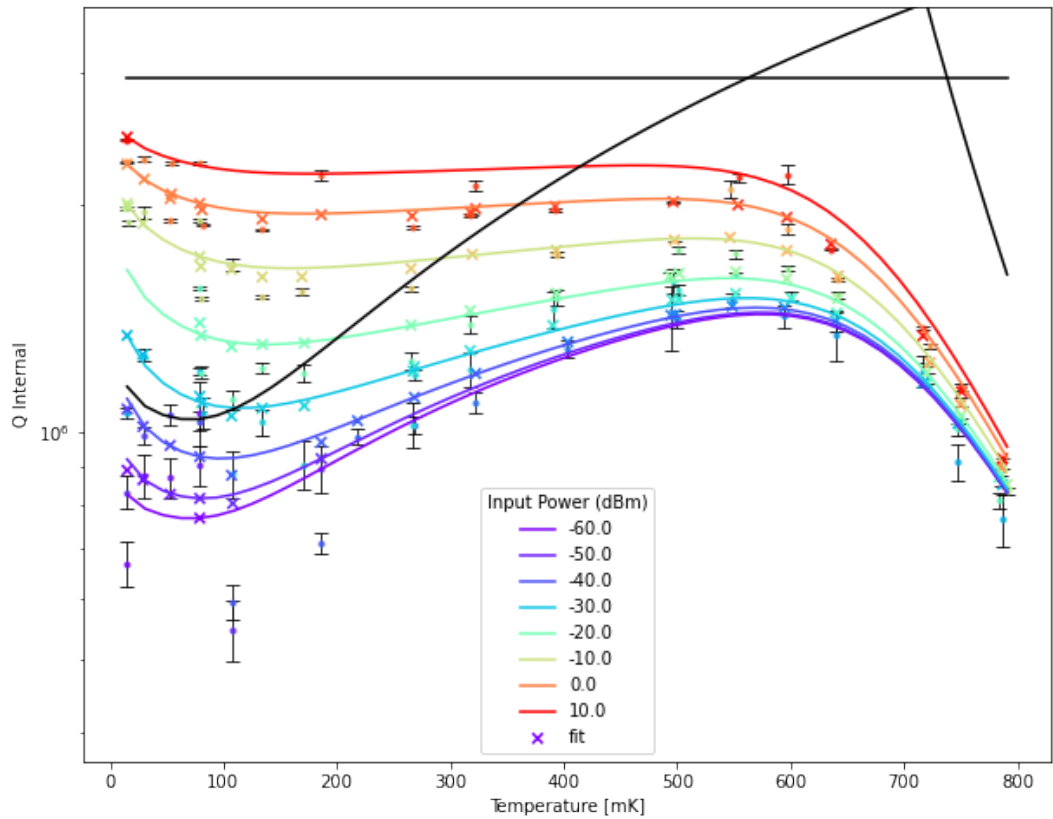


Figure G.1: Sample Low Quality Fit. Temperature and power dependent measurement of the internal quality factor for a CPW resonator that was dipped in BOE and employed the chlorine plasma etch. This device had uncharacteristically noisy low power data. The format of the plot is explained in figure 5.3.

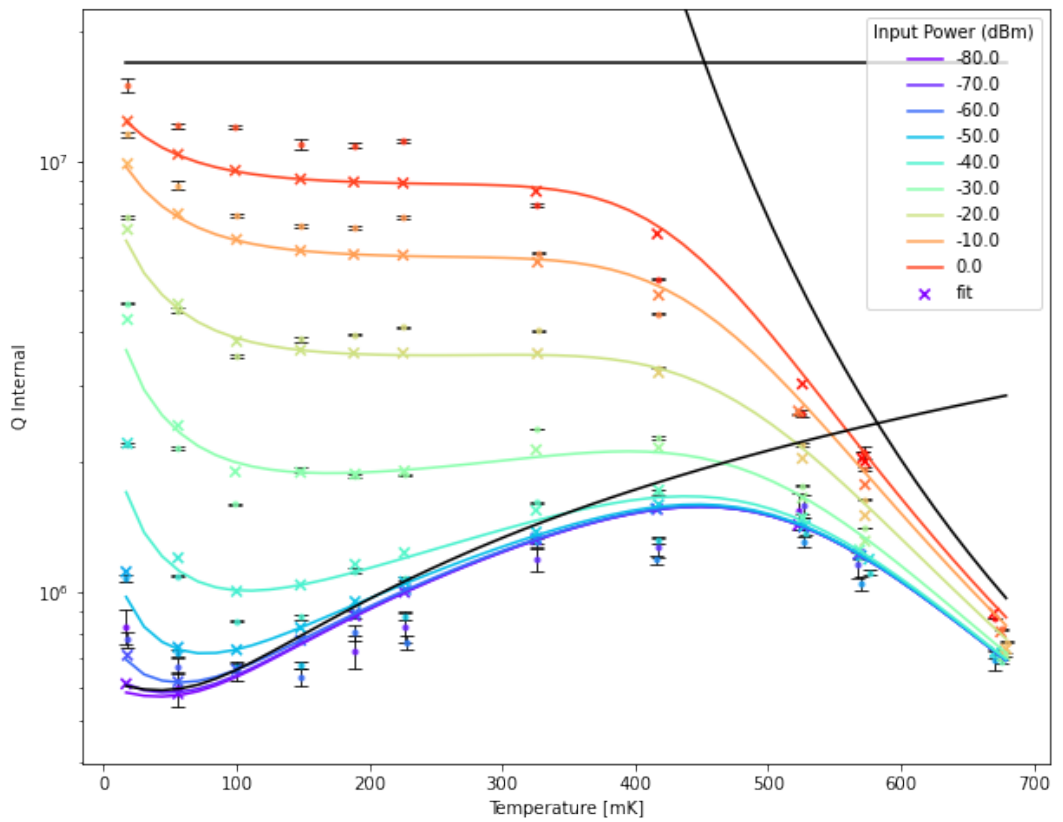


Figure G.2: **Sample Low Quality Fit.** Temperature and power dependent measurement of the internal quality factor for a CPW resonator that was dipped in BOE and employed the chlorine plasma etch. The fit for this device has particularly bad agreement with the high-power, low temperature data. The format of the plot is explained in figure 5.3.

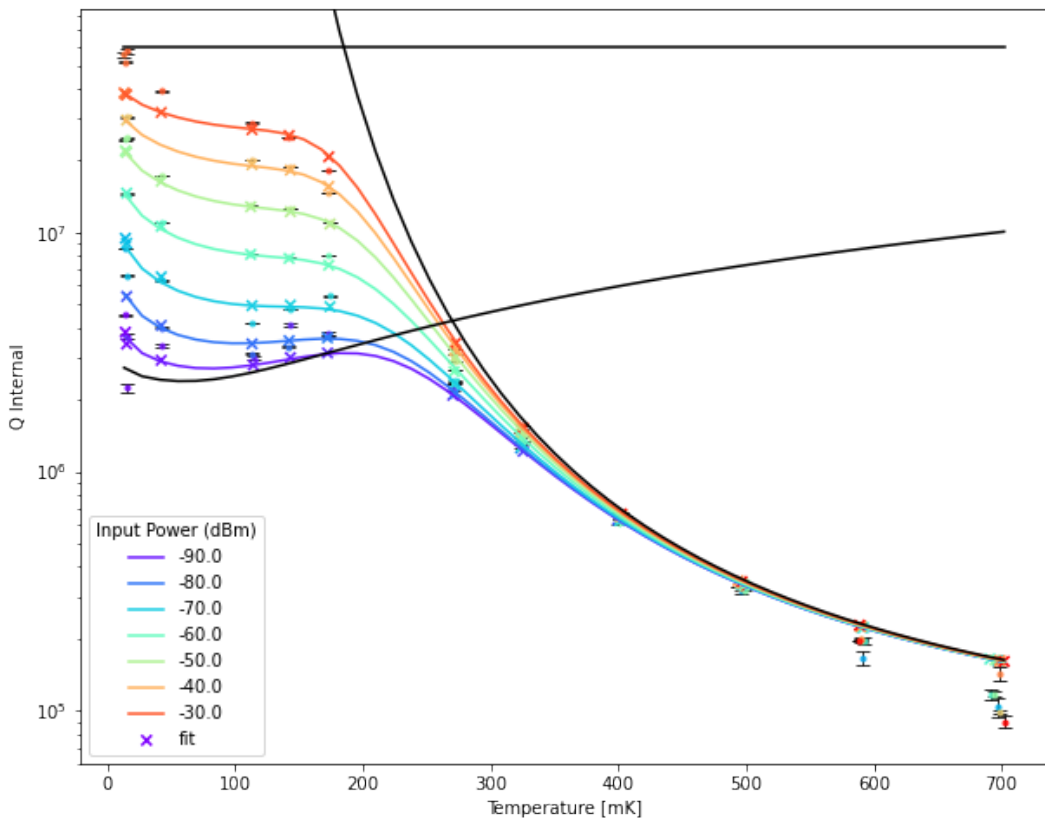


Figure G.3: **Sample Low T_c Fit.** Temperature and power dependent measurement of the internal quality factor for a lumped element resonator that was dipped in BOE and employed the chlorine plasma etch. The device T_c is low, which gives less data points to constrain the non-quasiparticle related fit parameters. The format of the plot is explained in figure 5.3.

Bibliography

1. Minev, Z. K. *et al.* To catch and reverse a quantum jump mid-flight. *Nature* **570**, 200–204 (2019).
2. Rice, J. E. *et al.* Quantum computation of dominant products in lithium–sulfur batteries. *The Journal of Chemical Physics* **154**, 134115 (2021).
3. Batra, K. *et al.* Quantum machine learning algorithms for drug discovery applications. *Journal of Chemical Information and Modeling* **61**, 2641–2647 (2021).
4. Riste, D. *et al.* Demonstration of quantum advantage in machine learning. *npj Quantum Information* **3**, 1–5 (2017).
5. Gisin, N., Ribordy, G., Tittel, W. & Zbinden, H. Quantum cryptography. *Reviews of modern physics* **74**, 145 (2002).
6. Zhang, J. *et al.* Observation of a many-body dynamical phase transition with a 53-qubit quantum simulator. *Nature* **551**, 601–604 (2017).
7. Awschalom, D. D., Hanson, R., Wrachtrup, J. & Zhou, B. B. Quantum technologies with optically interfaced solid-state spins. *Nature Photonics* **12**, 516–527 (2018).
8. Bernien, H. *et al.* Probing many-body dynamics on a 51-atom quantum simulator. *Nature* **551**, 579–584 (2017).
9. Girvin, S. M. Circuit QED: superconducting qubits coupled to microwave photons. *Quantum machines: measurement and control of engineered quantum systems*, 113–256 (2014).
10. Shankar, R. *Principles of quantum mechanics* (Springer Science & Business Media, 2012).

11. Koch, J. *et al.* Charge-insensitive qubit design derived from the Cooper pair box. *Physical Review A* **76**, 042319 (2007).
12. Schuster, D. I. *Circuit quantum electrodynamics* (Yale University, 2007).
13. Nielsen, M. A. & Chuang, I. L. *Quantum Computation and Quantum Information* (Cambridge University Press, 2017).
14. Arute, F. *et al.* Quantum supremacy using a programmable superconducting processor. *Nature* **574**, 505–510 (2019).
15. Terhal, B. M. Quantum error correction for quantum memories. *Reviews of Modern Physics* **87**, 307 (2015).
16. Marques, J. *et al.* Logical-qubit operations in an error-detecting surface code. *Nature Physics* **18**, 80–86 (2022).
17. Kjaergaard, M. *et al.* Superconducting Qubits: Current State of Play. *arXiv preprint arXiv:1905.13641* (2019).
18. Nakamura, Y., Pashkin, Y. A. & Tsai, J. Coherent control of macroscopic quantum states in a single-Cooper-pair box. *nature* **398**, 786–788 (1999).
19. Nersisyan, A. *et al.* Manufacturing low dissipation superconducting quantum processors. *arXiv preprint arXiv:1901.08042* (2019).
20. Paik, H. *et al.* Observation of high coherence in Josephson junction qubits measured in a three-dimensional circuit QED architecture. *Physical Review Letters* **107**, 240501 (2011).
21. Joshi, A., Noh, K. & Gao, Y. Y. Quantum information processing with bosonic qubits in circuit QED. *Quantum Science and Technology* **6**, 033001 (2021).
22. Martinis, J. M. & Megrant, A. UCSB final report for the CSQ program: Review of decoherence and materials physics for superconducting qubits. *arXiv preprint arXiv:1410.5793* (2014).
23. Wang, C. *et al.* Surface participation and dielectric loss in superconducting qubits. *Applied Physics Letters* **107**, 162601 (2015).

24. Müller, C., Cole, J. H. & Lisenfeld, J. Towards understanding two-level-systems in amorphous solids: insights from quantum circuits. *Reports on Progress in Physics* **82**, 124501 (2019).
25. Phillips, W. A. Two-level states in glasses. *Reports on Progress in Physics* **50**, 1657 (1987).
26. Gao, J. *The physics of superconducting microwave resonators* (California Institute of Technology, 2008).
27. Mamin, H. *et al.* Merged-element transmons: Design and qubit performance. *Physical Review Applied* **16**, 024023 (2021).
28. Martinis, J. M. *et al.* Decoherence in Josephson qubits from dielectric loss. *Physical review letters* **95**, 210503 (2005).
29. Spiecker, M. *et al.* A quantum Szilard engine for two-level systems coupled to a qubit. *arXiv preprint arXiv:2204.00499* (2022).
30. Bertrand, P. *Electron Paramagnetic Resonance Spectroscopy* (Springer, 2020).
31. Schlör, S. *et al.* Correlating decoherence in transmon qubits: Low frequency noise by single fluctuators. *Physical review letters* **123**, 190502 (2019).
32. Burnett, J. *et al.* Evidence for interacting two-level systems from the 1/f noise of a superconducting resonator. *Nature Communications* **5**, 1–6 (2014).
33. Wang, H. *et al.* Improving the coherence time of superconducting coplanar resonators. *Applied Physics Letters* **95**, 233508 (2009).
34. Woods, W. *et al.* Determining interface dielectric losses in superconducting coplanar-waveguide resonators. *Physical Review Applied* **12**, 014012 (2019).
35. Catelani, G., Schoelkopf, R. J., Devoret, M. H. & Glazman, L. I. Relaxation and frequency shifts induced by quasiparticles in superconducting qubits. *Physical Review B* **84**, 064517 (2011).
36. Serniak, K. *et al.* Hot nonequilibrium quasiparticles in transmon qubits. *Physical Review Letters* **121**, 157701 (2018).

37. Ristè, D. *et al.* Millisecond charge-parity fluctuations and induced decoherence in a superconducting transmon qubit. *Nature communications* **4**, 1–6 (2013).
38. Zmuidzinas, J. Superconducting microresonators: Physics and applications. *Annu. Rev. Condens. Matter Phys.* **3**, 169–214 (2012).
39. Vepsäläinen, A. P. *et al.* Impact of ionizing radiation on superconducting qubit coherence. *Nature* **584**, 551–556 (2020).
40. Wilen, C. D. *et al.* Correlated charge noise and relaxation errors in superconducting qubits. *Nature* **594**, 369–373 (2021).
41. Houzet, M., Serniak, K., Catelani, G., Devoret, M. & Glazman, L. Photon-assisted charge-parity jumps in a superconducting qubit. *Physical review letters* **123**, 107704 (2019).
42. Rafferty, O. *et al.* Spurious antenna modes of the transmon qubit. *arXiv preprint arXiv:2103.06803* (2021).
43. Pan, X. *et al.* Engineering superconducting qubits to reduce quasiparticles and charge noise. *arXiv preprint arXiv:2202.01435* (2022).
44. Liu, C.-H. *et al.* Quasiparticle Poisoning of Superconducting Qubits from Resonant Absorption of Pair-breaking Photons. *arXiv preprint arXiv:2203.06577* (2022).
45. Diamond, S. *et al.* Distinguishing parity-switching mechanisms in a superconducting qubit. *arXiv preprint arXiv:2204.07458* (2022).
46. Bronn, N. T. *et al.* Broadband filters for abatement of spontaneous emission in circuit quantum electrodynamics. *Applied Physics Letters* **107**, 172601 (2015).
47. Jeffrey, E. *et al.* Fast accurate state measurement with superconducting qubits. *Physical review letters* **112**, 190504 (2014).
48. Maki, K. Fluxoid structure in superconducting films. *Annals of Physics* **34**, 363–376 (1965).
49. Song, C. *et al.* Microwave response of vortices in superconducting thin films of Re and Al. *Physical Review B* **79**, 174512 (2009).

50. Wang, C. *et al.* Measurement and control of quasiparticle dynamics in a superconducting qubit. *Nature Communications* **5**, 5836 (2014).
51. De Graaf, S. *et al.* Two-level systems in superconducting quantum devices due to trapped quasiparticles. *arXiv preprint arXiv:2004.02485* (2020).
52. Premkumar, A. *et al.* Microscopic Relaxation Channels in Materials for Superconducting Qubits. *arXiv preprint arXiv:2004.02908* (2020).
53. Gambetta, J. M. *et al.* Investigating surface loss effects in superconducting transmon qubits. *IEEE Transactions on Applied Superconductivity* **27**, 1–5 (2016).
54. Quintana, C. *et al.* Characterization and reduction of microfabrication-induced decoherence in superconducting quantum circuits. *Applied Physics Letters* **105**, 062601 (2014).
55. Gladczuk, L., Patel, A., Paur, C. S. & Sosnowski, M. Tantalum films for protective coatings of steel. *Thin Solid Films* **467**, 150–157 (2004).
56. Stevie, F. A. & Donley, C. L. Introduction to x-ray photoelectron spectroscopy. *Journal of Vacuum Science & Technology A: Vacuum, Surfaces, and Films* **38**, 063204 (2020).
57. Place, A. P. *et al.* New material platform for superconducting transmon qubits with coherence times exceeding 0.3 milliseconds. *Nature communications* **12**, 1–6 (2021).
58. Montanaro, A. Quantum algorithms: an overview. *npj Quantum Information* **2**, 15023 (2016).
59. Kandala, A. *et al.* Hardware-efficient variational quantum eigensolver for small molecules and quantum magnets. *Nature* **549**, 242 (2017).
60. O’Malley, P. J. *et al.* Scalable quantum simulation of molecular energies. *Physical Review X* **6**, 031007 (2016).
61. Ofek, N. *et al.* Extending the lifetime of a quantum bit with error correction in superconducting circuits. *Nature* **536**, 441 (2016).

62. Hu, L. *et al.* Quantum error correction and universal gate set operation on a binomial bosonic logical qubit. *Nature Physics* **15**, 503 (2019).
63. Reed, M. D. *et al.* Realization of three-qubit quantum error correction with superconducting circuits. *Nature* **482**, 382 (2012).
64. Arute, F. *et al.* Quantum supremacy using a programmable superconducting processor. *Nature* **574**, 505–510 (2019).
65. Oliver, W. D. & Welander, P. B. Materials in superconducting quantum bits. *MRS Bulletin* **38**, 816–825 (2013).
66. Córcoles, A. D. *et al.* Protecting superconducting qubits from radiation. *Applied Physics Letters* **99**, 181906 (2011).
67. Gustavsson, S. *et al.* Suppressing relaxation in superconducting qubits by quasi-particle pumping. *Science* **354**, 1573–1577 (2016).
68. Chen, Y. *et al.* Qubit architecture with high coherence and fast tunable coupling. *Physical Review Letters* **113**, 220502 (2014).
69. Mundada, P., Zhang, G., Hazard, T. & Houck, A. Suppression of qubit crosstalk in a tunable coupling superconducting circuit. *Physical Review Applied* **12**, 054023 (2019).
70. Devoret, M. H. & Schoelkopf, R. J. Superconducting circuits for quantum information: an outlook. *Science* **339**, 1169–1174 (2013).
71. Barends, R. *et al.* Superconducting quantum circuits at the surface code threshold for fault tolerance. *Nature* **508**, 500–503 (2014).
72. Wei, K. X. *et al.* Verifying Multipartite Entangled GHZ States via Multiple Quantum Coherences. *arXiv preprint arXiv:1905.05720* (2019).
73. Dunsworth, A. *et al.* Characterization and reduction of capacitive loss induced by sub-micron Josephson junction fabrication in superconducting qubits. *Applied Physics Letters* **111**, 022601 (2017).

74. Kamal, A. *et al.* Improved superconducting qubit coherence with high-temperature substrate annealing. *arXiv preprint arXiv:1606.09262* (2016).
75. Lisenfeld, J. *et al.* Electric field spectroscopy of material defects in transmon qubits. *npj Quantum Information* **5**, 1–6 (2019).
76. Braginsky, V., Ilchenko, V. & Bagdassarov, K. S. Experimental observation of fundamental microwave absorption in high-quality dielectric crystals. *Physics Letters A* **120**, 300–305 (1987).
77. Luiten, A., Mann, A. & Blair, D. Ultrahigh Q-factor cryogenic sapphire resonator. *Electronics Letters* **29**, 879–881 (1993).
78. Cava, R. J. *et al.* Electrical and magnetic properties of Nb₂O₅-δ crystallographic shear structures. *Physical Review B* **44**, 6973 (1991).
79. Nico, C., Monteiro, T. & Graça, M. P. Niobium oxides and niobates physical properties: Review and prospects. *Progress in Materials Science* **80**, 1–37 (2016).
80. Face, D. & Prober, D. Nucleation of body-centered-cubic tantalum films with a thin niobium underlayer. *Journal of Vacuum Science & Technology A: Vacuum, Surfaces, and Films* **5**, 3408–3411 (1987).
81. Face, D., Prober, D., McGrath, W. & Richards, P. High quality tantalum superconducting tunnel junctions for microwave mixing in the quantum limit. *Applied Physics Letters* **48**, 1098–1100 (1986).
82. Dwikusuma, F., Saulys, D. & Kuech, T. Study on sapphire surface preparation for III-nitride heteroepitaxial growth by chemical treatments. *Journal of The Electrochemical Society* **149**, G603–G608 (2002).
83. Potts, A., Parker, G., Baumberg, J. & de Groot, P. CMOS compatible fabrication methods for submicron Josephson junction qubits. *IEE Proceedings-Science, Measurement and Technology* **148**, 225–228 (2001).
84. Barends, R. *et al.* Coherent Josephson qubit suitable for scalable quantum integrated circuits. *Physical Review Letters* **111**, 080502 (2013).

85. Wallraff, A. *et al.* Approaching unit visibility for control of a superconducting qubit with dispersive readout. *Physical Review Letters* **95**, 060501 (2005).
86. Face, D. & Prober, D. Nucleation of body-centered-cubic tantalum films with a thin niobium underlayer. *Journal of Vacuum Science & Technology A: Vacuum, Surfaces, and Films* **5**, 3408–3411 (1987).
87. Read, M. H. & Altman, C. A new structure in tantalum thin films. *Applied Physics Letters* **7**, 51–52 (1965).
88. Bylander, J. *et al.* Noise spectroscopy through dynamical decoupling with a superconducting flux qubit. *Nature Physics* **7**, 565–570 (2011).
89. Huang, Z. *et al.* Engineering Dynamical Sweet Spots to Protect Qubits from $1/f$ Noise. *arXiv preprint arXiv:2004.12458* (2020).
90. Reed, M. D. *et al.* Fast reset and suppressing spontaneous emission of a superconducting qubit. *Applied Physics Letters* **96**, 203110 (2010).
91. McGuire, G., Schweitzer, G. K. & Carlson, T. A. Core electron binding energies in some Group IIIA, VB, and VIB compounds. *Inorganic Chemistry* **12**, 2450–2453 (1973).
92. Himpsel, F., Morar, J., McFeely, F., Pollak, R. & Hollinger, G. Core-level shifts and oxidation states of Ta and W: Electron spectroscopy for chemical analysis applied to surfaces. *Physical Review B* **30**, 7236 (1984).
93. Kronberg, M. Plastic deformation of single crystals of sapphire: basal slip and twinning. *Acta Metallurgica* **5**, 507–524 (1957).
94. Moulder, J. F. Handbook of X-ray photoelectron spectroscopy. *Physical Electronics*, 170–171 (1995).
95. Shinotsuka, H., Tanuma, S., Powell, C. & Penn, D. Calculations of electron inelastic mean free paths. X. Data for 41 elemental solids over the 50 eV to 200 keV range with the relativistic full Penn algorithm. *Surface and Interface Analysis* **47**, 871–888 (2015).

96. Cumpson, P. J. Angle-resolved XPS and AES: depth-resolution limits and a general comparison of properties of depth-profile reconstruction methods. *Journal of Electron Spectroscopy and Related Phenomena* **73**, 25–52 (1995).
97. Kreikebaum, J. M., Dove, A., Livingston, W., Kim, E. & Siddiqi, I. Optimization of infrared and magnetic shielding of superconducting TiN and Al coplanar microwave resonators. *Superconductor Science and Technology* **29**, 104002 (2016).
98. Wang, Z. *et al.* Cavity attenuators for superconducting qubits. *Physical Review Applied* **11**, 014031 (2019).
99. Klimov, P. *et al.* Fluctuations of energy-relaxation times in superconducting qubits. *Physical Review Letters* **121**, 090502 (2018).
100. Kelly, J. *et al.* State preservation by repetitive error detection in a superconducting quantum circuit. *Nature* **519**, 66–69 (2015).
101. Serniak, K. *et al.* Direct Dispersive Monitoring of Charge Parity in Offset-Charge-Sensitive Transmons. *Physical Review Applied* **12**, 014052 (2019).
102. Dial, O. *et al.* Bulk and surface loss in superconducting transmon qubits. *Superconductor Science and Technology* **29**, 044001 (2016).
103. Touzard, S. *et al.* Gated conditional displacement readout of superconducting qubits. *Physical review letters* **122**, 080502 (2019).
104. Sangtawesin, S. *et al.* Origins of Diamond Surface Noise Probed by Correlating Single-Spin Measurements with Surface Spectroscopy. *Physical Review X* **9**, 031052 (2019).
105. Stick, D. *et al.* Ion trap in a semiconductor chip. *Nature Physics* **2**, 36 (2006).
106. Hite, D. *et al.* Surface science for improved ion traps. *MRS Bulletin* **38**, 826–833 (2013).
107. Schenkel, T. *et al.* Electrical activation and electron spin coherence of ultralow dose antimony implants in silicon. *Applied Physics Letters* **88**, 112101 (2006).

108. Paik, S.-Y., Lee, S.-Y., Baker, W., McCamey, D. & Boehme, C. T 1 and T 2 spin relaxation time limitations of phosphorous donor electrons near crystalline silicon to silicon dioxide interface defects. *Physical Review B* **81**, 075214 (2010).
109. Yoneda, J. *et al.* A quantum-dot spin qubit with coherence limited by charge noise and fidelity higher than 99.9%. *Nature Nanotechnology* **13**, 102 (2018).
110. Pozar, D. M. *Microwave engineering* (John wiley & sons, 2011).
111. Geerlings, K. L. *Improving coherence of superconducting qubits and resonators* (Yale University, 2013).
112. Altoé, M. V. P. *et al.* Localization and Mitigation of Loss in Niobium Superconducting Circuits. *PRX Quantum* **3**, 020312 (2022).
113. Chow, J. M. *Quantum information processing with superconducting qubits* (Yale University, 2010).